

TRANSFORMATION TOUGHENING OF METASTABLE
AUSTENITIC STEELS

by

RICARDO HENRIQUES LEAL

B.S., Instituto Militar de Engenharia, Brazil
(1977)

M.S., Instituto Militar de Engenharia, Brazil
(1979)

Submitted to the Department of
Materials Science and Engineering
in Partial Fulfillment of the Requirements
of the Degree of

DOCTOR OF PHILOSOPHY

at the

MASSACHUSETTS INSTITUTE OF TECHNOLOGY

June 1984

c Massachusetts Institute of Technology 1984

Signature of Author *Ricardo Henrique Leal*
Department of Materials Science and Engineering
May 4, 1984

Certified by *Morris Cohen*
Professor Morris Cohen
Thesis Supervisor

Certified by *Gregory B. Olson*
Dr. Gregory B. Olson
Thesis Supervisor

Accepted by *Bernhardt J. Wuensch*
Professor Bernhardt J. Wuensch
Chairman, Department Committee

MASSACHUSETTS INSTITUTE
OF TECHNOLOGY

TRANSFORMATION TOUGHENING OF METASTABLE
AUSTENITIC STEELS

by

RICARDO HENRIQUES LEAL

Submitted to the Department of Materials Science and Engineering on May 4, 1984 in partial fulfillment of the requirements for the Degree of Doctor of Philosophy in Metallurgy

ABSTRACT

Tensile tests and fracture toughness tests using the J-integral technique were performed on precipitation hardened metastable austenitic steels of five different compositions over the temperature range of -196°C to 300°C . One of these alloys was stable with respect to mechanically-induced martensitic transformation. The other four were metastable with respect to the same transformation and presented different transformational volume expansions.

The results indicate that significant toughness enhancement is promoted by the mechanically-induced martensitic transformation. This effect is manifested in uniform elongation, true strain to failure in the neck, J_{IC} and crack-growth resistance. A similar temperature dependence is observed for all these parameters, and their enhancements can be analysed within the same general framework.

Concerning uniform elongation, a 3- to 4- fold increase is obtained as compared to stable austenite. The transformation increases the uniform elongation by altering the flow behavior via a combination of dynamic softening and static-hardening. In altering the shape of the true-stress, true-strain curve, the onset of necking is delayed to very large plastic strains. Both the experimental results and a proposed model indicate that an optimum transformation stability exists for which the enhancement is maximum. A drop in uniform elongation is found at temperatures where only a very small amount of transformation takes place before necking. This drop is accounted for by analysing the alterations in the stress-strain behavior.

Fracture of the subject austenites occurs by shear instability, and thus the enhancement of strain to failure and J_{IC} can be rationalized by a model which gives the condition for shear localization. Under triaxial stress-states, the transformation promotes toughening by two mechanisms. The first, as with the enhancement of uniform elongation, is by altering the flow behavior of the austenite. The second is by reducing the triaxiality as a consequence of the transformational volume expansion. The model for enhancement in ϵ_f^n and J_{IC} also predicts the existence of an optimum transformation stability condition for which the toughness is maximum. However, in many instances, this maximum is not attained due to premature failure by other lower-toughness fracture processes. For the alloys here studied, the maxima in ϵ_f^n and J_{IC} occur at M_S^c for the respective stress-states because of premature failure at $\sigma < M_S^c$ due to intrinsic brittleness of stress-assisted martensite.

The results for the resistance to crack-growth indicate that the transformation is also beneficial for this property and that there is likewise an optimum transformation stability condition for maximum toughness.

A semi-quantitative model for the relative enhancement in fracture toughness is developed here. The model indicates that, although important, dilatation is not essential for the toughening process. The volume-change contribution is not only dependent on the dilatation magnitude but also on the amount of martensite forming in the transformation zone.

A comparison of the fracture toughness obtained in this work with other values reported for high-toughness commercial steels indicate that mechanically-induced martensitic transformation can be a very substantial toughening mechanism, giving K_{IC} values up to $255 \text{ MPa}\sqrt{\text{m}}$, at a yield strength of 1300 MPa. The results here reported show that the addition of Cr spreads out the usually sharp temperature dependence of mechanical properties of metastable austenitic steels and also promotes a larger transformational volume change.

Thesis Supervisor: Dr. Morris Cohen
Title: Institute Professor, Emeritus

Thesis Supervisor: Dr. Gregory B. Olson
Title: Principal Research Associate

TABLE OF CONTENTS

<u>Chapter Number</u>		<u>Page Number</u>
	Title Page	1
	Abstract	2
	Table of Contents	4
	List of Illustrations and Figures	6
	List of Tables	12
	Acknowledgements	13
I	Introduction	15
II	Bibliographic Review	17
	2.1 - Mechanically-Induced Martensite and Transformation Plasticity	17
	2.2 - Some Aspects of Elastic-Plastic Fracture Mechanics	30
	2.3 - Ductile Fracture and Localization of Shear Deformation	38
III	Experimental Procedures	42
	3.1 - Composition of Alloys and Thermo-Mechanical Treatments	42
	3.2 - Transformation Volume-Change Measurements	49
	3.3 - Tensile Tests	53
	3.4 - Fracture Toughness Tests	56
IV	Experimental Results	60
	4.1 - Yield Strength and Transformation Behavior	60

<u>Chapter Number</u>		<u>Page Number</u>
	4.2 - Mechanical Behavior	66
	4.2.1 - Tensile Tests	66
	4.2.2 - Fracture Toughness Tests	70
V	Discussion	98
	5.1 - Transformation Behavior	98
	5.2 - Transformation Stability	105
	5.2.1 - Normalized Temperature Interval	105
	5.2.2 - Uniform Elongation Relative Enhancement	105
	5.2.3 - Strain to Failure Relative Enhancement	106
	5.2.4 - J_{Ic} Relative Enhancement	107
	5.3 - Strain Hardening and Flow Stability	115
	5.4 - Shear-Instability Controlled Fracture	122
	5.5 - The Role of the Volume Change	133
	5.6 - Transformation Toughening Model (Summary)	140
	5.7 - Comparison with Commercial Steels	148
VI	Conclusions	151
VII	Suggestions for Future Work	155
	Appendix	157
	Bibliography	164
	Biographical Note	174

LIST OF ILLUSTRATIONS AND FIGURES

<u>Figure Number</u>		<u>Page Number</u>
1	Schematic temperature dependence of the yield strength of metastable austenitic steels. The curve for strain-induced nucleation and the extension of the curve for austenitic yielding by slip at temperatures lower than M_s^σ are also shown(Reference 5)	19
2	Temperature dependence of the fracture toughness of a high-strength TRIP steel showing the enhancement due to mechanically-induced transformation(Reference,10)	19
3	Schematic curves of true-stress and volume fraction of martensite versus plastic strain for (a) strain-induced and (b) stress-assisted transformation (Reference 33)	23
4	Calculated transformation stresses and measured yield strength for TRIP steel under different stress-states(Reference 41)	23
5	Schematic closed contour used in the definition of J-integral; (a) in general and (b) ahead of the crack-tip (Reference 63)	31
6	Schematic of the region where the J-integral concept is valid(Reference 68)	35
7	Schematic temperature dependence of the effective atomic volume for martensite and austenite showing the Invar effect.	45
8	Temperature dependence of the effective atomic volume of martensite and austenite for the alloys studied in this work	50
9	Tensile specimens. Dimensions in mm.	54
10	Fracture toughness specimens. Dimensions in mm.	57

<u>Figure Number</u>		<u>Page Number</u>
11	Yield strength versus temperature. The dashed line indicates possible drop in σ_y for 31Ni(L)	61
12	Plastic uniform elongation versus temperature. The dashed line and open point indicate premature failure. The horizontal error bars indicate the uncertainty in M_d temperatures.	70
13	Strain to failure versus temperature for the lower-carbon alloys. The dashed lines and open points indicate premature failure. The horizontal error bars indicate the uncertainty in M_d temperatures	71
14	Strain to failure versus temperature for the higher-carbon alloys. The dashed lines and open points indicate premature failure	72
15	Optical micrograph of the region outside necking of 31Ni(L) tensile tested at 25°C	74
16	Optical micrograph of the region outside necking of 26Ni-4Cr(H) tensile tested at -55°C	74
17	Optical micrograph of the necked region of 34Ni-9Co(H) tensile tested at: (a) 130°C, (b) 90°C, and (c) 55°C	77
18	Low-magnification view of the shear-instability tensile fracture	79
19	High-magnification view of void-forming cracked particles in 31Ni-5Cr(L)	80
20	High-magnification view of equiaxed void-forming particles in 31Ni-5Cr(L)	80
21	Optical micrograph of the necked region of 31 Ni(L) tested at 25°C	82
22	SEM fractograph of 31Ni(L) tensile tested at 25°C showing a typical cup-and-cone fracture	82

<u>Figure Number</u>		<u>Page Number</u>
23	SEM fractograph of 26Ni-4Cr(H) tensile tested at -55°C showing some intergranular fracture	83
24	J_{Ic} versus temperature for the lower-carbon alloys. The dashed lines indicate premature failure. The horizontal error bars indicate the uncertainty in M_d temperatures. The vertical error bars represent 50% confidence level	87
25	J_{Ic} versus temperature for the higher-carbon alloys. The dashed lines indicate premature failure. The horizontal error bars indicate the uncertainty in M_d temperatures. The vertical error bars represent 50% confidence level	88
26	$dJ/d\Delta a$ versus temperature for the lower-carbon alloys. The horizontal error bars indicate the uncertainty in M_d temperatures; The vertical error bars represent 50% confidence level.	89
27	$dJ/d\Delta a$ versus temperature for the higher-carbon alloys. The horizontal error bars indicate the uncertainty in M_d temperatures. The error bars represent 50% confidence level	90
28	Optical micrograph of the crack-tip of 31Ni(L) tested at 175°C : (a) 100X, (b) 500X	92
29	Optical micrograph of the crack-tip of 31Ni(L) tested at 135°C : (a) 100X, (b) 500X	93
30	Optical micrograph of the crack-tip of 31Ni-5Cr(L) tested at -75°C : (a) 100X, (b) 500X	94
31	Optical micrograph of the crack-tip of 31Ni(L) tested at 25°C .	95

<u>Figure Number</u>		<u>Page Number</u>
32	SEM fractograph of fracture toughness specimen of 31Ni(L) tested at 25°C showing quasi-cleavage	95
33	SEM fractograph of fracture toughness specimen of 26Ni-4Cr(H) tested at -55°C showing intergranular fracture	96
34	Schematic comparison between crack-tip plastic and transformation zones at: (a) $M_s < T_1 < M_d(ct)$, (b) $T_2 = M_s^{\sigma}(ct)$, (c) $T_3 < M_s^{\sigma}(ct)$	101
35	Uniform elongation relative enhancement versus normalized temperature interval	106
36	Austenitic temperature dependence of the strain to failure of both lower- and higher-carbon alloys. The dashed line indicates the lower-carbon stable austenite baseline values used in the estimate of $\Delta \epsilon_f^n$ for $T < 135^{\circ}C$	108
37	Strain to fracture absolute enhancement versus normalized temperature interval	110
38	Austenitic temperature dependence of J_{Ic} for both lower- and higher-carbon alloys. The dashed line indicates the lower-carbon stable austenite baseline values used in the calculation of $\Delta J_{Ic}/J_{Ic}(aust)$ for $T < 135^{\circ}C$	111
39	J_{Ic} relative enhancement versus normalized temperature interval	113
40	True-stress and strain-hardening rate versus true-plastic-strain up to necking for 31Ni(L) tested at 90°C	116
41	True-stress and strain-hardening rate versus true-plastic-strain up to necking for 31Ni(L) tested at 25°C	117
42	True-stress and strain-hardening rate versus true-plastic-strain up to necking for 31Ni(L) tested at -75°C	118

<u>Figure Number</u>		<u>Page Number</u>
43	True-stress and strain-hardening rate versus true-plastic-strain up to necking for 26Ni-4Cr(H) tested at 0°C and -55°C	120
44	Optical micrograph of the necked region of 31Ni(L) tested at 175°C	125
45	Optical micrograph of the necked region of (a) 34Ni-9Co(H) and (b) 26Ni-4Cr(H) tested at 130°C	128
46	J_{IC} relative enhancement versus transformation zone half-height	134
47	J_{IC} relative enhancement versus amount of martensite in the transformation zone	135
48	$k(\Delta V/V)$ versus relative transformational volume change	137
49	Schematic uniform elongation relative enhancement, strain to failure absolute enhancement, and J_{IC} relative enhancement versus normalized temperature interval	141
50	Schematic true-stress, true-plastic-strain curves at (a) $T_1 > M_d$, (b) $T_2 \leq M_d$, (c) T_3 when maximum in toughness is attained, (d) $T_4 < T_3$	142
51	Schematic temperature dependence of plastic strain. It shows the dependences of stable austenite strain to failure and the strain for the onset of necking, the dependences of the strain corresponding to the two inflections in the curves σ versus ϵ promoted by mechanically-induced transformation, and also the increase in ϵ_f^n and ϵ_{pu} due to the transformation. The maximum in ϵ_{pu} and ϵ_f^n are observed respectively in the temperature intervals ΔT_1 and ΔT_2 .	144

Figure
Number

Page
Number

52	Schematic true-stress, true-plastic-strain curves for different temperatures showing possible premature failure by other fracture process described by $\epsilon_f(\sigma)$: (a) $T_1' > M_d$, (b) $T_2' \leq M_d$, (c) T_3' when premature failure prevails	145
53	Comparison of fracture toughness of the alloys studied here and commercial steels	149
A1	J versus Δa curves for 36Ni-4Cr(H)	159
A2	J versus Δa curves for 31Ni-5Cr(L)	160
A3	J versus Δa curves for 26Ni-4Cr(H)	161
A4	J versus Δa curves for 31Ni(L)	162
A5	J versus Δa curves for 34Ni-9Co(H)	163

LIST OF TABLES

<u>Table Number</u>		<u>Page Number</u>
I	Composition of Alloys in wt%	43
II	Selected Treatments	47
III	Relative Transformational Volume-Change of Metastable Alloys	51
IV	M_s , M_s^σ , and M_d for Uniaxial Tension, Necked Region, and Crack-Tip	63
V	Tensile Properties of 36Ni-4Cr(H)	67
VI	Tensile Properties of 31Ni-5Cr(L)	67
VII	Tensile Properties of 26Ni-4Cr(H)	68
VIII	Tensile Properties of 31Ni(L)	68
IX	Tensile Properties of 34Ni-9Co(H)	69
X	Fracture Properties of 36Ni-4Cr(H)	84
XI	Fracture Properties of 31Ni-5Cr(L)	84
XII	Fracture Properties of 26Ni-4Cr(H)	85
XIII	Fracture Properties of 31Ni(L)	85
XIV	Fracture Properties of 34Ni-9Co(H)	86
XV	Calculated Plastic Zones and Measured Transformation Zone Sizes	103

ACKNOWLEDGEMENTS

I wish to acknowledge several people whose help made this work possible. Thanks to:

- Professor Morris Cohen for his interest in bringing me to MIT, for his guidance and technical advice throughout the work, for his enthusiasm and incentive, and also for his personal kindness to me and my family;

- Dr. Gregory B. Olson for an almost daily basis technical guidance and advice, for his interest, enthusiasm and incentive in the work, and also for his friendship;

- Professor A.S.Argon, R.M.Pelloux, D.M.Parks and I-Wei Chen for helpful discussions;

- Marge Meyer for her kindness in all instances, either in solving administrative problems or in being very friendly to me and my family;

- Mim Rich for her technical help, and also for her kindness on all occasions;

- many people who helped in the experimental work, including: Len Suddenfield, Elizabeth Shaw, Joe Adario, Ken Rich, Art Gregor, Chester Wieleba and Peter Neshe;

- many colleagues who helped make life at MIT highly enjoyable; apologizing for names involuntarily missed, I mention: Sue Best, Mica Grujicic, Chen-Yih Hsu, Ana Sarosiek, Kaneaki Tsuzaki, Joe Goss, Paul Wleyshman, Harold Clark, Tom Kelly, Keith Taylor, Dennis Haezebrouk, Eric Kvam and Paul Adler;

Portions of the text
on the following page(s)
are not legible in the
original.

- the "Brazilian community" for helping make life outside MIT highly enjoyable;

- Comissão Nacional de Energia Nuclear (CNEN), an agency of the Ministry of Mines and Energy of Brazil, for sponsoring me and my family throughout these four years;

- Secretaria de Tecnologia Industrial (STI), an agency of the Ministry of Industry and Commerce of Brazil, for providing a complementation to my main scholarship;

- ONR, NSF, and DOE for supporting various aspects of the research project;

- my parents, brother, sisters and in-laws for their incentive and support throughout the years and distance.

This thesis is dedicated to my wife Vania and daughter Priscila, for their encouragement, understanding and patience during the long hours and days taken from my family for my graduate studies at MIT.

(Alloys provided by Prof. J.J.Morris, Jr., U.Cal.-Berkeley, and Dr. R.J.Ault, Republic Steel)

CHAPTER I : INTRODUCTION

It has been recognized that metastable austenitic steels can exhibit high strength associated with large uniform ductility. This excellent combination of properties is a direct consequence of the martensitic transformation taking place under mechanically-applied stresses.

It is also reported that the same transformation is responsible for the enhancement of fracture toughness in these materials when compared with stable austenitic steels. Although theories based on the absorption of strain energy by the transformation account for the improvement of fracture toughness in an approximate way, a more complete understanding of how martensitic transformation enhances the general toughness of metastable austenitic alloys is needed.

In this work, tensile properties and fracture toughness using the J-integral method of five different precipitation-hardenable metastable austenitic steels are studied as a function of temperature. While one of the alloys does not transform in the temperature range studied (-196°C to 300°C), the other four show different stabilities with respect to the martensitic transformation as well as different transformation volume changes. The transformation is shown to produce enhancement in ductility and toughness as measured by any of the four parameters: uniform elongation (ϵ_{pu}), strain to failure in the neck (ϵ_f^n), J_{Ic} , and $dJ/d\Delta a$, where

the last is an indication of the material resistance to crack growth.

A generalized formalism to explain the enhancement in ductility and toughness is developed based on the study of the influence of mechanically-induced martensitic transformation on the flow behavior of metastable austenitic steels. This formalism is able to explain the results obtained for ϵ_{pu} , ϵ_f^n , and J_{Ic} , all under Mode I loading. The influence of the volume expansion associated with the martensitic transformation on the toughness enhancement under triaxial stress-states has been rationalized and a final expression showing the dependence of the relative enhancement in J_{Ic} on the extent of the transformation and the relative transformation volume change has been achieved.

2.1 - Mechanically-Induced Martensite and Transformation Plasticity

Although it has been a long time since the first attempts were made to explain how applied stresses interact with martensitic transformation⁽¹⁾, only during the 50's an adequate rationalization of the problem was obtained. Patel and Cohen⁽²⁾ showed that the mechanical work performed on or by the transforming region, as the resolved normal and shear forces are carried through the repective transformation displacements, should contribute to the thermodynamic driving force. This work term is expressed as:

$$W = \tau \gamma_0 + \sigma_n \epsilon_0 \quad [1]$$

where γ_0 and ϵ_0 are the shear and normal components of the transformation invariant-plane shape strain, τ and σ_n are the shear and normal stresses resolved in the planes and directions of γ_0 and ϵ_0 .

Mechanically-induced martensitic transformations are usually classified as stress-assisted or strain-induced⁽³⁾. In the former case, the plates nucleate at sites already present in the parent phase and the process is thermodynamically assisted by the applied stresses, while in the latter case, the matensite nucleates at new sites created by plastic deformation of the parent phase⁽³⁾. The

temperature dependence of the yield strength for materials where mechanically-induced martensitic transformation takes place is shown schematically in Figure 1. At temperatures below M_S^σ (4), the transformation is stress-assisted and initial yielding is controlled by the macroscopic strain accompanying the transformation. At temperatures above M_S^σ , initial yielding is controlled by slip in the parent phase, and the yield-strength curve follows the normal temperature dependence of the yield-strength of the parent phase. Between M_S^σ and M_d , the curve of strain-induced nucleation is shown to fall between the curve of the actual yield-strength versus temperature and that extrapolated from the stress-assisted range of temperatures. This is consistent with the nucleation at new sites created by plastic deformation. M_d is the highest temperature at which strain-induced transformation is found to occur. At still higher temperatures fracture precedes any detectable martensite formation.

It is known that martensitic transformation can produce plastic deformation of adjacent austenite. When the transformation takes place under an applied stress, it is accompanied by a macroscopic strain, defined as transformation plasticity, which can arise from a biasing of the plastic accommodation processes around the martensitic units, as well as a biasing of the plate variants formed (5). This transformation plasticity has been shown to inhibit flow instability (necking) by increasing the strain-hardening

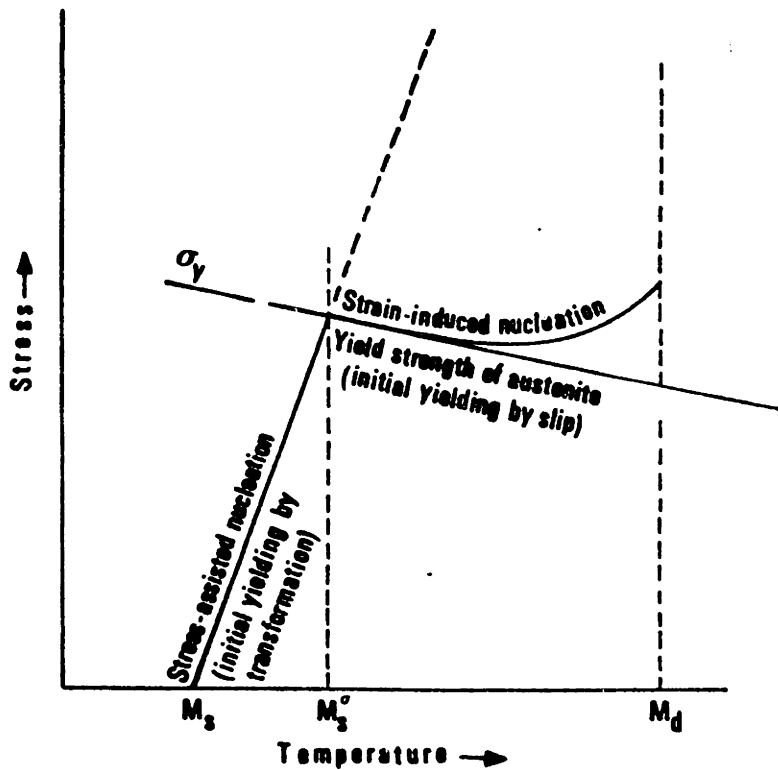


Figure 1 - Schematic temperature dependence of the yield strength of metastable austenitic steels. The curve for strain-induced nucleation and the extension of the curve for austenitic yielding by slip at temperatures lower than M_s^σ are also shown (Reference 5).

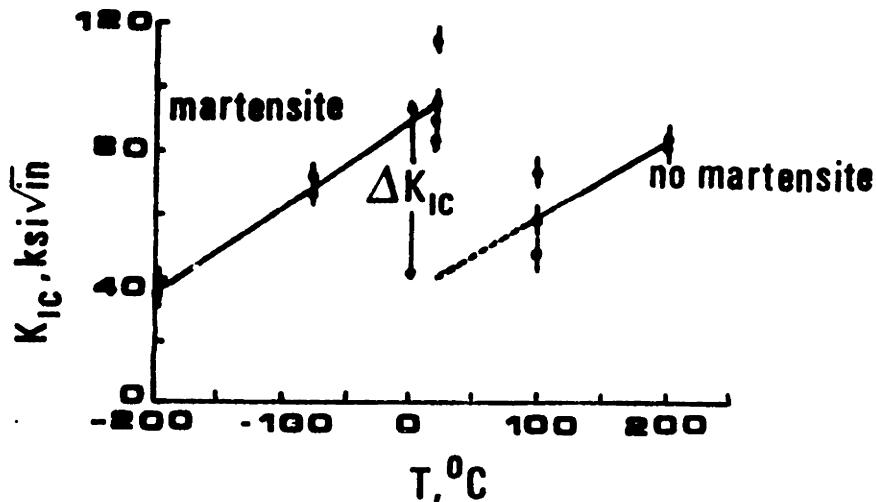


Figure 2 - Temperature dependence of the fracture toughness of a high-strength TRIP steel showing the enhancement due to mechanically-induced transformation (Reference 10).

rate⁽⁶⁾. This increase of strain-hardening, coupled with the suppression of early necking results in an overall increase of tensile strength and uniform ductility⁽⁶⁾.

These ideas, initially developed in lower strength steels⁽⁶⁾, have been successfully applied to very high-strength steels, the so-called TRIP (Transformation Induced Plasticity) steels⁽⁷⁾. Subsequently many papers have appeared dealing with the influence of mechanically-induced martensitic transformation on the general mechanical behavior of metastable austenitic steels under monotonic⁽⁸⁻²²⁾ and cyclic⁽²³⁻²⁹⁾ loading.

Dealing specifically with fracture toughness under monotonic loading, there are indications that TRIP steels do have high toughness^(8-10,18-22). Based on the hypothesis that the transformation of austenite to martensite is equivalent to a mode of plastic deformation and thus capable of absorbing strain energy that otherwise would have driven crack extension^(9,10), Gerberich et al.⁽⁹⁾ and Antolovich and Singh⁽¹⁰⁾ have calculated the enhancement of fracture toughness due to the TRIP phenomenon. In the Antolovich and Singh work⁽¹⁰⁾, a comparison between calculated and experimental values apparently supported their model.

The Antolovich and Singh experimental procedure consisted of measuring K_{Ic} as a function of temperature for a high-carbon (0.6C) and severely warm-worked (75% at 460°C) TRIP steel, with the result shown in Figure 2. At room temperature and below, mechanically-induced martensite was

formed, while at higher temperatures no martensite was observed even at the fracture surfaces. A comparison between the actual K_{Ic} at room temperature and the value obtained from extrapolation of the higher-temperature tests gave the enhancement of fracture toughness due to martensitic transformation.

From a theoretical point of view, Antolovich and Singh⁽¹⁰⁾ calculated the dissipation of energy associated with the transformation as a work term obtained by the product of the stress at which martensite forms and the shear component of the invariant-plane shape strain. They considered that the martensite forms by a strain-induced mechanism, and in this case some of their hypotheses are justified, such as the assumption that the properties of austenite determine the plastic zone size (which is taken equal to the transformation zone), and also the assumption that martensite forms ahead of the crack tip at the equivalent yield strength of the material⁽¹⁰⁾. However, these hypotheses are unreasonable when the transformation is stress-assisted at the crack-tip. In this case, although the plastic zone is again equal to the transformation zone, yielding is controlled by the transformation itself and the martensite forms at equivalent stress level much lower than the tensile yield strength of the material⁽³⁰⁾. Furthermore, Antolovich and Singh only considered enhancement in fracture toughness due to the shear component of the transformation strain,

neglecting any possible contribution of the transformation volume change, which seems to play a key role in the transformation fracture-toughness enhancement observed in ceramic systems⁽³¹⁾.

These limitations to the Antolovich and Singh model justify further investigation of the transformation toughening problem in an attempt to reach a more basic understanding of the phenomenon.

A schematic representation of the true tensile stress-strain curves for temperatures ranges where the transformation is stress-assisted and strain-induced is shown in Figure 3⁽³³⁾, together with the respective transformation curves. The very distinct behavior of the material in each range is evident. When the transformation is stress-assisted, the martensite volume fraction (f) is directly proportional to the plastic strain (ϵ). The high dynamic softening is such that the stress is kept at a very low value, lower than the predicted flow curves for austenite and martensite or for a linear mixture of the two. A relatively sharp increase toward the "mixture" flow curve is observed when the transformation is exhausted. On the other hand, when the transformation is strain-induced, under the assumption that shear-band intersections constitute the primary strain-induced nucleation site⁽³⁴⁻³⁸⁾, the transformation curve can be described by an expression of the form⁽³⁴⁾:

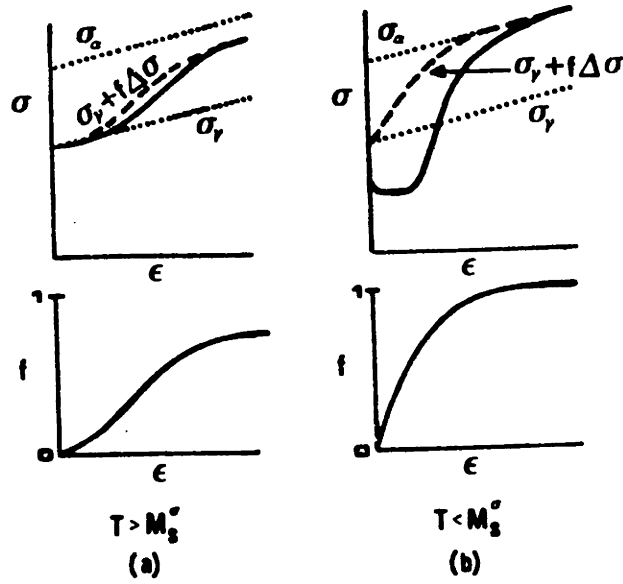


Figure 3 - Schematic curves of true-stress and volume fraction of martensite versus plastic strain for (a) strain-induced and (b) stress-assisted transformation (Reference 33)

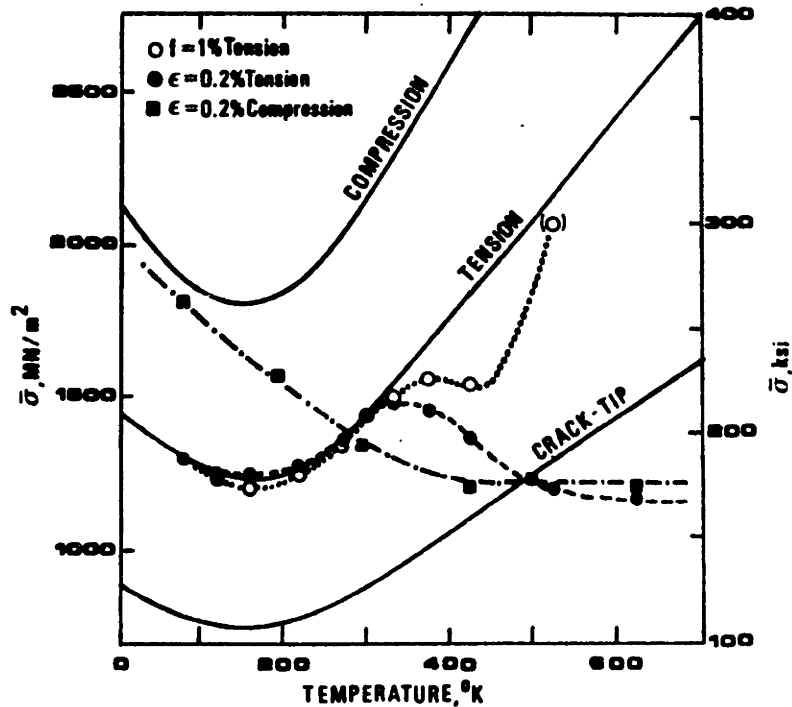


Figure 4 - Calculated transformation stresses and measured yield strength for TRIP steel under different stress-states (Reference 41).

$$f = 1 - \exp(-\beta [1 - \exp(-\alpha \epsilon)^n]) \quad [2]$$

where α is a dimensionless parameter related to the rate of shear-band formation, β is proportional to the probability that a shear-band intersection acts as a nucleation site, and n is a power-law parameter ($n \geq 2$). In this case, the dynamic softening, although present, is much smaller and the stress-strain curve is not very different from the one predicted by the rule of mixtures.

Recently, constitutive equations have been theoretically developed for both temperature ranges, when the martensite is stress-assisted⁽³⁰⁾ and strain-induced⁽³²⁾. In TRIP steels the basic mode of transformation on cooling is isothermal. Kinetic theories of isothermal martensitic transformation^(39,40) predict that the transformation rate varies as a function of the total applied driving force (ΔG) according to:

$$\dot{f} = (n_i + pf - N_v)(1-f)V\nu \exp -(A+B\Delta G)/RT \quad [3]$$

where n_i is the initial density of nucleation sites, p is the autocatalytic parameter, f is the volume fraction of martensite, N_v is the number of martensitic plates per unit volume, V is the instantaneous mean martensitic plate volume, ν is the lattice vibration frequency, R is the gas constant, T is absolute temperature, and A and B are constants.

Taking into account that when stress-assisted martensite is formed, $(-\Delta G)$ is the sum of the chemical driving force $(-\Delta G_{ch})$ and the additional driving force due to the interaction of applied stresses and the strain associated with the transformation (Equation 1), the general constitutive equation for TRIP steels in the stress-assisted range of temperatures is then⁽³⁰⁾,

$$\bar{\sigma}_t(\dot{f}) = -\left(\frac{Bd\Delta G}{d\bar{\sigma}}\right)^{-1} \left[A+B \Delta G_{ch} + RT \ln \frac{\dot{f}}{(n_i + pf - N_v)(1-f)VU} \right] \quad [4]$$

where $\bar{\sigma}_t(\dot{f})$ is the equivalent stress required for transformation at rate \dot{f} , which is related to the imposed strain rate through:

$$\dot{f} = k \dot{\epsilon} \quad [5]$$

Equation 4 also denotes the temperature dependence of the equivalent yield strength which is dependent on the stress-state through $d\Delta G/d\bar{\sigma}$ ⁽³⁰⁾. Figure 4 shows the theoretical temperature dependence of the equivalent yield strength based on Equation 4 for three different stress-states. The model predicts a much lower transformation stress ahead of the crack tip, a consequence of the influence of stress triaxiality on $d\Delta G/d\bar{\sigma}$ ⁽⁴¹⁾. Figure 4 also shows that there is good agreement between the theory and experimental results for the tensile yield strength in the

temperature range where the transformation is stress-assisted.

In the temperature range where transformation is strain-induced, constitutive equations have been developed based on results for metastable austenitic steels⁽³²⁾. In this case the static hardening contribution to the flow stress is expressed as:

$$\sigma_s(\epsilon) = (1-f) [\sigma_\gamma(\epsilon - \alpha'f)] + f [\sigma_\alpha(\epsilon - \alpha'f)] \quad [6]$$

where f is the volume fraction of martensite at a strain ϵ and σ_γ and σ_α are the pure austenite and pure martensite flow stresses at a strain $(\epsilon - \alpha'f)$. Here $\alpha'f$ corrects for the shape-strain contribution to the measured ϵ ⁽⁵⁾. The dynamic softening contribution, $\Delta\sigma_d$, is related to σ_s through⁽³²⁾:

$$\frac{\Delta\sigma_d}{\sigma_s} = \beta' \frac{df}{d\epsilon} \quad [7]$$

with β' for the studied metastable austenitic steel equal to 5.3×10^{-2} . The constitutive flow relation for strain-induced transformation is then given by:

$$\sigma = \left((1-f) [\sigma_\gamma(\epsilon - \alpha'f)] + f [\sigma_\alpha(\epsilon - \alpha'f)] \right) \times \left[1 - \beta' \frac{df}{d\epsilon} \right] \quad [8]$$

In terms of stability of plastic flow, from a continuum point of view, the ideal hardening curve would be the one described by⁽⁵⁾:

$$\frac{d\sigma}{d\epsilon} = \sigma \quad [9]$$

or, in other words:

$$\sigma = \sigma_0 \exp \epsilon \quad [10]$$

The transformation-plasticity effects of dynamic softening and static hardening bring the shape of the stress-strain curve almost exactly to that of the ideal exponential hardening curve⁽⁵⁾ and this is the explanation for the high values of uniform elongation obtained in metastable austenitic alloys under appropriate stability conditions.

Transformation toughening can be obtained not only in steels but also in ceramic systems where tetragonal zirconia (ZrO_2) is present as a dispersed phase or precipitates^(31,42,43). The martensitic transformation of the tetragonal ZrO_2 into a monoclinic structure under stresses ahead of a crack-tip is known to increase the fracture toughness of the material through the shielding of the crack tip from the applied stress, in a manner analogous to the plastic zone in ductile materials⁽⁴⁴⁾. Two approaches for the quantitative analysis of the problem have been used:

a) an energetic approach, where the enhancement in toughness is modelled by examining the energy changes that accompany crack extension^(45,46); b) a mechanics approach, where the reduction in near-tip stress intensity relative to the applied stress intensity is calculated⁽⁴⁷⁾. In both approaches only the dilatant part of the transformation is taken into account, since the overall transformation shear strain is low in these systems⁽⁴⁶⁾.

In the formalism of the mechanics approach, Hutchinson⁽⁴⁸⁾ recently developed constitutive equations for an elastic solid containing particles that undergo an irreversible stress-induced dilatant transformation. Based on these equations, he calculated the reduction in crack-tip stress intensity and showed that toughening is associated with the crack advance and is due to the wake of transformed particles which are left behind a quasi-statically advancing crack-tip⁽⁴⁸⁾. The highest toughening is obtained in the so-called supercritically transforming composite where, in any region of the material when the mean stress reaches a critical value (σ_m^c), all the particles are completely transformed. The crack-tip stress-intensity reduction is given by⁽⁴⁸⁾:

$$K = K - K_{\text{tip}} = 0.2143 \frac{E \theta^T \sqrt{H}}{(1 - \nu)} \quad [11]$$

where E is the Young modulus, ν is the Poisson's ratio, H is the half-height of the wake of transformed particles and θ^T is the total dilatation of the transformed composite related to each particle dilatation (θ_p) by:

$$\theta^T = c \theta_p \quad [12]$$

c being the particle volume fraction. Considering the possibility of the transformation occurring in a range of stresses and consequently the existence of partially transformed regions (subcritically transforming composite), the crack-tip stress-intensity reduction can be considerably less than the values predicted by Equation 11⁽⁴⁸⁾.

Despite all these efforts in modeling the transformation toughening in ceramic systems, comparison with experimental results suggests that the theoretical models underestimate the measured toughness enhancement (44,47,48). This seems to indicate that distortional components of transformation together with possible preferred orientation effects may have to be taken into account along with the dilatant component⁽⁴⁸⁾.

2.2 - Some Aspects of Elastic-Plastic Fracture Mechanics

When dealing with low-strength, high-toughness materials, the Linear Elastic Fracture Mechanics small-scale yielding assumption fails, and it becomes necessary to invoke new concepts valid for elastic-plastic behavior. One such concept is the so-called J-integral formulation.

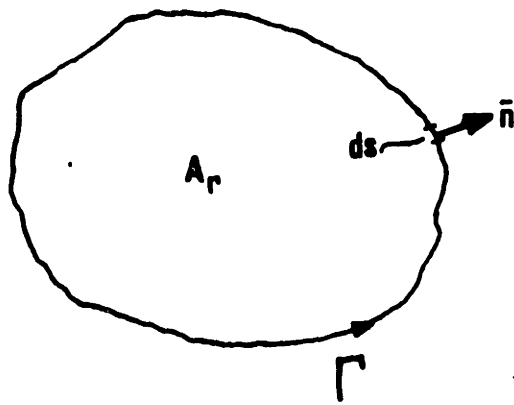
The J-integral was originally defined for a nonlinear elastic material as⁽⁴⁹⁾:

$$J = \int_{\Gamma} W dy - T \left(\frac{\partial u}{\partial x} \right) ds \quad [13]$$

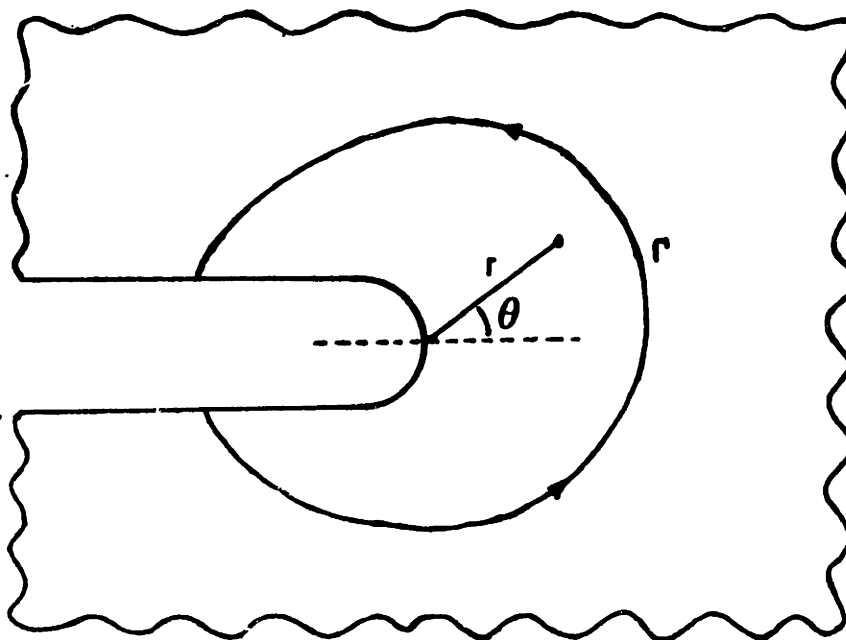
where Γ is a two-dimensional closed contour followed counter-clockwise in a stressed solid, as shown in Figure 5a. T is the traction force perpendicular to Γ pointing in the outward direction ($T_i = \sigma_{ij} n_j$), u is the displacement in the x-direction, ds is an element of Γ , and W is the strain energy per unit volume:

$$W = W(x,y) = W(\epsilon) = \int_0^{\epsilon} \sigma_{ij} d\epsilon_{ij}. \quad [14]$$

It has been shown⁽⁴⁹⁾ that the J-integral is path independent when the contour is taken around a crack tip with its initial and final points respectively in the upper and lower surfaces of the crack (Figure 5b). Furthermore, the J-integral defined along this same contour is a measure of the change in potential energy (π) when the initial crack



(a)



(b)

Figure 5 - Schematic closed contour used in the definition of J-integral: (a) in general and (b) ahead of the crack-tip (Reference 63).

length, a , is infinitesimally extended^(49,50):

$$J = - \frac{\partial \pi}{\partial a} \quad [15]$$

By choosing a circle as the contour Γ , by invoking the path-independent property of the integral, and by assuming a power-law stress-strain relationship in a nonlinear elastic material, Hutchinson⁽⁵¹⁾ and Rice and Rosengren⁽⁵²⁾ were able to derive crack-tip stress and strain fields, whose dominant terms at distances close to the crack tip are:

$$\sigma_{ij} = \sigma_0 \left[\frac{J}{\alpha \sigma_0 \epsilon_0 I_n r} \right]^{1/(N+1)} f_{ij}(\theta)$$

$$\epsilon_{ij} = \sigma_0 \left[\frac{J}{\alpha \sigma_0 \epsilon_0 I_n r} \right]^{N/(N+1)} f_{ij}(\theta) \quad [16]$$

where N is the inverse of the strain-hardening coefficient n , σ_0 and ϵ_0 are the initial yield stress and strain, α is the constant in the stress-strain law, I_n is a numerical constant dependent on n , r is the radial distance from the crack tip, and $f_{ij}(\theta)$ and $g_{ij}(\theta)$ are functions of the angle measured counterclockwise from the plane ahead of the crack tip (Figure 5b).

These equations show that the J -integral can be considered a stress-field parameter. Furthermore, as the

J-integral is a measure of the change in potential energy, it is equivalent to the crack extension force G in the limit of linear elasticity⁽⁵³⁾.

All these concepts are rigorously correct for nonlinear elastic materials but they can be extended to elastic-plastic materials under the assumption of the deformation theory of plasticity⁽⁴⁹⁾. This theory assumes that elastic-plastic materials behave exactly the same as a nonlinear elastic material when loaded, with infinitesimal increments in strain at any point proportional to the strain at that point. On unloading, the two materials will behave differently: the nonlinear elastic material will follow the reversed loading path while the elastic-plastic material will not.

The concept of J-integral as a field intensity parameter allows the use of J as a fracture toughness parameter^(54,55). The critical value of J-integral that will correspond to the initiation of crack extension is J_c and for tensile crack-opening Mode I it is called J_{Ic} . The equivalence between J and G allows J_{Ic} and K_{Ic} to be related through⁽⁵³⁾:

$$J_{Ic} = G_{Ic} = \frac{K_{Ic}^2}{E'} \quad [17]$$

where $E'=E$ for plane stress and $E'=E/(1 - \nu^2)$ for plane strain.

The experimental techniques for J_{Ic} determination are based on the measurement of J-integral as a function of crack extension (Δa) (54-59). Two techniques are standardized⁽⁶⁰⁾. One uses multiple specimens with the same initial crack length⁽⁵⁸⁾. Each specimen has its initial crack extended to different values of Δa , with the crack length displacement in steels measured by heat tinting. The other standard technique uses a single specimen that is unloaded at different values of Δa , with the crack extension determined by measurement of the compliance variations⁽⁵⁹⁾. A non-standard technique has been recently proposed⁽⁶²⁾ in which the J versus Δa curve can be constructed directly from the load-displacement curve of one single specimen.

The concept of J-integral as a fracture toughness parameter is based on the assumption that a region exists near the crack tip where the stress and strain fields are governed by Equation 16. This imposes geometrical requirements to be satisfied by the specimens used to measure J_{Ic} . First, the size of the J-dominated field region (r_{HRR}) must be larger than the small region very near the crack tip where nonproportional loading occurs (Figure 6). Second, the expressions in Equation 16 must be asymptotically true in the limit $r \rightarrow 0$, and this means that the uncracked ligament must be sufficiently large to assure that the fully plastic field solution can be neglected at regions near the crack tip⁽⁶³⁾. The size of the nonproportional loading region is 2

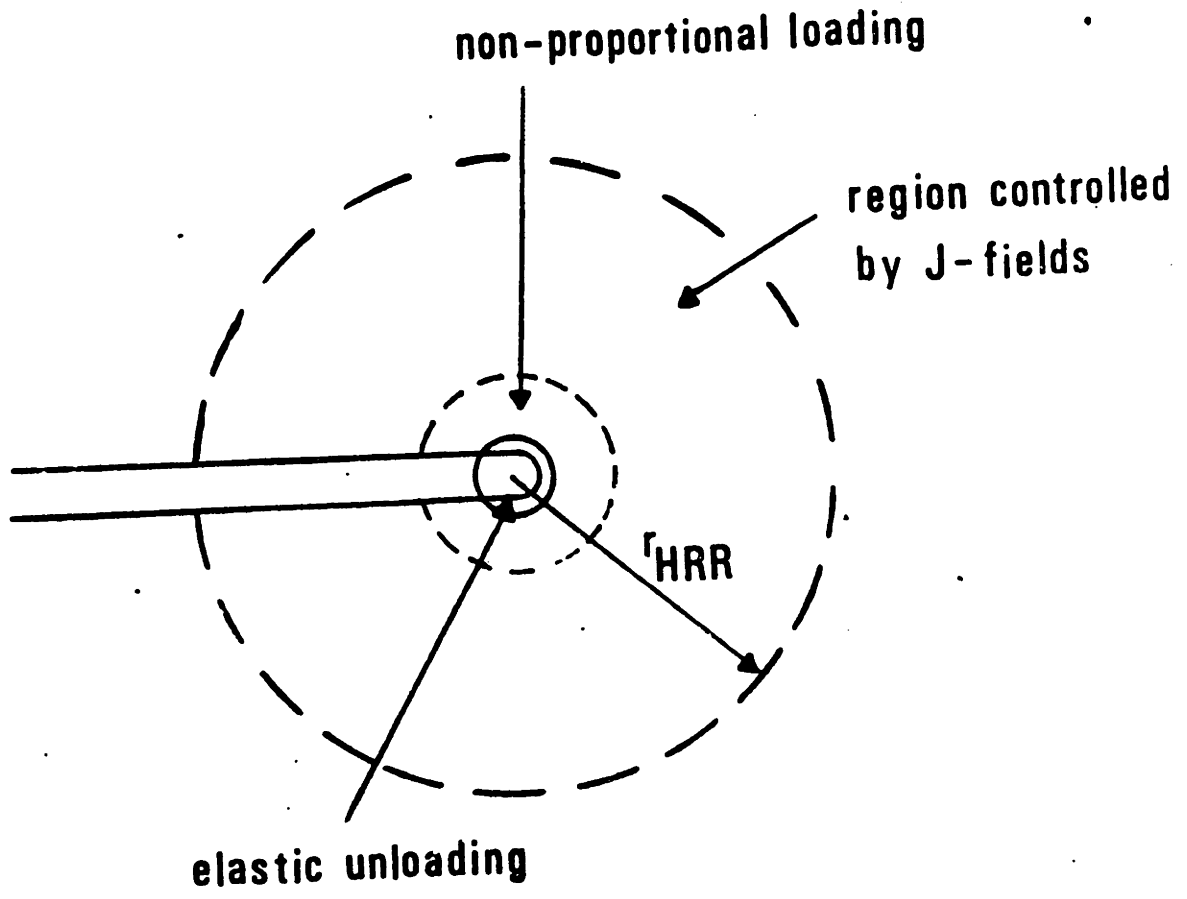


Figure 6 - Schematic of the region where the J-integral concept is valid (Reference 68)

to 3 times larger than the crack-tip-opening displacement of a blunted crack^(64,65). The nonproportional loading region corresponds to the region of large shear strains introduced ahead of the crack tip due to blunting^(66,67).

The required uncracked ligament size is a function of the material strain-hardening coefficient and the crack geometry^(64,65). For bend-type specimens (three-point bend and tensile compact) of materials of any strain-hardening coefficient⁽⁶⁸⁾, the size of the initial uncracked ligament, b , must satisfy:

$$b \geq 25 \frac{J_{Ic}}{\sigma_{flow}} \quad [18]$$

where σ_{flow} is an average value between yield strength and ultimate strength⁽⁶⁰⁾.

Although the concept of J-integral as a fracture parameter has been developed for stationary cracks, the experimental J versus Δa curves may be interpreted as a crack-growth resistance curve if certain requirements are satisfied, namely⁽⁶⁸⁻⁷⁰⁾:

$$a \ll r_{HRR} \quad \text{and} \quad [19]$$

$$w = \frac{b}{J} \left(\frac{dJ}{d\Delta a} \right) \gg 1$$

When these conditions are satisfied, a nondimensional parameter, the tearing modulus (T_m), can be defined as a measure to the resistance of ductile materials to tearing instability⁽⁶⁸⁻⁷¹⁾:

$$T_m = \frac{E}{\sigma_{flow}} \left(\frac{dJ}{d\Delta a} \right) \quad [20]$$

Besides the J-integral approach to elastic-plastic fracture mechanics, the concept of a critical crack-tip opening displacement (CTOD) required for crack propagation is also widely used⁽⁷²⁾. The relation between J_{Ic} and CTOD is expressed as⁽⁶⁴⁾:

$$J_{Ic} = M \times CTOD \times \sigma_y \quad [21]$$

where σ_y is the yield strength and M is a function of the strain-hardening coefficient and the ratio σ_y/E .

2.3 - Ductile Fracture and Localization of Shear Deformation

It is well established that the fracture process in ductile materials occurs by the formation and ultimately impingement of voids formed around precipitates or second-phase particles⁽⁷³⁻⁷⁷⁾, with these particles ranging in size from a few Angstroms to several microns⁽⁷⁸⁾.

The voids are nucleated either due to brittle cracking of the particles^(79,80) or by decohesion of the particles-matrix interface^(76,80-86) caused by deformation incompatibilities between particle and matrix. Apparently elongated particles are more susceptible to cracking^(81,82) while equiaxed ones almost always nucleate voids by interfacial separation⁽⁸²⁾.

Many different theories have been proposed for void-nucleation^(76,80,82-86). Some of these models are dislocation-based^(80,85), while others are continuum-based^(82,86). A necessary but not sufficient condition for void formation is that the locally concentrated elastic strain energy released compensates for the surface energy created^(76,87). The additional requirement to be met for void formation is sometimes expressed as the attainment of a critical value of plastic strain in the region surrounding the particle^(84,86). More recently, Argon^(82,83) proposed a mechanism in which beyond the necessary energy condition, voids are formed when the tensile stress acting on the particle-matrix interface reaches a critical value. The value of the critical stress is dependent on the nature of

the particle, matrix and their bonding. The interfacial tensile stress is a function of both the flow and hydrostatic stress in the region where the particle is situated⁽⁸²⁾. The critical stress criterion has been experimentally verified in some cases^(83,88).

After the voids are nucleated, continued plastic deformation promotes their growth. Growth models have been developed for cylindrical and spherical particles in a triaxial stress-state^(89,90). These growth models show that high stress-triaxiality and low strain-hardening will drastically decrease the strain to fracture^(89,90).

The final stage of void coalescence has been less analysed. A geometrical model has been proposed in which elliptical voids coalesce by shear deformation on planes located at 45° to their major axis⁽⁹²⁾. More recently, Gurson^(93,94) developed a flow rule as well as a constitutive relation for a progressively cavitating ductile solid.

In some instances, under plane strain conditions in ductile metals, the fracture crack does not propagate in a flat mode but rather in a zig-zag fashion. This type of fracture has been observed in a variety of materials including copper⁽⁷⁵⁾, maraging steels⁽⁹⁵⁻⁹⁷⁾, 4340 steels^(97,98) and nonferrous alloys⁽⁹⁹⁾. The ridges are observed to form at approximately 45° to the macroscopic crack-propagation plane and the wavelength of these zig-zags varies from a few microns to 1 mm.⁽⁹⁷⁾ These zig-zags have been observed in the center of tensile specimens after

necking⁽⁷⁵⁾, as well as in Charpy impact, dynamic tear-energy, and fracture-toughness specimens⁽⁹⁷⁾. The microscopic fracture process along the ridges of the zig-zags in all cases are by void nucleation, growth and coalescence⁽⁹⁷⁾.

Many models have been proposed to explain the zig-zag type of fracture^(76,95-103). Berg⁽¹⁰¹⁾ proposed that a large number of microvoids will be present within the plastic zone in the region near the crack tip as a consequence of triaxial stresses acting on inclusions. Fracture will occur by shear instabilities connecting the voids in a zig-zag path along the zones of highly localized shear strain⁽¹⁰¹⁾. McClintock⁽¹⁰⁰⁾ proposed a combined triaxial stress/critical shear strain failure criterion for the microvoid fracture process along the ridges. Based on the slip-line flow-field for sharp cracks in nonhardening materials, the model suggests that the crack will propagate along the planes at 45° to the macroscopic fracture surface where hydrostatic stress and shear strain are maximum⁽¹⁰⁰⁾.

More recently, Van den Avyle⁽⁹⁷⁾ extended McClintock's criterion by suggesting that the crack propagates at 45° to the macroscopic fracture plane along a plane of constant hydrostatic stress but decreasing plastic strain. The crack changes direction when the local combination of plastic strain and hydrostatic stress is too low to satisfy the critical condition for void-sheet formation⁽⁹⁷⁾. The crack then follows a higher plastic-strain field line at 90° downward to the original direction of crack propagation.

The zig-zag fracture process then repeats itself⁽⁹⁷⁾.

Although experimental results were explained based on the critical hydrostatic stress/plastic strain criterion^(96,97), this model does not consider the modification in the slip-line flow field due to blunting^(66,67).

All models for zig-zag fracture suggest that the process is a consequence of localization of shear deformation that ultimately leads to failure by shear instability. Based on previous work⁽¹⁰⁴⁻¹⁰⁷⁾ which associates the onset of localization with a material instability, using a continuum approach, Rice developed a theory for shear-band formation⁽¹⁰⁸⁾. His theory has been extensively applied to axisymmetric-tension and plane strain problems in ductile materials⁽¹⁰⁹⁻¹¹³⁾. These studies suggest that the critical requirements for the onset of shear localization are strongly dependent on the local strain-hardening rate, triaxiality and parameters related to the void formation process⁽¹⁰⁹⁻¹¹³⁾. Using a direct numerical approach Tvergaard arrived at these same conclusions^(114,115).

Very recently Tvergaard and Needleman⁽¹¹⁷⁾, using finite element methods and the constitutive formalism proposed by Gurson^(93,94), were able to simulate the fracture process in the necking region of a material under axisymmetric tension. Their results showed the zig-zag fracture process in the interior of the specimen⁽¹¹⁷⁾.

CHAPTER III : EXPERIMENTAL PROCEDURE

3.1 - Composition of Alloys and Thermomechanical Treatments

The present research was conducted on precipitation-hardenable low-carbon Fe-Ni-Ti based metastable austenitic steels. The five studied compositions as determined by chemical analysis are shown in Table I. Henceforth each alloy will be designated by its Ni and Co or Cr content and also a letter L or H indicative of the lower ($\approx 0.004w\%$) or higher ($\approx 0.012w\%$) carbon content. For instance, the first alloy in Table I will be referred to as the 36Ni-4Cr(H) alloy.

The difference in carbon content between the alloys was not intentional but occurred because the alloys were produced by different suppliers. The small difference in carbon content has a significant influence on the mechanical response of each group of alloys (L and H).

The alloy compositions were designed for mechanical-property comparisons between stable and metastable steels and also between metastable steels with different relative volume-changes associated with the deformation-induced martensitic transformation. Unless otherwise stated, in this work the words stable and metastable refer to the relative lower or higher tendency for mechanically-induced martensitic transformation.

The first alloy-design objective was to achieve, after all thermal and thermomechanical treatments, fairly

TABLE I : COMPOSITION OF ALLOYS IN wt%

	36Ni-4Cr(H)	31Ni-5Cr(L)	26Ni-4Cr(H)	31Ni(L)	34Ni-9Co(H)
	stable	metastable	metastable	metastable	metastable
	---	high $\Delta V/V$	high $\Delta V/V$	low $\Delta V/V$	low $\Delta V/V$
Ni	36.0	30.5	26.0	30.8	34.0
Ti	3.1	2.66	3.4	2.72	3.0
Cr	3.9	5.0	3.9	---	---
Co	---	---	---	---	8.9
C	0.011	0.004	0.010	0.004	0.011
Mo	1.2	1.4	1.2	1.4	1.1
V	0.29	0.31	0.30	0.32	0.11
Al	0.22	0.23	0.23	0.20	0.23
B	0.008	0.007	0.007	0.007	0.008
N	0.0016	0.002	0.0015	0.0009	0.0012
Mn	0.18	0.07	0.19	0.10	0.17
P	0.007	0.001	0.005	0.005	0.005
S	0.004	0.003	0.004	0.002	0.004
Fe	bal.	bal.	bal.	bal.	bal.

strong materials (yield strength $> 1100\text{MPa}$), with the same temperature dependence of the yield strength in the pure austenitic phase. Also the M_s^σ temperatures for the less stable compositions was desired to come at about room temperature. The latter requirement assures that these alloys will have their highest yield strength at room temperature.

The second alloy-design objective was to have the metastable compositions with different relative volume changes accompanying the martensitic transformation. Although ferrous martensite is generally ferromagnetic, the Curie temperature of the austenite can be adjusted by compositional variation, and ferromagnetic austenites usually show the Invar effect⁽¹¹⁷⁾. As shown schematically in Figure 7, there is a sharp knee in the temperature dependence of the austenitic effective atomic volume at the Curie temperature. If a ferromagnetic austenite is transformed at temperatures well below the Curie temperature, the transformational volume expansion becomes relatively small or even null⁽¹¹⁸⁾.

Taking 31Ni(L), which is expected to be slightly ferromagnetic in the austenitic state at temperatures around room temperature⁽¹¹⁸⁾, as the basic metastable composition, the addition of Co increases the austenitic Curie temperature while Cr produces the reverse effect. In view of these considerations, 34Ni-9Co(H) was designed to obtain a highly ferromagnetic austenite at room temperature with a very low volume change attending the martensitic transformation. 26Ni-4Cr(H), on the other hand, was designed to be

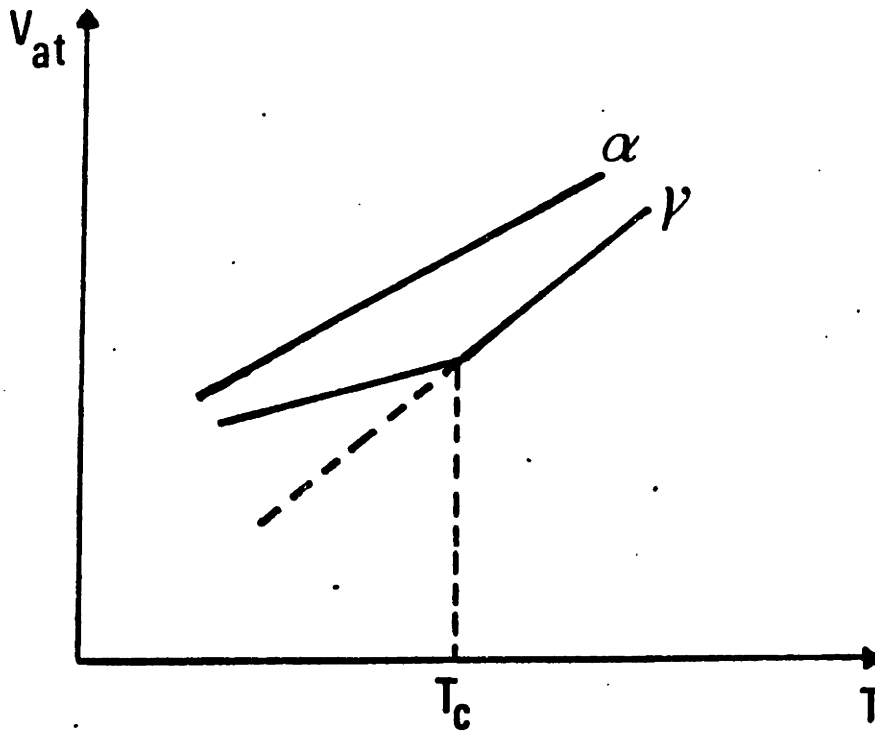


Figure 7 - Schematic temperature dependence of the effective atomic volume for martensite and austenite showing the Invar effect.

paramagnetic at room temperature with a high volume change in the transformation. In both of the above alloys, the Ni content was selected to produce compositions with comparable stability to that of 31Ni(L). Finally, the alloy 31Ni-5Cr(L), although still metastable, is much more stable than 31Ni(L), 34Ni-9Co(H) and 36Ni-4Cr(H), while 36Ni-4Cr(H) is designed to be completely stable over the range of temperatures studied in this work.

The alloys were received in ingot sizes of about 5x10x20 cm. They were homogenized at 1200°C for 24 hours under inert atmosphere, followed by hot-rolling at 1100°C down to a thickness of 1.02cm.

After the hot-rolling operation, the materials were solutionized as shown in Table II. The treatments were done on slabs of approximate size 12x10x1 cm. covered with a ceramic coating to protect against oxidation. The solutionizing treatments were chosen to produce the same grain size in all the alloys. These treatments had to be done at temperatures equal or higher than 1000°C to avoid observed cellular precipitation on the grain boundaries, a phenomenon which had been previously reported⁽¹¹⁹⁾. In all cases the grain size was of the order of 100 μm., with the difference in the treatment temperature suggesting that the presence of chromium made grain growth more difficult.

Initially an attempt was made to avoid any rolling operation, but the maximum strength obtained after aging at peak hardness was too low (yield strength \approx 1000MPa).

TABLE II : SELECTED TREATMENTS

	Solutionizing	Warm-Rolling	Aging
36Ni-4Cr(H)	1050°C/lhr	40% at 450°C	720°C/lhr
31Ni-5Cr(L)	1050°C/lhr	40% at 450°C	720°C/45min
26Ni-4Cr(H)	1050°C/lhr	40% at 450°C	720°C/2hrs
31Ni(L)	1000°C/lhr	40% at 450°C	720°C/30min
34Ni-9Co(H)	1000°C/lhr	40% at 450°C	720°C/2hrs

Furthermore, the tensile fracture at room temperature for all alloys was intergranular. In order to increase the strength of the alloys and to avoid intergranular fracture, a warm-rolling operation of 40% reduction in thickness at 450°C was introduced after the solutionizing treatment, with the material thickness being reduced to 6.35 mm.

The aging treatments shown in Table II were then selected to accomplish the design objectives. The chosen treatments did not correspond to peak hardness, but all compositions were slightly underaged. All aging treatments were performed on specimens machined to their final dimensions and quartz encapsulated under an argon atmosphere.

3.2 - Transformation Volume-Change Measurements

The transformation volume change was determined for the metastable compositions after the treatments described in Table II by measuring the difference between the effective atomic volumes of martensite and austenite. The martensitic and austenitic lattice parameters for 31Ni(L), 34Ni-9Co(H) and 26Ni-4Cr(H) as well as the austenitic lattice parameter for 31Ni-5Cr(L) were measured as a function of temperature in the range -50°C to 90°C in an X-ray diffractometer using a chromium K_{α} source ($\lambda = 2.291 \overset{\circ}{\text{A}}$) operated at 35kV and 15mA. The room-temperature martensitic lattice parameter for 31Ni-5Cr(L) was also determined. The martensitic (211) and austenitic (220) peaks were selected to give the closest reflection angles to 90° , thus minimizing experimental errors.

The dependence of the atomic volume with temperature is shown in Figure 8. Table III gives the relative transformation volume-change for the temperatures in the extremes of the range measured as well as at room temperature. From these results it is apparent that the cobalt-containing alloy does not have the expected lower transformation volume change when compared with 31Ni(L). The increase in $\Delta V/V$ for aged Fe-Ni-Ti-Co alloys as compared to the solutionized condition has been previously reported⁽¹²⁰⁾ and the origin of this effect of aging is unclear.

Although no alloy shows a large temperature variation of $\Delta V/V$, the results in Figure 8 and Table III

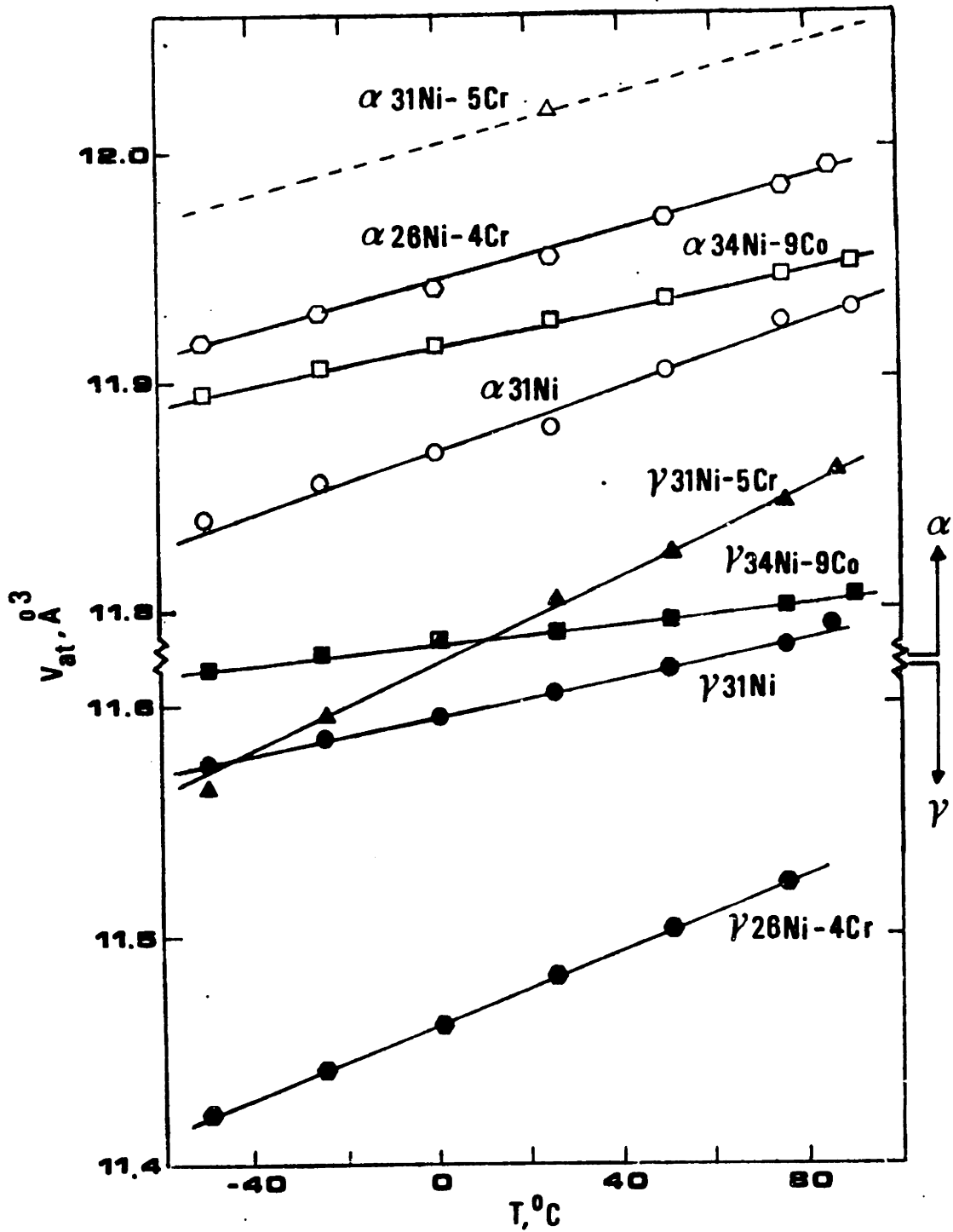


Figure 8 - Temperature dependence of the effective atomic volume of martensite and austenite for the alloys studied in this work.

TABLE III : RELATIVE TRANSFORMATIONAL VOLUME CHANGE OF
METASTABLE ALLOYS

	$\Delta v/v(\%)$		
	-50°C	25°C	90°C
34Ni-9Co(H)	2.40	2.52	2.60
31Ni(L)	2.39	2.44	2.52
26Ni-4Cr(H)	4.35	4.13	4.08
31Ni-5Cr(L)	3.77*	3.55	3.20*

* Estimated from the assumed temperature dependence of v_{at}
for martensite

indicate that ferromagnetic 34Ni-9Co(H) and 31Ni(L) show a slight decrease in $\Delta V/V$ with decreasing temperature, while the opposite applies to paramagnetic 26Ni-4Cr(H). Also, the temperature dependence of the austenitic effective atomic volume for paramagnetic 26Ni-4Cr(H) is much steeper than for the ferromagnetic 34Ni-9Co(H) and 31Ni(L), consistent with the usual Invar effects associated with the austenite magnetic properties. The steep atomic volume temperature dependence of 31Ni-5Cr(L) suggests that its austenite is also paramagnetic and probably has a slightly increasing $\Delta V/V$ at low temperatures. Based on the similarities between 31Ni-5Cr(L) and 26Ni-4Cr(H), the slope of the temperature dependence for the effective atomic volume of martensitic 31Ni-5Cr(L) was taken equal to that measured for 26Ni-4Cr(H).

From the results shown in Figure 8 and Table III, 26Ni-4Cr(H) and 31Ni-5Cr(L) have relatively higher $\Delta V/V$ as compared to 34Ni-9Co(H) and 31Ni(L). Based on this, 26Ni-4Cr(H) and 31Ni-5Cr(L) may be referred to as the high transformational volume-change alloys (HV) as opposed to the low transformational volume-change alloys (LV), 34Ni-9Co(H) and 31Ni(L).

3.3 - Tensile Tests

Tensile tests were performed on all compositions treated as listed in Table II in the temperature range -196°C to 225°C . The tests were conducted on an Instron machine model TTDL1362 at a crosshead rate of 8.47×10^{-3} mm/s. At temperatures above room temperature the tests were performed in a silicone oil bath, while at temperatures below room temperature alcohol refrigerated by liquid nitrogen was used. At -196°C liquid nitrogen was employed.

The specimen dimensions given in Figure 9 comply with the TR-6 specifications⁽¹²¹⁾ for round tensile specimens. The loading axis of the specimens was aligned with the rolling direction of the plates.

From the load-displacement curves obtained directly from the machine chart recorder, the values of yield strength (σ_y), plastic uniform elongation (ϵ_{pu}), and true-stress, true-plastic-strain curves were calculated. Values of true strain to failure in the necked region (ϵ_f^n) were also determined for each specimen.

After fracture, half of each specimen was used for fractographic analysis carried out on an AMR-SEM under 25kV. The other half was longitudinally ground, polished and etched for optical metallographic examination. The etchant used for revealing the martensite was 100 ml H_2O - 20 ml HCl - 0.12g $\text{Na}_2\text{S}_2\text{O}_5$ applied for 5 to 10 seconds. In some cases a solution of 80 ml H_2O_2 - 15 ml H_2O - 5 ml HF was used for

A	B	C	D	E	F
57.14	12.70	4.06	0.125R	25.40	0.32

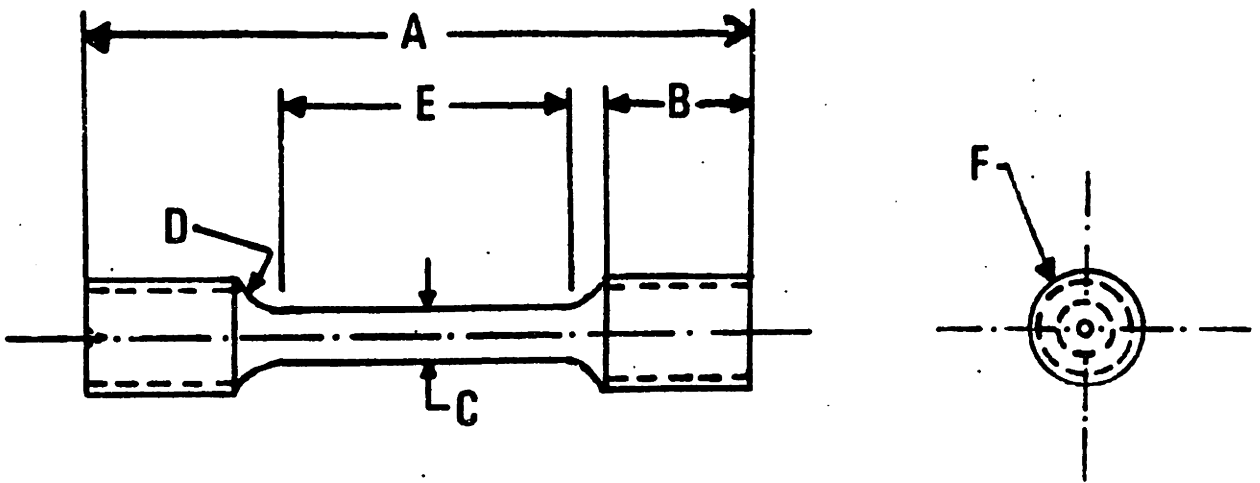


Figure 9 - Tensile specimens. Dimensions in mm.

5 to 10 seconds prior to the metabisulfite etchant for revealing the austenitic grain boundaries. The optical metallography was conducted with an A.O. Ultrastar microscope.

3.4 - Fracture Toughness Tests

Fracture toughness tests on three-point bend specimens, using the J-integral method, were performed over the temperature range of -196°C to 300°C . The three-point bend specimen dimensions are shown in Figure 10. The specimens were cut in the L-W direction, with their length aligned in the rolling direction and the crack propagating in the plate width direction.

The samples were pre-cracked under equal conditions on a Physmet FCM-300B pre-cracking machine up to a remaining uncracked ligament of about 5.0 mm. This gives a ratio of initial crack-length to specimen width, $a_0/W \cong 0.56$, which lies within the recommended range of a_0/W values (54,60). At least three samples were tested for each condition, with the test stopped at different values of crack extension (Δa). The maximum crack extension in all cases was kept below 2.0mm.

In the temperature range of -196°C to 225°C , the tests were conducted on a Physmet SB-750C three-point bending machine with a crosshead rate of 5.29×10^{-3} mm/s. These tests were conducted in the same environments as described for the tensile tests. The tests at 300°C were performed in an air oven with an Instron machine model TTDL1362 at a crosshead rate of 4.23×10^{-3} mm/s. The fixtures used for the tests at 300°C were the same used for all other temperatures to assure the same span distance. No detectable difference in stiffness between the two machines was observed.

A	B	C	D	E
53.34	5.08	1.14	11.43	5.715

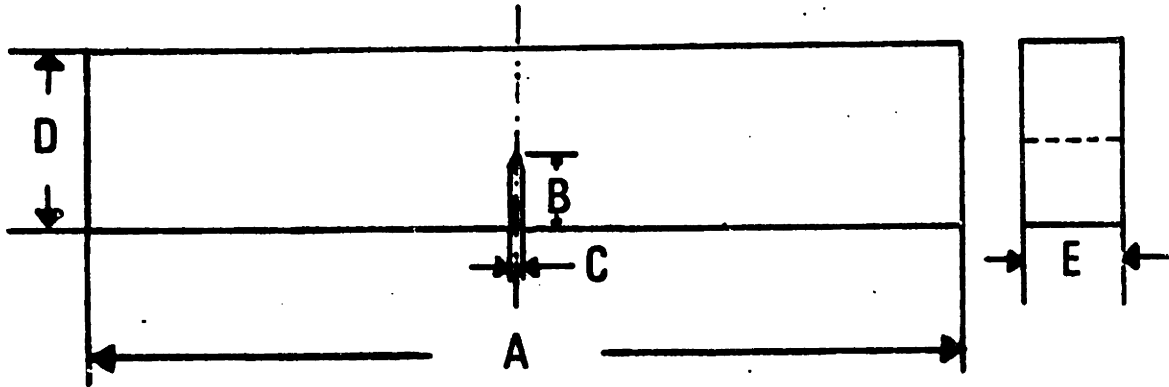


Figure 10 - Fracture toughness specimens. Dimensions in mm.

In addition, three 31Ni-5Cr(L) specimens aged at 720°C for 64 hours (overaged) were tested at -25°C. One 20% side grooved 31Ni-5Cr(L) specimen was tested at -75°C. The grooves had an opening angle of 90° and penetrated 10% of the thickness from each side of the usual specimen. The tests of overaged and side-grooved specimens are discussed in the Appendix.

The J-integral values were calculated using the formula developed by Rice et al.⁽⁵⁷⁾ for bending specimens:

$$J = \frac{2A}{3b} \quad [22]$$

where A is the area under the load-displacement curve, B is the specimen thickness and b is the initial uncracked ligament.

After unloading, the specimens were cut in two half-thickness parts with a 0.3mm thick diamond saw in a low-speed Isomet cutting machine. One of the two halves was used for measuring the crack-length displacement by heat tinting, while the other half was reserved either for optical metallography of the crack-tip region or for fractographic analysis. At each temperature for all alloys, the metallography was usually done on the specimen loaded to the smallest crack extension, or, in other words, to J values closest to J_{IC} , while the fractography was done on specimens loaded to larger crack extensions.

The heat tinting was done at 300°C for 30 min. and the crack extension (Δa) was measured as the largest Δa ahead of the fatigue pre-crack; in all cases this occurred at the center of the specimens. Curves of J versus Δa were constructed, and from them J_{Ic} and $dJ/d\Delta a$ values were obtained.

For optical metallography, the crack was first impregnated with resin under vacuum to avoid further opening during the grinding, polishing and etching procedures. The metallographic technique as well as the fractographic analysis followed the same procedure as for the tensile specimens.

CHAPTER IV : EXPERIMENTAL RESULTS

4.1 - Yield Strength and Transformation Behavior

Figure 11 shows the temperature dependence of the yield strength for all compositions. The data suggest that 31Ni(L) has an M_S temperature around -160°C while 34Ni-9Co(H) and all other alloys have $M_S < -196^{\circ}\text{C}$. This has been confirmed by metallographic examination of 31Ni(L) and 34Ni-9Co(H) cooled to -196°C for a short period of time; while plate martensite was formed in 31Ni(L), no transformation was observed in 34Ni-9Co(H). Magnetic tests confirmed that no transformation was present in the other three alloys after cooling to -196°C .

Figure 11 suggests uniaxial tension M_S^{σ} temperatures ($M_S^{\sigma}(u)$) for 31Ni(L) and 34Ni-9Co(H) respectively equal to -20°C and 30°C . The value of $M_S^{\sigma}(u)$ for 34Ni-9Co(H) has been confirmed by the construction of the same σ_y versus T curve using the one-specimen technique developed by Bolling and Richman⁽⁴⁾. However, this same technique indicated $M_S^{\sigma}(u) \cong 20^{\circ}\text{C}$ for 31Ni(L). Furthermore, a careful examination of Figure 11 suggest a slight drop in yield strength for 31Ni(L) tested at $T < 25^{\circ}\text{C}$ (dashed line). These observations indicate uncertainty in the actual $M_S^{\sigma}(u)$ for 31Ni(L), which appears to be in the range -20°C to 25°C .

The uniaxial tension M_S^{σ} temperatures for 31 Ni(L) and 34Ni-9Co(H) being in the range of -20°C to 30°C fits

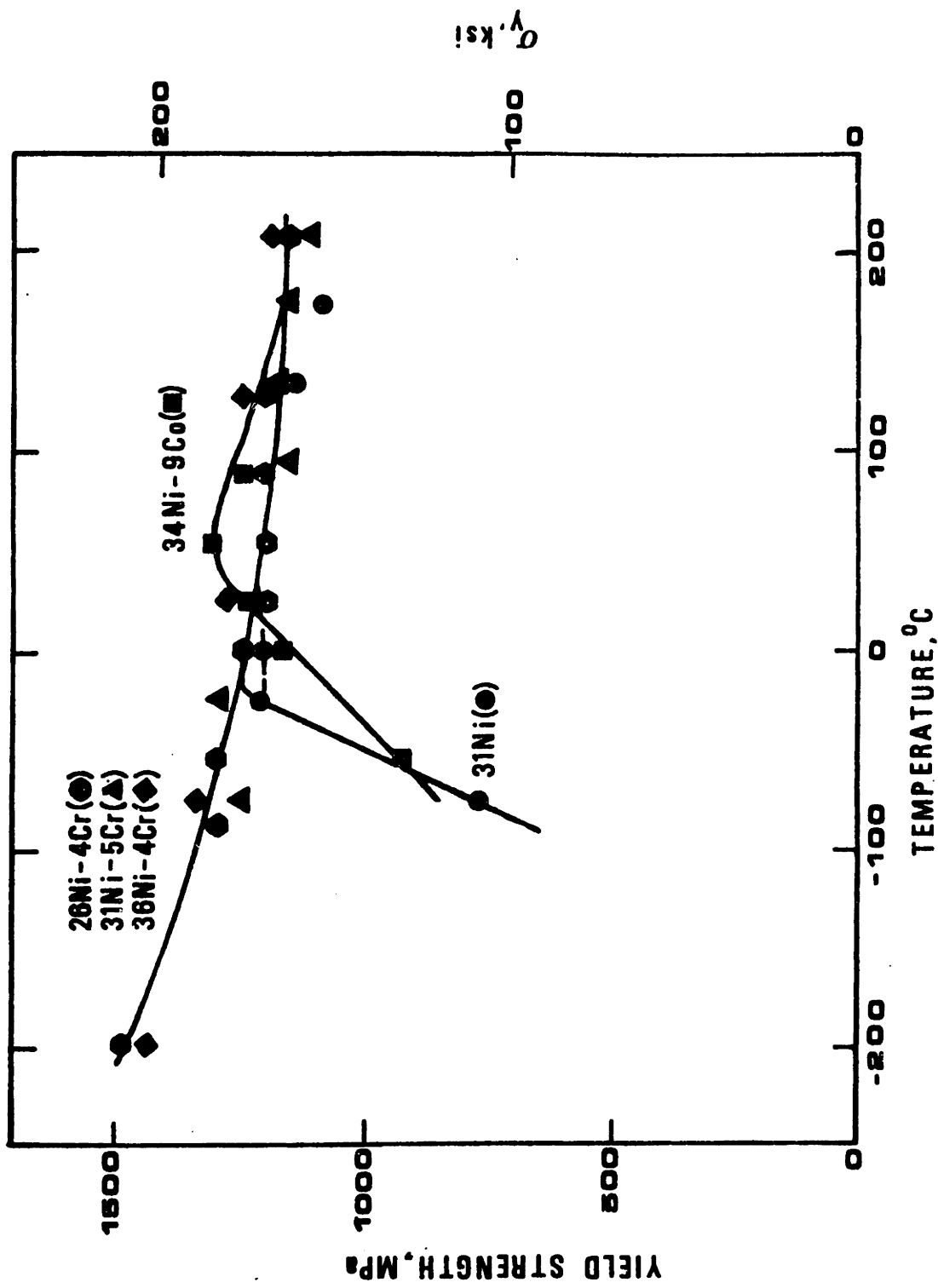


Figure 11 - Yield strength versus temperature. The dashed line indicates possible drop in σ_y for 31Ni(L).

reasonably well the design objective of having the strength level of the less stable alloys as high as possible near room temperature. Also, whenever yielding is controlled by slip in the austenite, the temperature dependence of the yield strength is the same for all alloys. The elevation in yield strength observed for 34Ni-9Co(H) at temperatures a little higher than M_S^σ temperature has been previously reported for other metastable austenitic alloys⁽¹²¹⁾ and has been proposed to be a consequence of the so-called pre-transformation strengthening phenomenon.

Although all the chromium-containing alloys apparently showed no obvious uniaxial-tension M_S^σ temperature ($M_S^\sigma(u)$) down to -196°C , an $M_S^\sigma(u)$ temperature of -120°C is estimated for 26Ni-4Cr(H). This choice is based on the results for uniform elongation and its rationale will be discussed later. A significant drop in the yield strength may not be observed at -196°C due to a high tendency for isothermal transformation kinetics in this alloy. Furthermore, the metallographic technique for M_S^σ estimation described next suggests a change in the martensite predominant morphology in the region outside the neck for 26Ni-4Cr(H) in the interval -196°C to -90°C . Table IV lists M_S and uniaxial tension M_S^σ temperature ($M_S^\sigma(u)$) for all compositions.

Portions of the text
on the following page(s)
are not legible in the
original.

TABLE IV : M_s , M_s^u , AND M_d FOR UNIAXIAL TENSION, NECKED REGION, AND CRACK-TIP

	Uniaxial Tension		Necking		Crack-Tip		
	M_s ($^{\circ}$ C)	$M_s^u(u)$ ($^{\circ}$ C)	$M_d(u)$ ($^{\circ}$ C)	$M_s^u(n)$ ($^{\circ}$ C)	$M_d(n)$ ($^{\circ}$ C)	$M_s^u(ct)$ ($^{\circ}$ C)	$M_d(ct)$ ($^{\circ}$ C)
36Ni-4Cr(H)	<-196	<-196	<-196	<-196	<-196	<-196	<-196
31Ni-5Cr(H)	<-196	<-196	-196 < M_d < -75	<-196	25 < M_d < 95	-196 < M_s^u < -75	95 < M_d < 135
26Ni-4Cr(H)	<-196	<-120	-55 < M_d < 0	\approx 0	> 220	\approx 55	220 < M_d < 300
31Ni(H)	\approx -160	-20 < M_s^u < 30	60 < M_d < 95	\approx 60	175 < M_d < 220	90 < M_s^u < 135	175 < M_d < 225
34Ni-9Co(H)	<-196	\approx 30	90 < M_d < 130	\approx 90	> 220	\approx 130	220 < M_d < 300

Equation 4 predicts that the M_S^σ temperature is stress-state dependent. The M_S^σ temperature for the necked region and that ahead of the crack-tip can be experimentally estimated by metallographically studying the changes in martensite morphology. The plate morphology is predominant for the stress-assisted martensite while strain-induced martensite shows predominantly lath morphology. Table IV lists the M_S^σ temperatures estimated for the necked region ($M_S^\sigma(n)$) and crack-tip ($M_S^\sigma(ct)$). Whenever a temperature interval is listed, this means that at the lower temperature, plate martensite is clearly predominant while at the higher temperature, lath martensite is the predominant morphology.

Table IV also lists the M_d temperatures for each stress-state ($M_d(u)$ for uniaxial tension, $M_d(n)$ for the necked region and $M_d(ct)$ for the crack-tip). The M_d temperatures have been determined by metallography. In this work M_d is defined as the highest temperature where martensite can be found at 1000X under an optical microscope. Whenever a temperature interval is listed for M_d , this means that at the lower temperature martensite has been detected by optical metallography while at the higher temperature no transformation is observed.

Whenever M_S^σ or M_d is presented as a temperature interval, for purpose of calculations or graphic display the highest temperature in the interval is considered. In other

words, M_s^* and M_d temperatures shown in graphs or used in calculations are either the actually determined value or an upper-bound value. In the upper-bound case, horizontal error bars are displayed to account for the uncertainty in the temperature determination.

A detailed discussion of transformation behavior is given in section 5.1.

4.2 - Mechanical Behavior

4.2.1 - Tensile Tests

Tables V to IX show the results obtained for all alloys studied. Figure 11 shows the temperature dependence of the yield strength (σ_y) for all compositions, as discussed in the previous section. Figure 12 illustrates the temperature dependence of the plastic uniform elongation (ϵ_{pu}) for all compositions. Figures 13 and 14 show the true fracture strain in the necked region (ϵ_f^n) for the lower- and higher-carbon alloys, respectively. In all these plots the relevant M_d temperatures are indicated.

Uniform Ductility

The temperature dependence of the true plastic uniform elongation (ϵ_{pu}) depicted in Figure 12 clearly indicates the existence of two levels of ϵ_{pu} values for the metastable austenitic alloys studied here. By decreasing the test temperature from 225°C, the values of ϵ_{pu} increase smoothly until the $M_d(u)$ temperature is reached. At temperatures below $M_d(u)$, initially a small drop in uniform elongation occurs, followed by a sharp increase of nearly one order of magnitude. With further decrease in temperature, although the uniform elongation remains fairly high, a progressive drop is observed. These features are apparent in the response of 31Ni(L), 34Ni-9Co(H) and 26Ni-4Cr(H). No sharp variation in ϵ_{pu} is found for 31Ni-5Cr(L) and 36Ni-4Cr(H) because no martensitic transformation takes place before necking in these alloys over the temperature range

TABLE V : TENSILE PROPERTIES OF 36Ni-4Cr(H)

T(°C)	σ_y (MPa)	ϵ_{pu}	ϵ_f^n
-196	1445	0.1093	0.4165
-75	1339	0.0600	0.3581
25	1271	0.0388	0.3561
130	1253	0.0187	0.2430
220	1179	0.0139	0.1910

TABLE VI : TENSILE PROPERTIES OF 31Ni-5Cr(L)

T(°C)	σ_y (MPa)	ϵ_{pu}	ϵ_f^n
-196	1497	0.1128	0.9768
-75	1247	0.0649	0.7497
-25	1289	0.0482	0.6870
25	1219	0.0496	0.6070
95	1149	0.0314	0.6070
135	1178	0.0310	0.4179
175	1138	0.0208	0.6184
220	1126	0.0237	0.6832

TABLE VII : TENSILE PROPERTIES OF 26Ni-4Cr(H)

T(°C)	σ_y (MPa)	ϵ_{pu}	ϵ_f^n
-196	1456	0.1738	0.0758
-90	1314	0.3206	0.2540
-55	1304	0.0457	0.3436
0	1236	0.0628	0.8178
25	1201	0.0530	1.0533
55	1185	0.0401	0.6731
90	1198	0.0342	0.7476
130	1219	0.0302	0.5423
220	1153	0.0235	0.2951

TABLE VIII : TENSILE PROPERTIES OF 31Ni(L)

T(°C)	σ_y (MPa)	ϵ_{pu}	ϵ_f^n
-75	764	0.1547	0.2536
-25	1208	0.2186	0.6806
0	1200	0.2263	0.8278
25	1219	0.2465	0.8926
60	1181	0.0400	0.9742
95	1146	0.0447	1.1410
135	1144	0.0366	0.6097
175	1079	0.0229	0.6749
220	1118	0.0229	0.7500

TABLE IX : TENSILE PROPERTIES OF 34Ni-9Co(H)

T(°C)	σ_y (MPa)	ϵ_{pu}	ϵ_f^n
-55	904	0.1547	0.1889
0	1182	0.1749	0.1797
25	1245	0.1912	0.3549
55	1300	0.1813	0.7369
90	1238	0.0193	0.8167
130	1236	0.0176	0.6073
220	1132	0.0201	0.2987

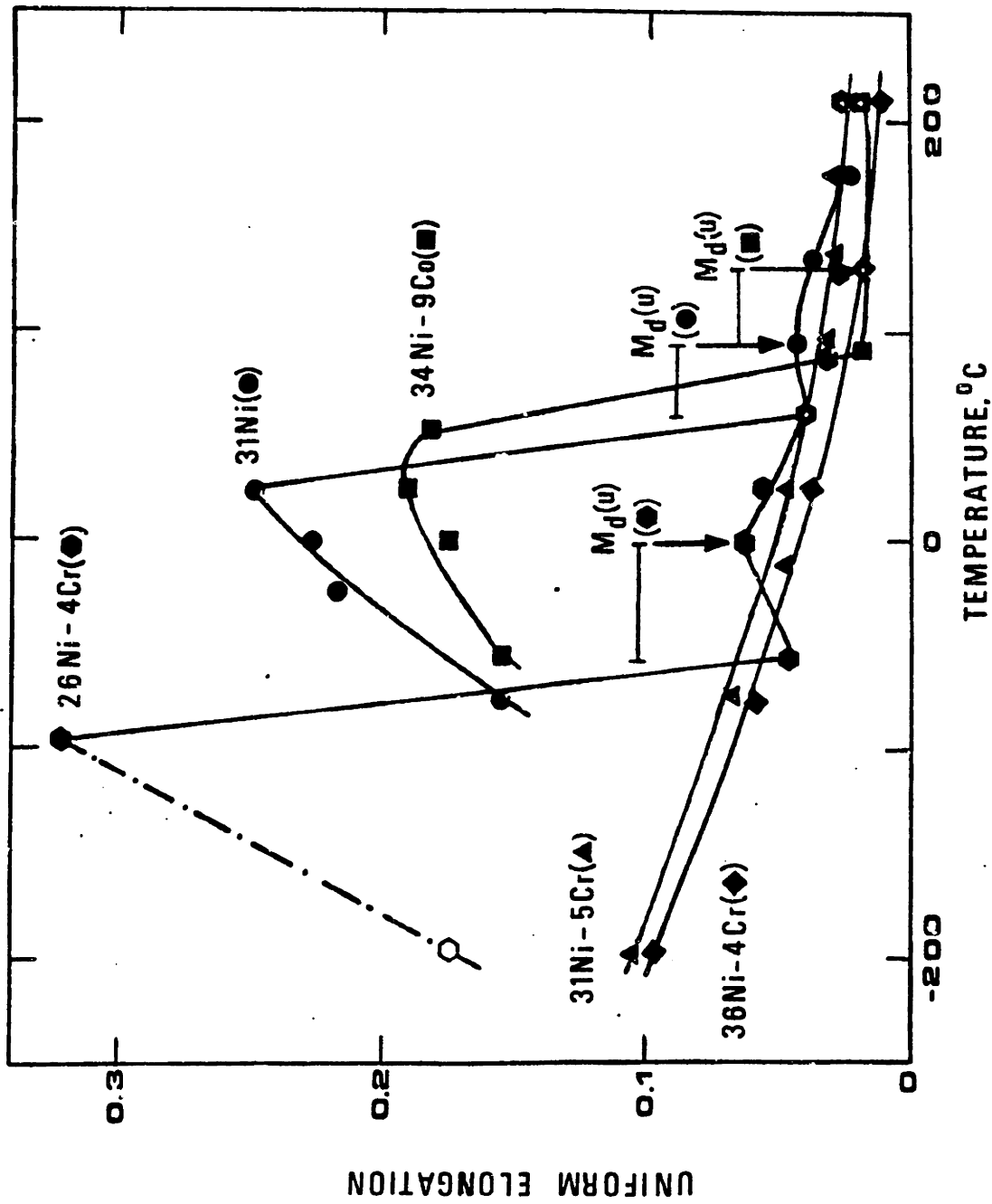


Figure 12 - Plastic uniform elongation versus temperature. The dashed line and open point indicate premature failure. The horizontal error bars indicate the uncertainty in M_d temperatures.

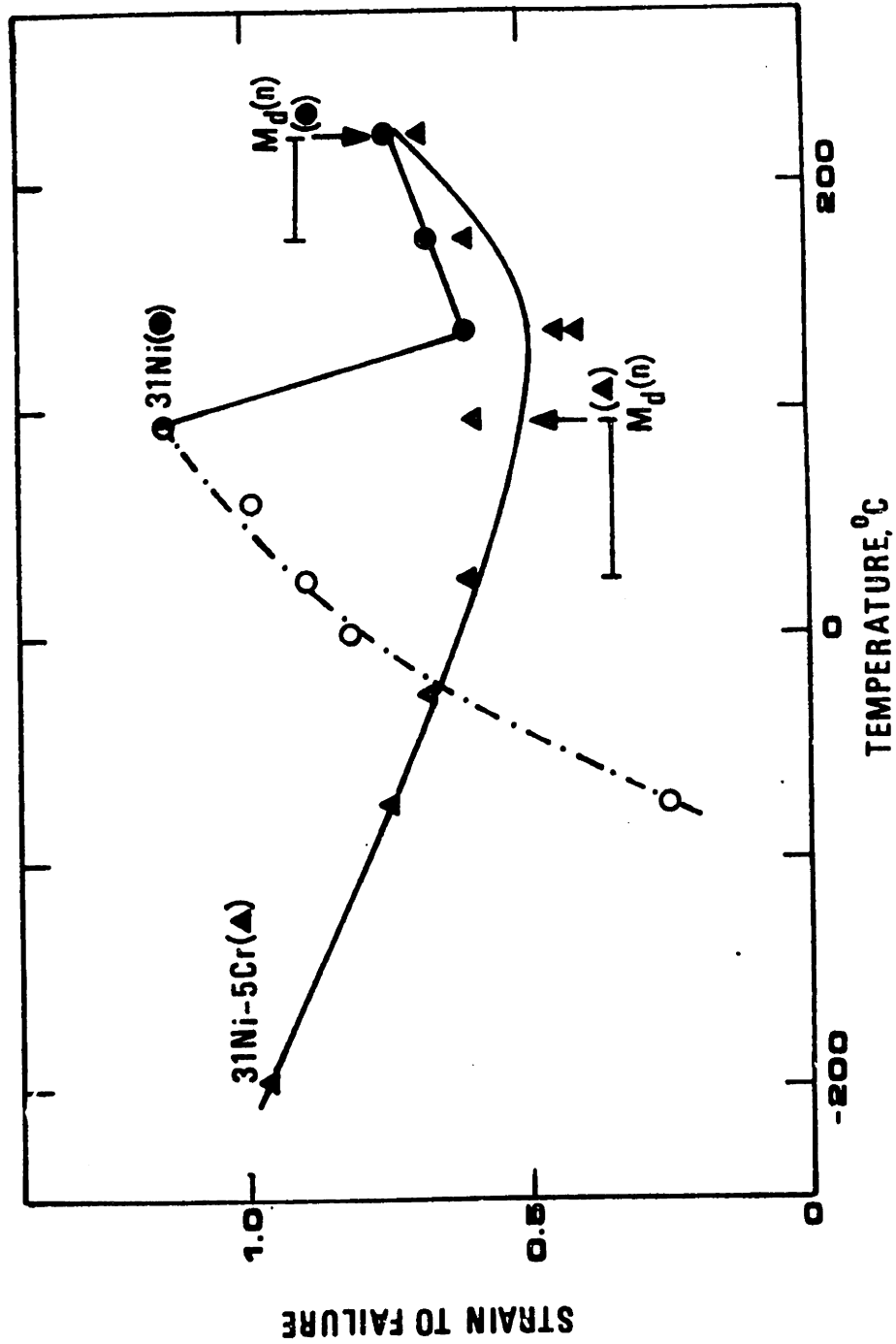


Figure 13 - Strain to failure versus temperature for the lower-carbon alloys. The dashed lines and open points indicate premature failure. The horizontal error bars indicate the uncertainty in M_d temperatures.

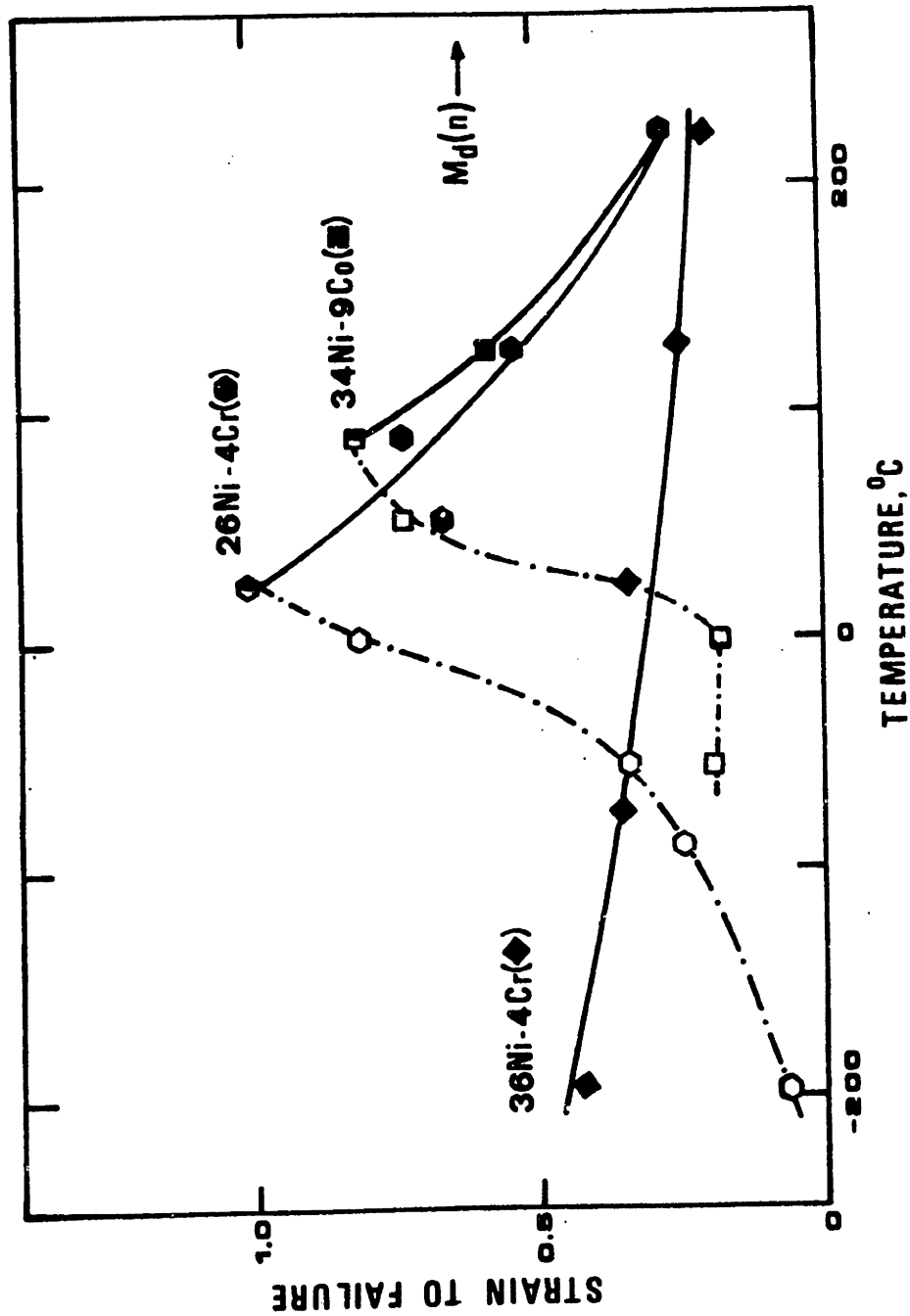


Figure 14 - Strain to fracture versus temperature for the higher-carbon alloys. The dashed lines and open points indicate premature failure.

studied.

Only in one case did fracture occur before necking. This happened for 26Ni-4Cr(H) tested at -196°C . The uniform elongation in this case is equal to the fracture strain.

The behavior of the uniform elongation at temperatures lower than $M_d(u)$ is a consequence of mechanically-induced martensitic transformation. While at temperatures higher than $M_d(u)$ no transformation occurs before necking, in the temperature where the uniform elongation is maximum, substantial transformation is present outside the necked region of tensile specimens. For instance, Figure 15 shows this region in 31Ni(L) tested at 25°C . The drop at lower temperatures, where the alloys are progressively less stable relative to the martensitic transformation, suggests that an optimum stability condition is required for obtaining maximum uniform elongation.

The drop in ϵ_{pu} at temperatures just below $M_d(u)$ is apparently related to the first mechanically-induced martensite formed before necking. Figure 16 shows small patches of transformation present throughout the uniformly strained region of 26Ni-4Cr(H) tested at -55°C , corresponding to the local minimum in ϵ_{pu} .

A more detailed analysis of the influence of mechanically-induced martensitic transformation on the uniform elongation will be presented in the next chapter.

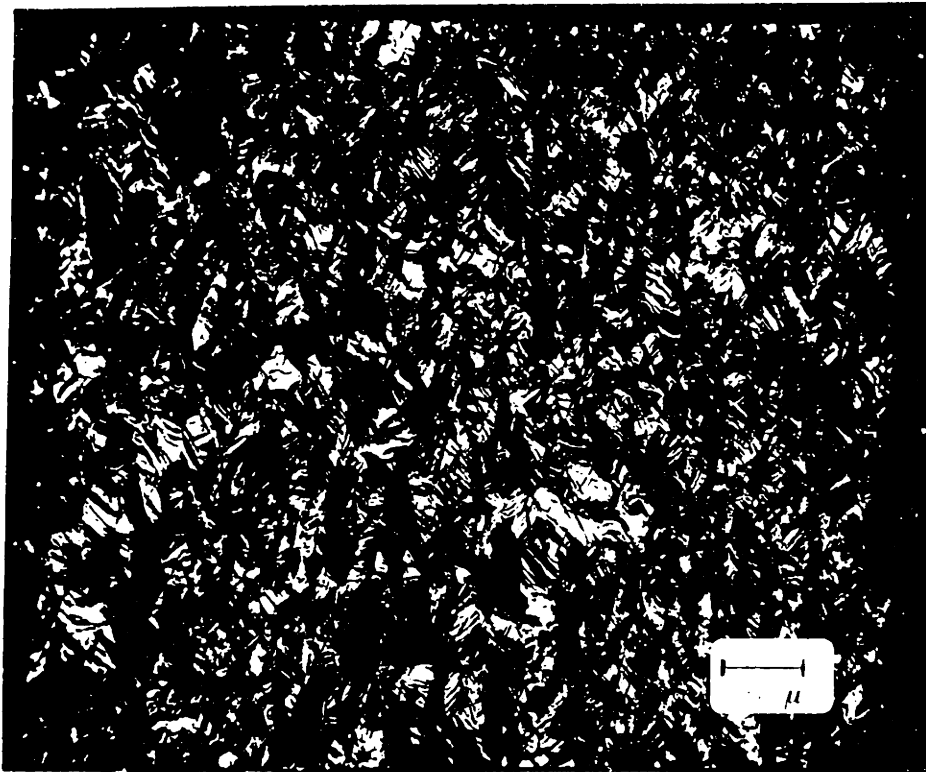


Figure 15 - Optical micrograph of the region outside necking of 31Ni(L) tensile tested at 25°C.

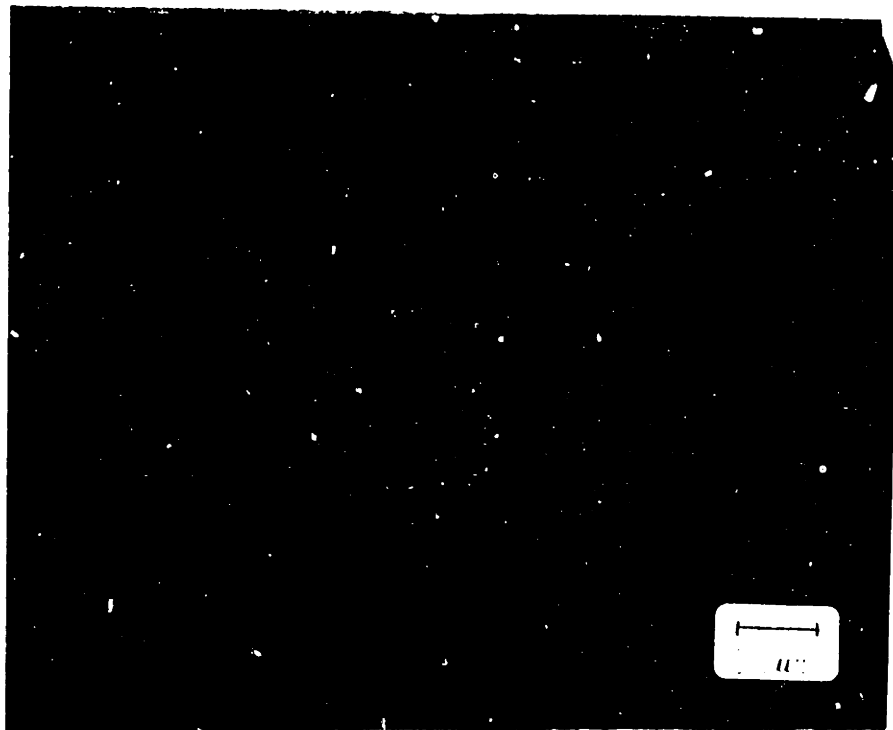
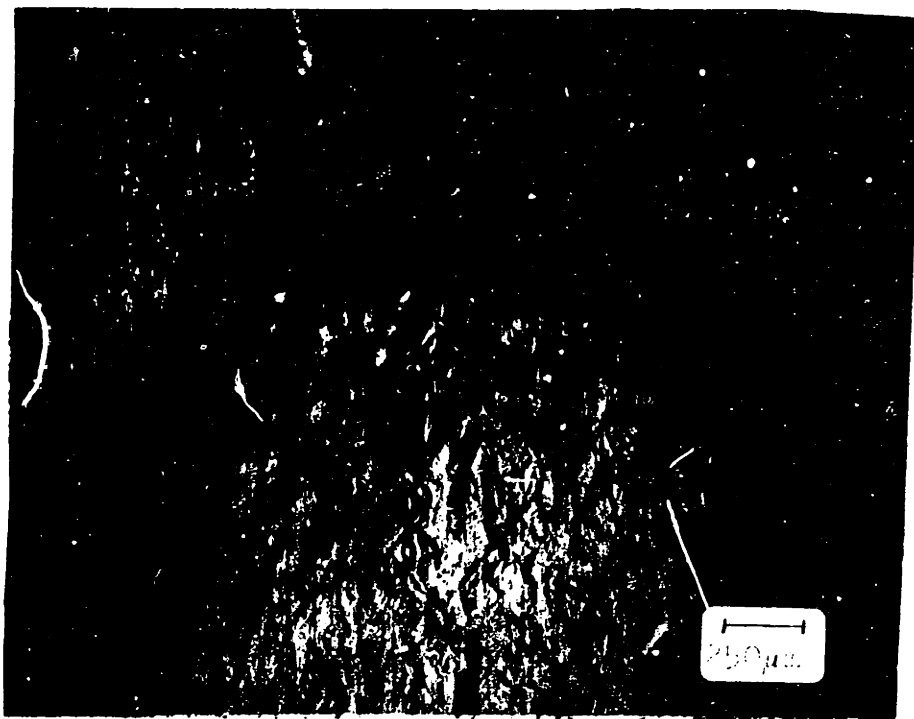


Figure 16 - Optical micrograph of the region outside necking of 26Ni-4Cr(H) tensile tested at -55°C.

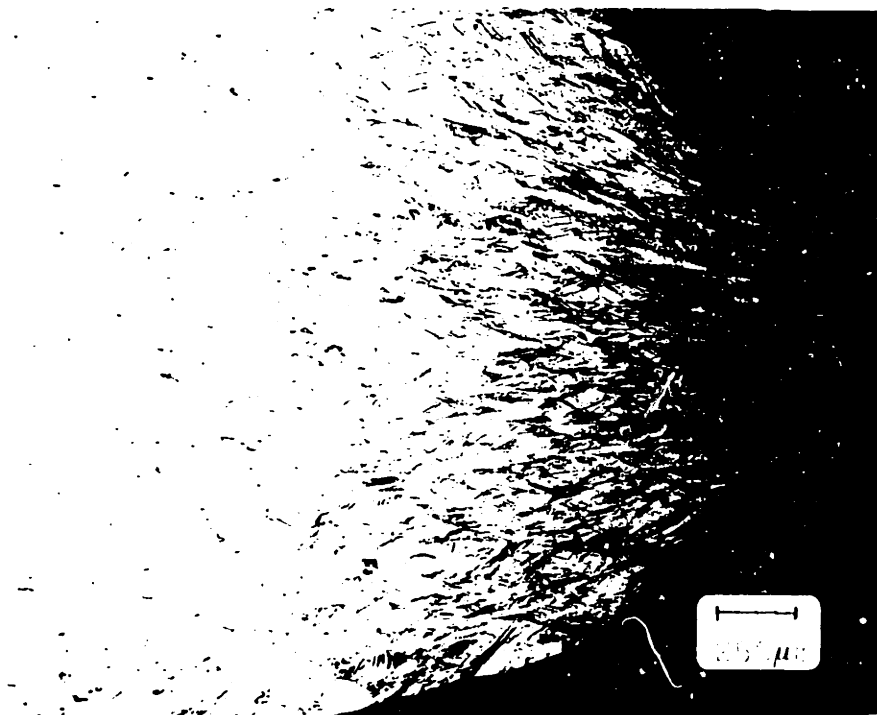
Strain to Failure in the Neck

Despite the striking difference in the overall level of ϵ_f^n at temperatures above $M_d(n)$ between the lower- and higher-carbon alloys, Figure 13 and 14 indicate some common features between the temperature dependence of ϵ_f^n and that observed for uniform elongation. Peaks in ϵ_f^n are present for 31Ni(L), 34Ni-9Co(H) and 26Ni-4Cr(H). These peaks are again a consequence of mechanically-induced martensitic transformation, now taking place at the larger strains present after necking. As Figure 17 suggests, there is apparently an optimum stability condition for highest enhancement in ϵ_f^n . For instance, in 34Ni-9Co tested at 130°C (Figure 17a), the relatively small amount of transformation occurring after necking is not sufficient to give the highest possible enhancement in ϵ_f^n . In the same alloy tested at 55°C (Figure 17c), a large amount of transformation occurs before necking and again the transformation after necking is small compared to that observed at the temperature giving the highest ϵ_f^n , $T=90^\circ\text{C}$, shown in Figure 17b. At this temperature nearly all transformation occurred after necking.

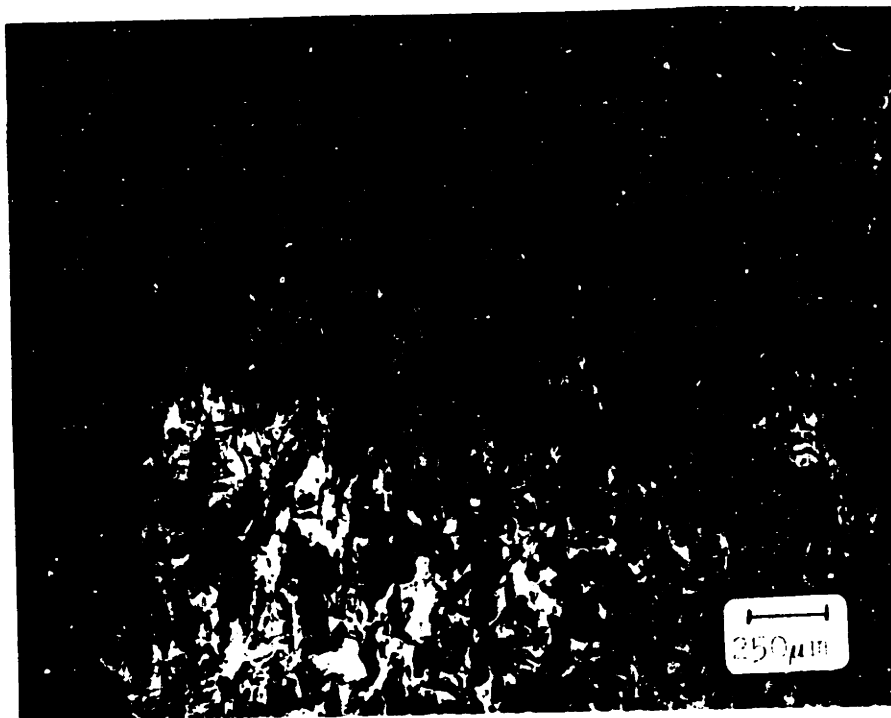
The measured values of ϵ_f^n for 31Ni-5Cr(L) suggests a reversed temperature dependence of ϵ_f^n for the lower-carbon austenite at $T \gg 135^\circ\text{C}$ as compared to the behavior of the higher-carbon austenite. Taking into account this reversed temperature dependence, the apparent drop in ϵ_f^n for 31Ni(L) tested at 135°C actually represents a significant increment



(a)



(b)



(c)

Figure 17 - Optical micrograph of the necked region of $^{34}\text{Ni}-9\text{Co}(\text{H})$ tensile tested at: (a) 130°C , (b) 90°C and (c) 55°C .

in these parameters as compared to the values for the non-transformed austenite as given by 31Ni-5Cr(L).

A more detailed analysis of the influence of the mechanically-induced martensitic transformation on the strain to failure will be presented in the next chapter.

Tensile Fracture

Whenever little or no martensite was present in the necked region, all the alloys failed by shearing on a plane about 45° to both the direction of load application (rolling direction) and the normal to the rolling plane. A typical picture of the macroscopic failure mode is shown in Figure 18. The failure on a microscopic scale occurred by void nucleation, growth and coalescence.

Although in some instances the voids were clearly nucleated by cracking of elongated particles as shown in Figure 19, in most cases the voids were evidently formed by decohesion of particle-matrix interfaces around more equiaxed particles, Figure 20. In all cases, the particles which formed voids varied in size approximately from 0.2 to 1 μm . These dimensions are much larger than those of the small γ' particles precipitated during aging and responsible for the strengthening of these alloys. The γ' particles (Ni_3Ti and/or $\text{Ni}_3(\text{Ti},\text{Al})$) have sizes in the range 50 to 100 \AA ⁰⁽¹²³⁾. X-ray dispersive analysis in the JEM indicated that the void-forming particles were highly enriched in Ti but not in Ni. This suggests that these particles were probably Ti-nitrides or Ti-carbides formed during solidification.



Figure 18 - Low-magnification view of the shear-instability tensile fracture.

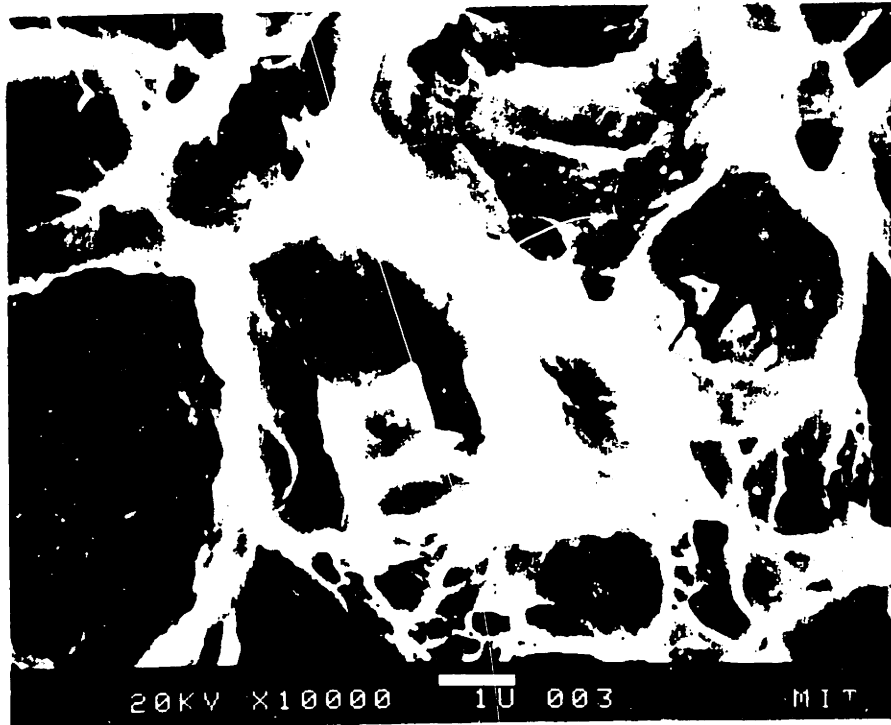


Figure 19 - High-magnification view of void-forming cracked particles in 31Ni-50Cr(1).

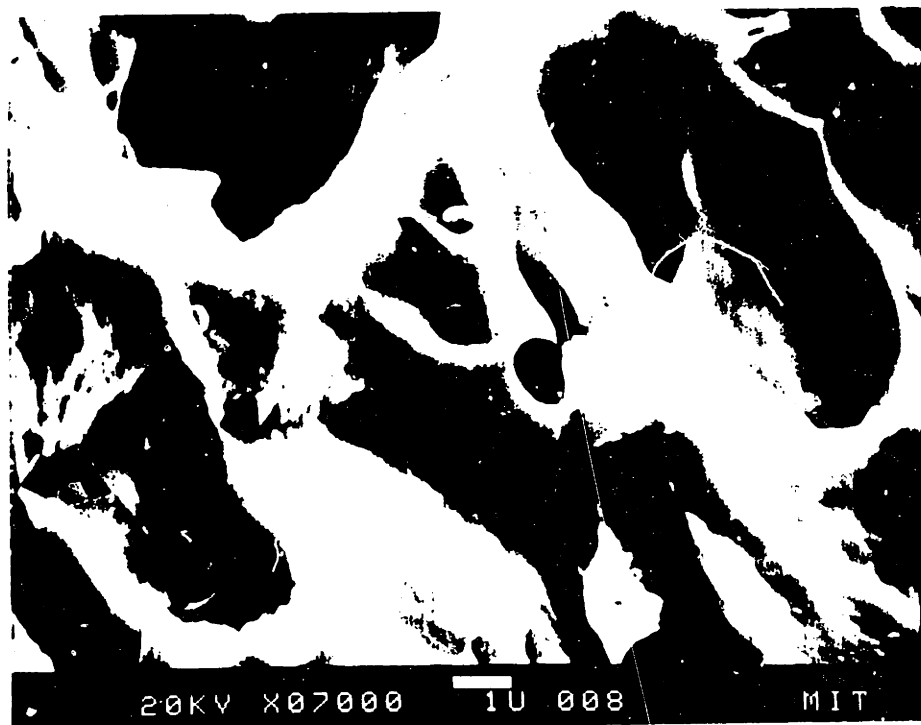


Figure 20 - High-magnification view of equiaxed void-forming particles in 31Ni-50Cr(1)

In contrast to the higher-temperature macroscopic shear-failure mode, at lower temperatures when the fracture takes place in a material that is essentially 100% martensitic, a typical cup-and-cone fracture is observed. Figures 21 and 22 show the metallography of the necked region and the low-magnification fractography of 31Ni(L) tested at 25°C. Although even at these lower temperatures the predominant microscopic failure mode was by void nucleation, growth and coalescence, cleavage and intergranular fractures were present in some instances. Figure 23 shows some intergranular fracture in 26Ni-4Cr(H) tested at -55°C. The same tendency for intergranular fracture was observed in 34Ni-9Co(H) tested at low temperatures. The 31Ni(L) alloy, on the other hand, showed some cleavage. The cleavage, intergranular fracture, and flat ductile mode of failure apparently contributed to the decrease in ϵ_f^n observed at low temperatures.

4.2.2 - Fracture Toughness Tests

From the J versus Δa curves shown in the Appendix, the J_{IC} and $dJ/d\Delta a$ values listed in Tables X to XIV were obtained. From these results, Figures 24 to 27 have been constructed to show the temperature dependence of J_{IC} and $dJ/d\Delta a$ for the lower- and higher-carbon alloys. By comparing the overall levels of J_{IC} in Figures 24 and 25 as well as the levels of $dJ/d\Delta a$ in Figures 26 and 27 at temperatures higher than $V_d(ct)$, the higher intrinsic toughness of the lower-carbon alloys is again evident.



Figure 21 - Optical micrograph of the necked region of 31Ni(L) tested at 25°C.

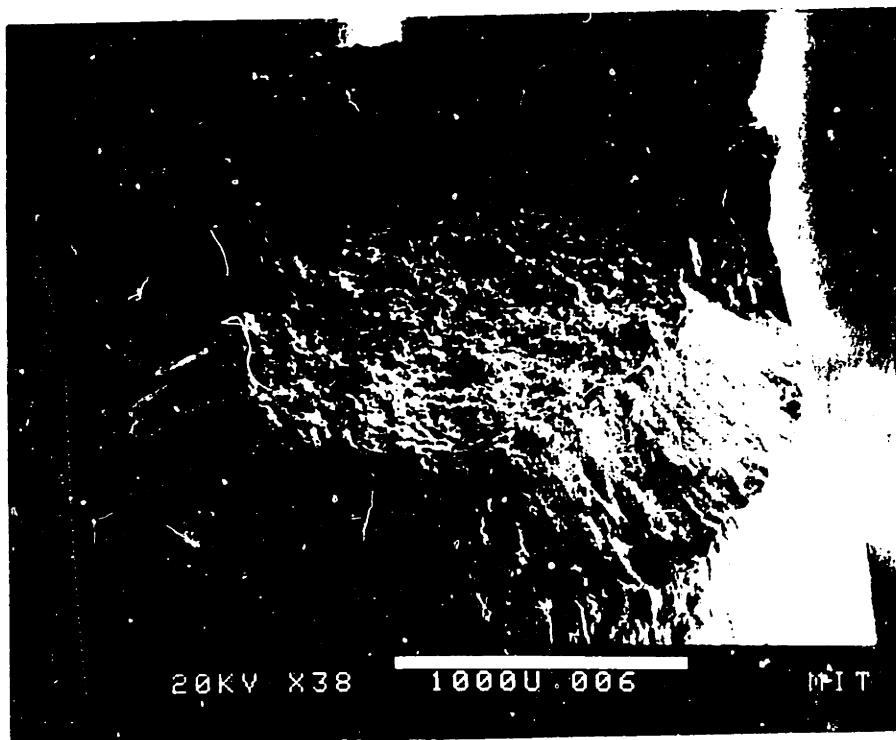


Figure 22 - SEM fractograph of 31Ni(L) tensile tested at 25°C showing a typical cup-and-cone fracture.



Figure 23 - SEM fractograph of 26Ni-4Cr(H) tensile tested at -55°C showing some intergranular fracture.

TABLE X : FRACTURE PROPERTIES OF 36Ni-4Cr(H)

T(°C)	J _{IC} (kJ/m ²)	dJ/dΔa (MPa)
-196	178.5	23.47
-75	139.3	45.17
25	117.8	33.42
130	95.6	17.84
220	108.4	27.74

TABLE XI : FRACTURE PROPERTIES OF 31Ni-5Cr(L)

T(°C)	J _{IC} (kJ/m ²)	dJ/dΔa (MPa)
-196	139.6	153.48
-25	248.7	126.87
25	206.4	109.25
95	128.1	112.58
135	153.4	36.22
220	158.7	80.42

TABLE XII : FRACTURE PROPERTIES OF 26Ni-4Cr(H)

T(°C)	J _{IC} (kJ/m ²)	dJ/dΔa (MPa)
-55	142.0	113.72
25	187.6	126.25
55	156.2	139.88
90	142.9	131.89
130	123.8	68.93
220	105.7	39.72
300	116.7	1.95

TABLE XIII : FRACTURE PROPERTIES OF 31Ni(L)

T(°C)	J _{IC} (kJ/m ²)	dJ/dΔa (MPa)
-75	64.4	15.67
25	108.4	27.34
95	170.5	213.57
135	205.6	116.17
175	116.8	88.90
220	148.1	81.77
300	142.5	19.63

TABLE XIV : FRACTURE PROPERTIES OF 34Ni-9Co(H)

T(°C)	J _{IC} (kJ/m ²)	dJ/dΔa (MPa)
-55	139.3	42.98
25	131.5	64.71
55	98.5	75.16
90	106.0	99.39
130	117.5	76.64
220	101.0	43.20

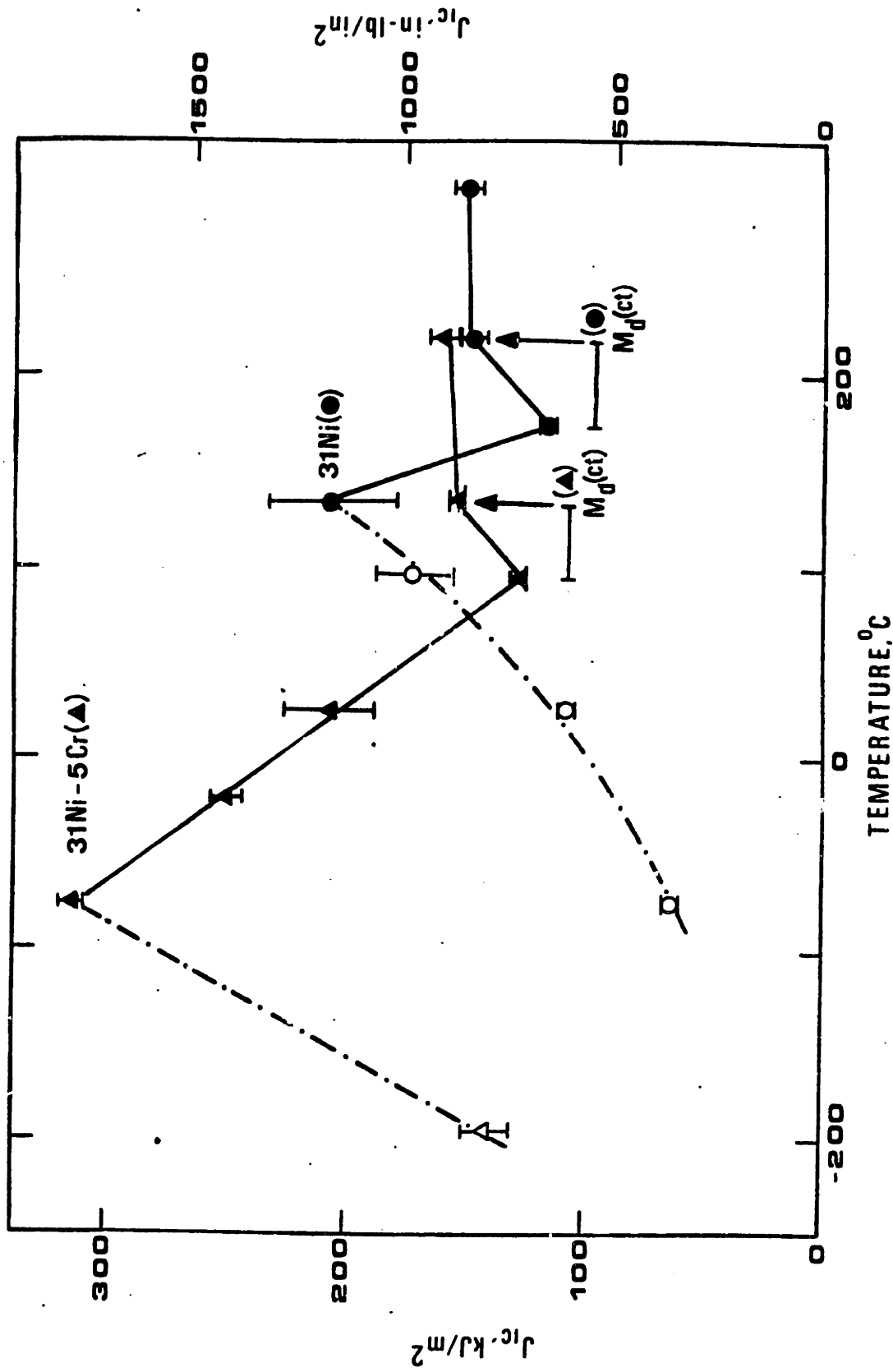


Figure 24 - J_{IC} versus temperature for the lower-carbon alloys. The dashed lines indicate premature failure. The horizontal error bars indicate the uncertainty in M_d temperatures. The vertical error bars represent 50% confidence level

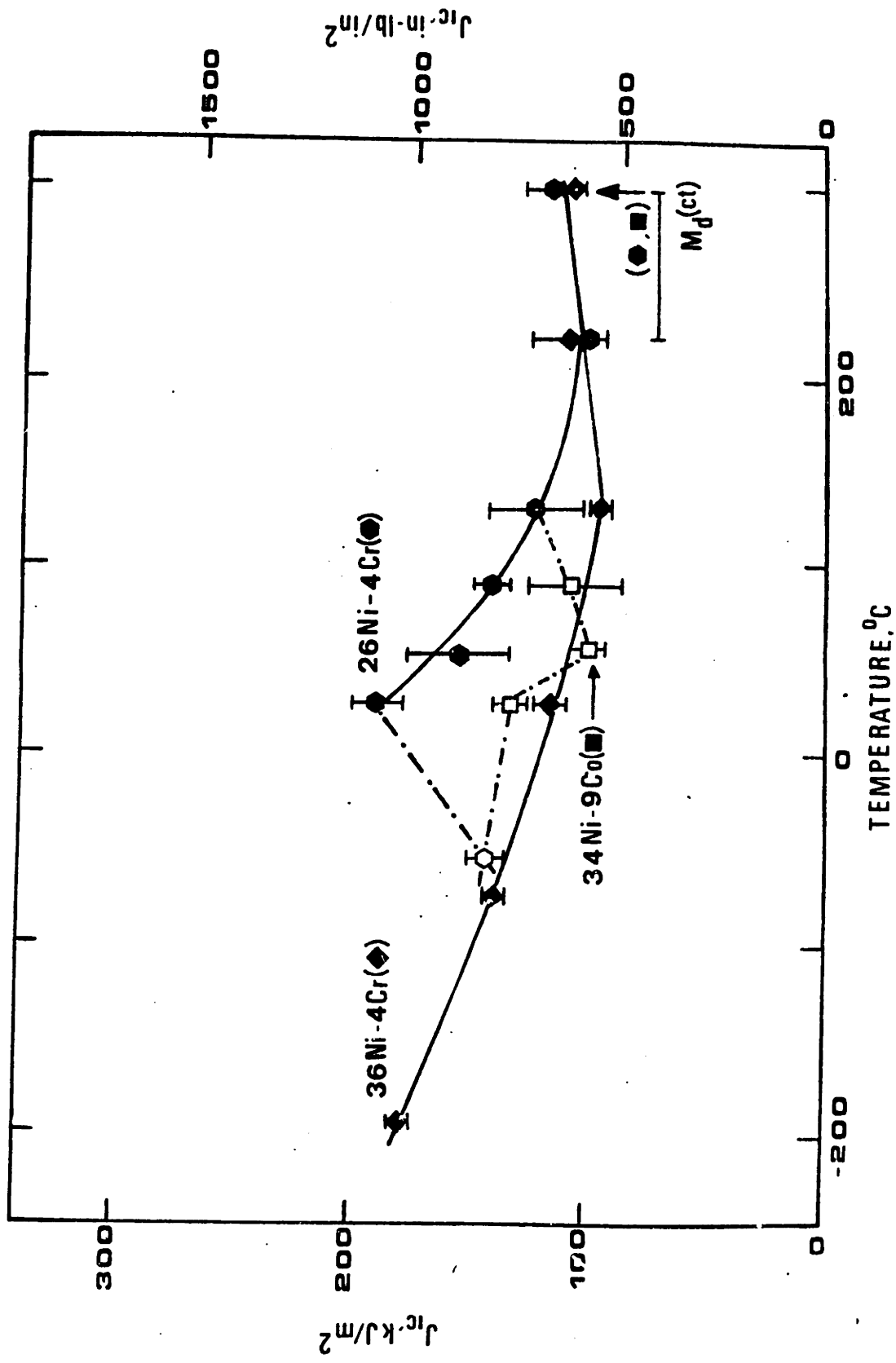


Figure 25 - J_{Ic} versus temperature for the higher-carbon alloys. The dashed-dotted lines indicate premature failure. The horizontal error bars indicate the uncertainty in M_d temperature. The vertical error bars represent 50% confidence level.

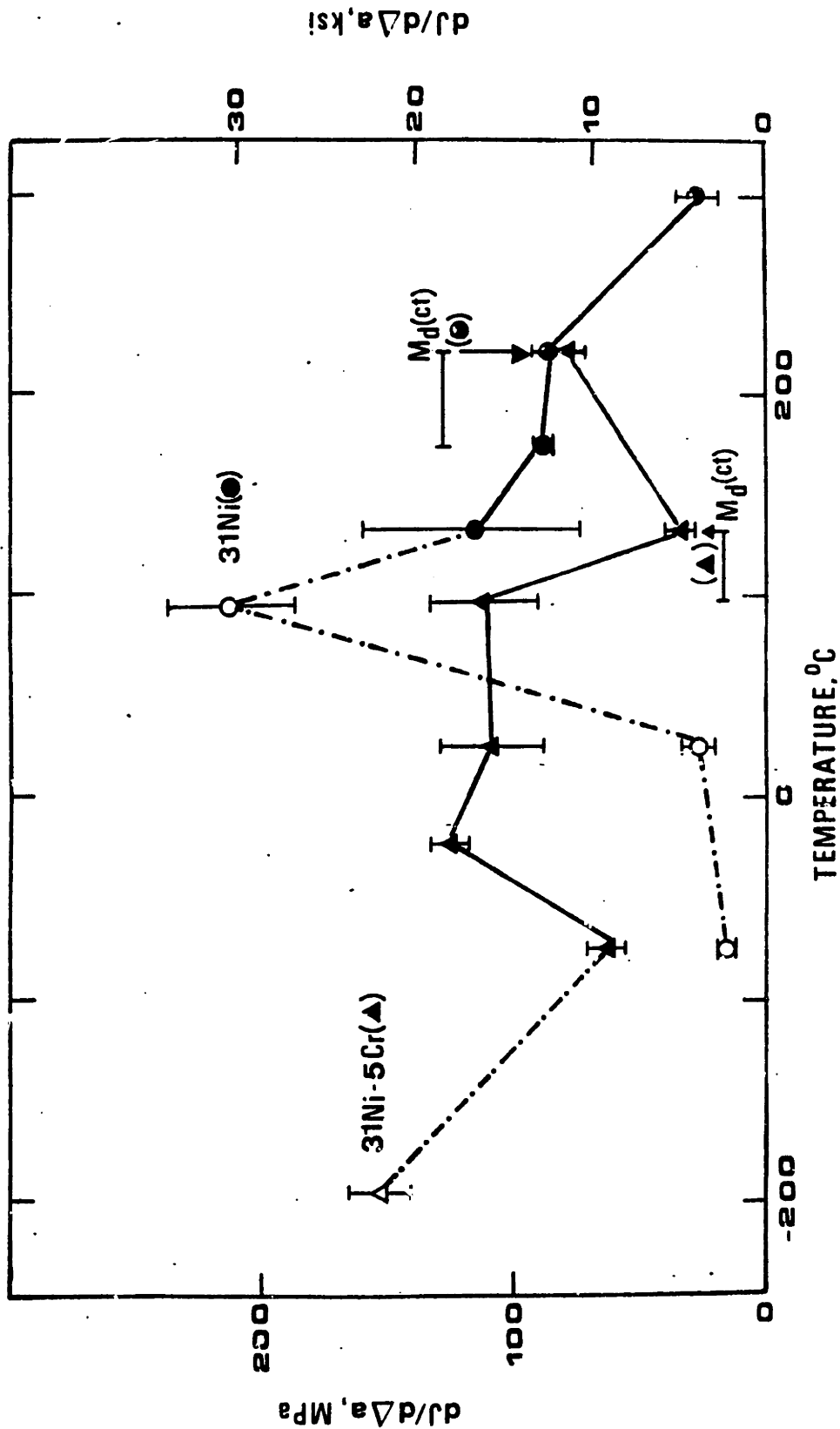


Figure 26 - $dJ/d\Delta a$ versus temperature for the lower-carbon alloys. The vertical error bars represent 50% confidence level. The horizontal error bars indicate uncertainty in M_d .

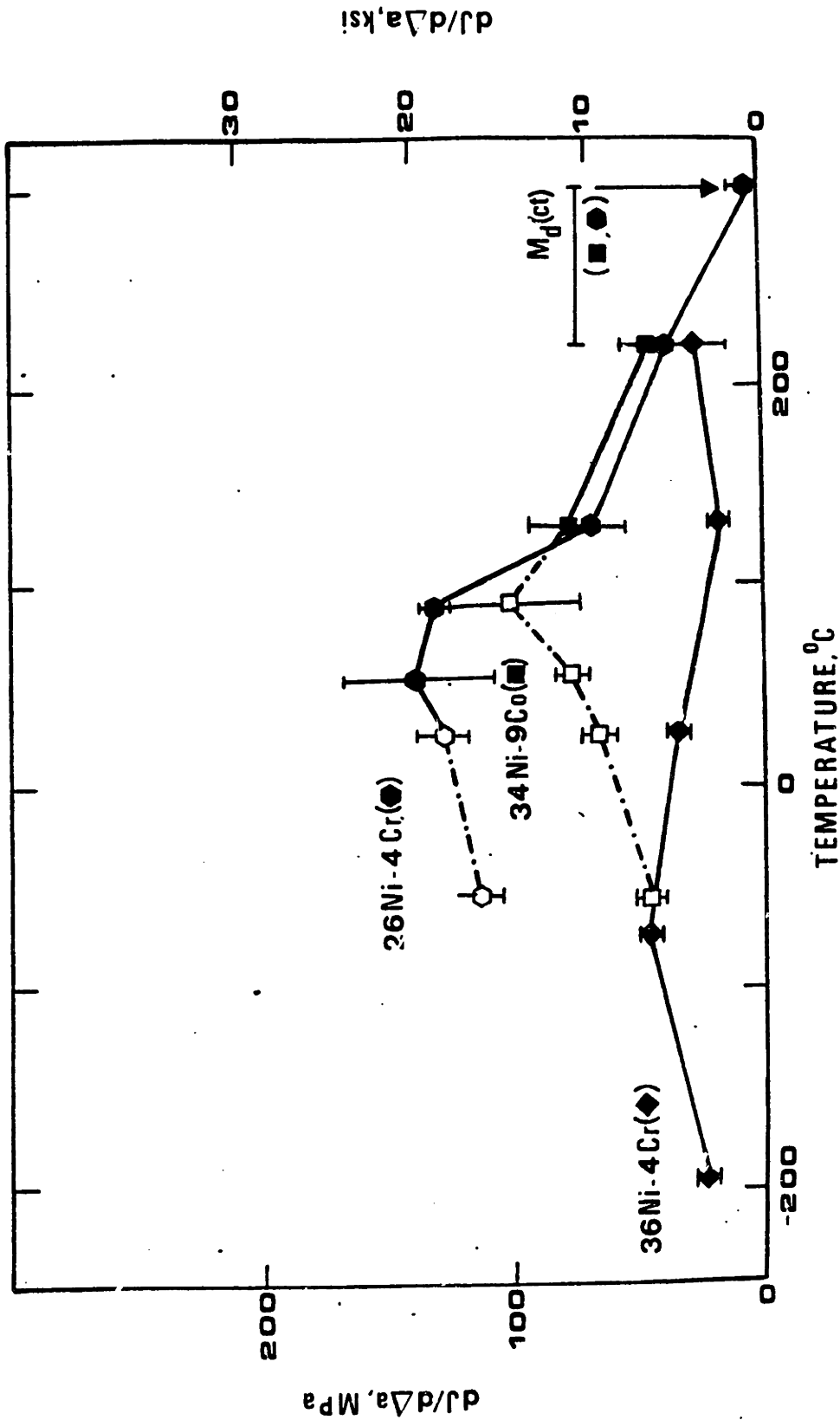
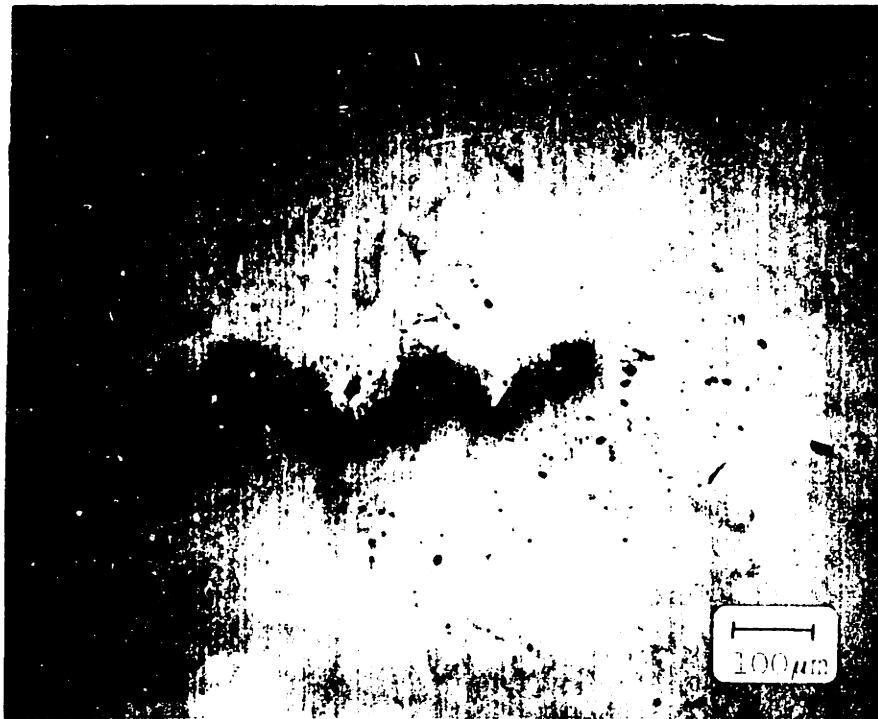


Figure 27 - $dJ/d\Delta a$ versus temperature for the higher-carbon alloys. The vertical error bars represent 50% confidence level. The horizontal error bars indicate the uncertainty in M_D .

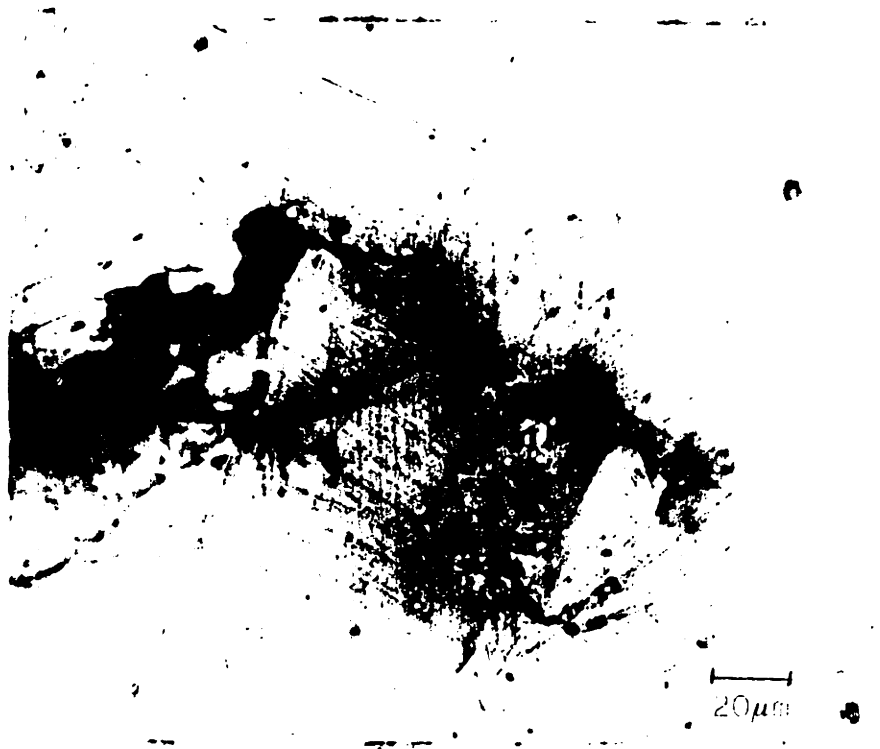
J_{IC} Results

As indicated in Figures 24 and 25, the general behavior of J_{IC} at temperatures lower than $M_d(ct)$ is similar to that observed for ϵ_{pu} . At temperatures slightly lower than $M_d(ct)$, a drop in J_{IC} is found due to the very first mechanically-induced martensite formed at the crack-tip. Figure 28 shows the small amount of transformation present at the crack-tip of 31Ni(L) tested at 175°C. By lowering the temperature, J_{IC} increases to a maximum and then decreases at still lower temperatures. The increase in toughness, as measured by J_{IC} , is once more promoted by mechanically-induced transformation, now occurring at the crack-tip. Figures 29 and 30 show the martensite present at the crack-tip of 31Ni(L) and 31Ni-5Cr(L) tested at their peak-toughness temperatures of 135°C and -75°C, respectively.

At temperatures lower than that of the toughness peak, large amounts of martensite are formed ahead of the crack-tip. A typical example is shown in Figure 31 for 31Ni(L) tested at 25°C. By comparing this with Figures 28 to 30, it is clear that the macroscopic mode of failure changed from the zig-zag to a flatter failure mode when large amounts of transformation took place. As with the tensile fracture, some cleavage and intergranular fracture occurred at these low temperatures. Figure 32 shows cleavage in the fracture surface of 31Ni(L) tested at 25°C, and Figure 33 shows intergranular fracture in 26Ni-4Cr(H) tested at -55°C.

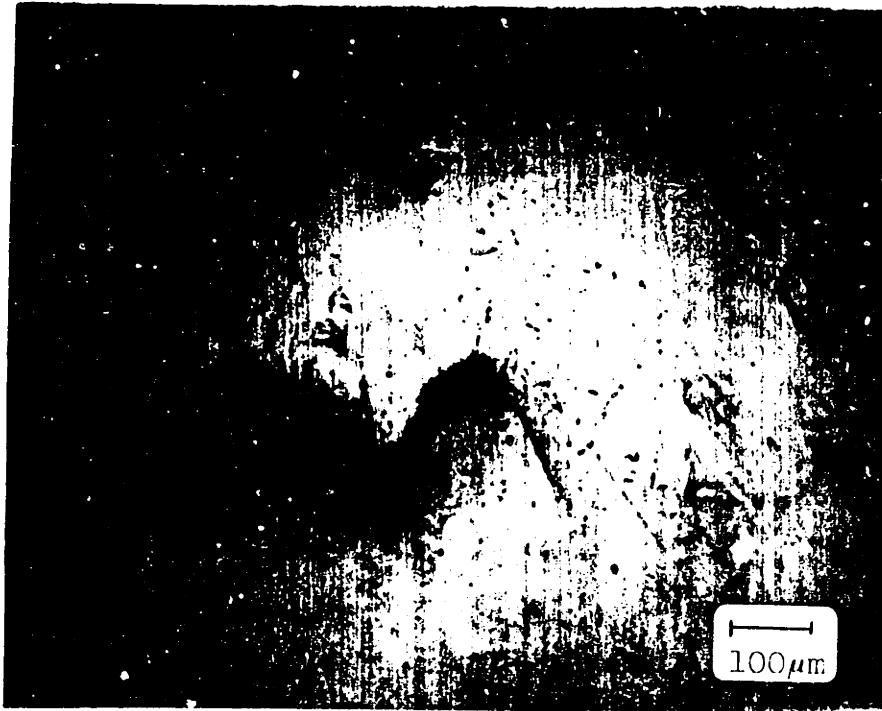


(a)

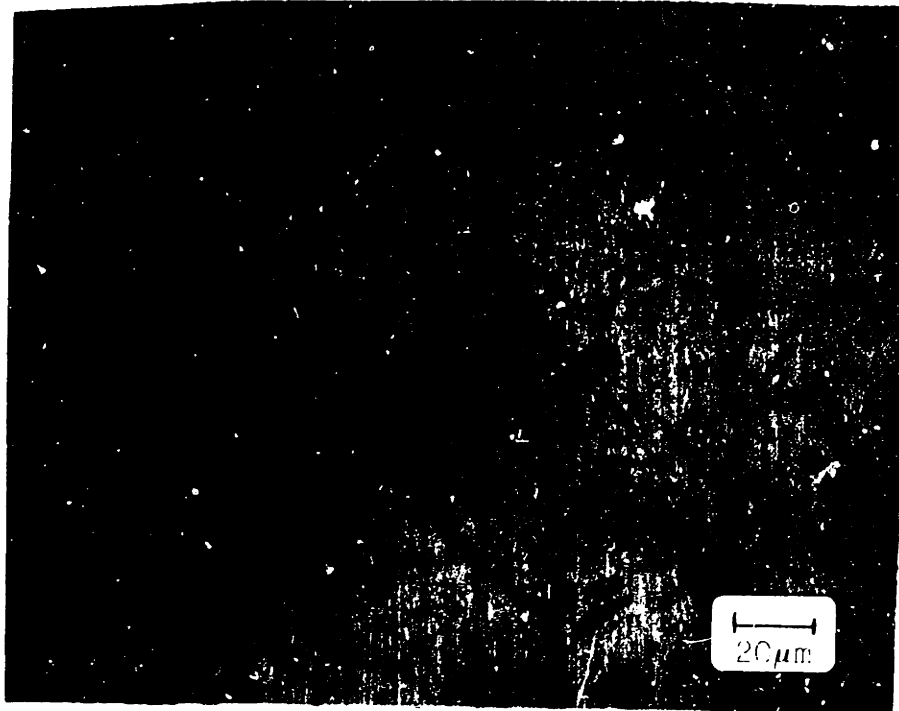


(b)

Figure 28 - Optical micrograph of the crack-tip of 31Ni(L) tested at 175°C: (a) 100X, (b) 500X

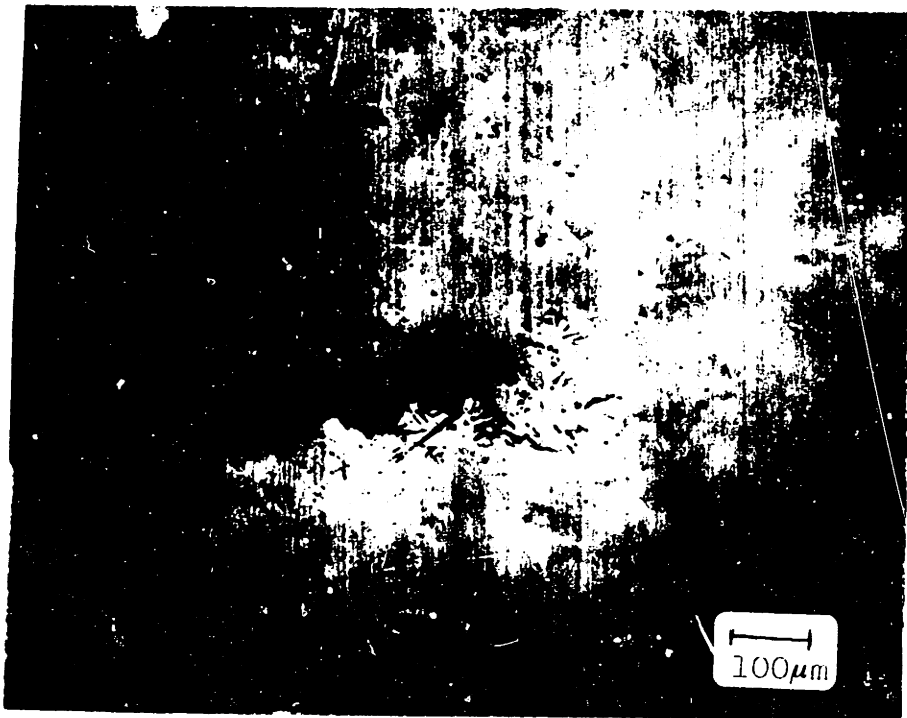


(a)

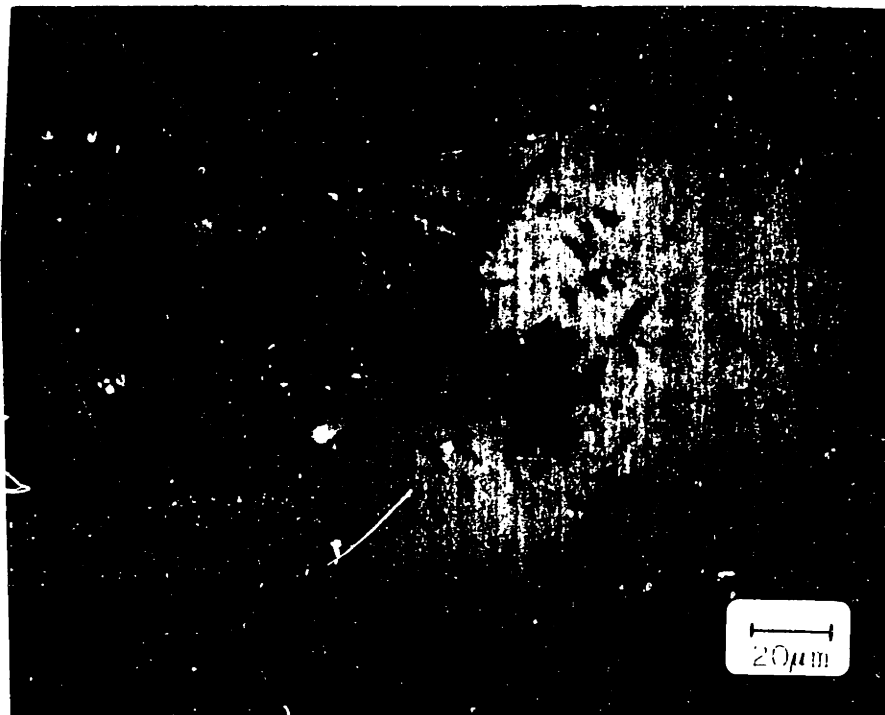


(b)

Figure 29 - Optical micrograph of the crack-tip of 31Ni(L) tested at 135°C: (a) 100X, (b) 500X.



(a)



(b)

Figure 30 - Optical micrograph of the crack-tip of 31Ni-5Cr(1.) tested at -75°C : (a) 100X, (b) 500X.



Figure 31 - Optical micrograph of the crack-tip of 31Ni(L) tested at 25°C.

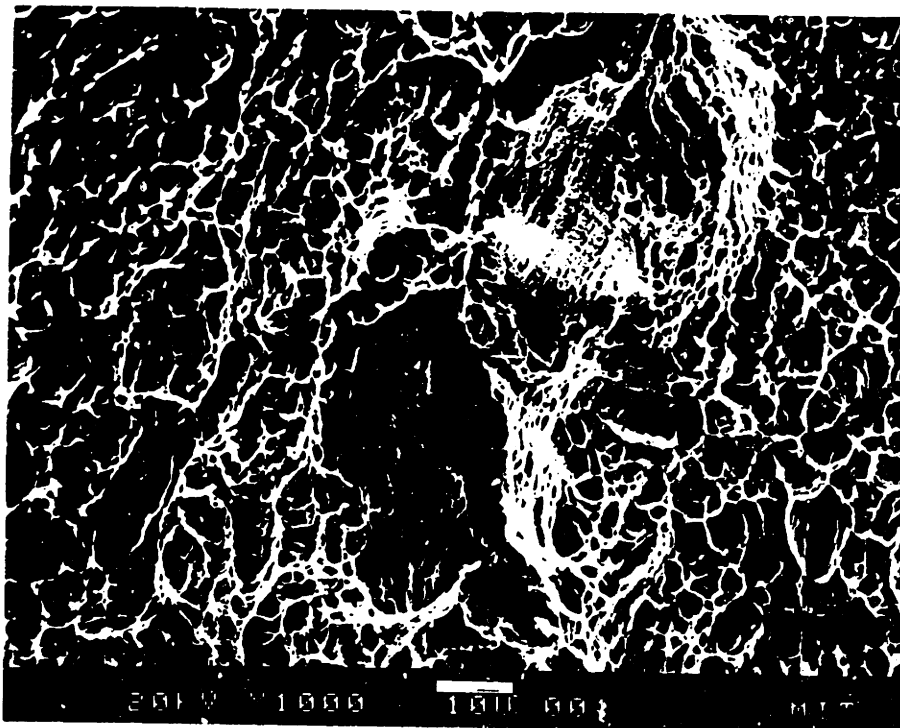


Figure 32 - SEM fractograph of fracture toughness specimen of 31Ni(L) tested at 25°C showing quasi-cleavage.

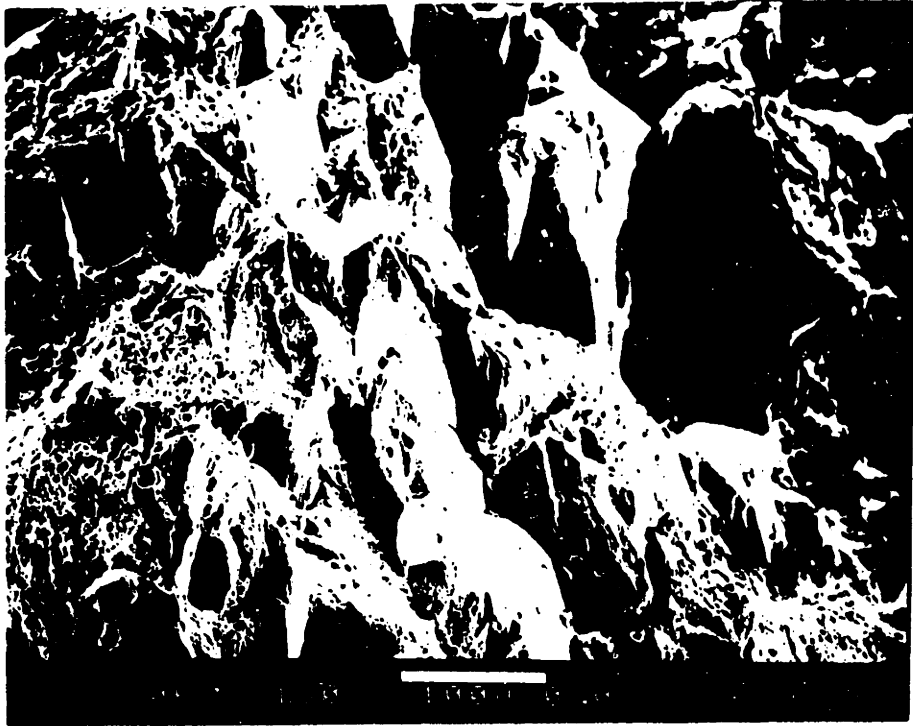


Figure 33 - SEM fractograph of fracture toughness specimen of 26Ni-4Cr(H) tested at -55°C showing intergranular fracture.

An apparently anomalous behavior in the J_{Ic} temperature dependence of 34Ni-9Co(H) sets in at temperatures lower than 55°C. At these temperatures J_{Ic} increases with lower temperature although large amounts of martensite are present in the crack-tip region. This seems to be a consequence of delamination changing the stress-state ahead of the crack-tip from plane strain to plane stress. Although a few delamination cracks were present in the lower-carbon alloys, much more delamination was present in the higher-carbon compositions tested at temperatures where moderate to large amounts of transformation took place at the crack-tip.

Resistance to Crack Growth

Concerning the resistance of the alloys studied here to the instability of crack growth, the tearing modulus given by Equation 20 cannot be taken definitely as a material parameter because w defined in Equation 19 varied only between 2 and 8 for all tests performed. Despite this, relative differences in $dJ/d\Delta a$ may be interpreted as relative differences in the material's resistance to the continuation of crack propagation.

Figures 26 and 27 indicate that mechanically-induced martensitic transformation enhances the resistance to crack propagation. The peaks observed in the temperature dependence of $dJ/d\Delta a$ for 31Ni(1), 26Ni-4Cr(H) and 34Ni-9Co(H) suggest that there is again a certain optimum stability condition to produce maximum toughness.

5.1 - Transformation Behavior

A comparison between Figures 12, 13 and 24 or 12, 14 and 25 indicates that for any specific alloy the temperature for the maximum of ϵ_{pu} is lower than that for the maximum in ϵ_f^n , and this is lower than that for the maximum in J_{Ic} .

The lower temperature for the changes in uniform elongation is expected because the onset of necking is a phenomenon occurring at relatively small plastic strains as compared to the fracture process that determines ϵ_f^n and J_{Ic} . In order to have transformation occurring at such low strains, the austenite must have less stability, or, in other words, to be deformed at lower temperatures. Superimposed on this, the effect of the stress-state on the stability of the stress-assisted transformation also contributes to the observed shift in temperature.

As predicted by Equation 4^(30,41), the stress-assisted transformation stress is reduced under a triaxial stress-state due to the increase in $d\Delta G/d\bar{\sigma}$. This produces a shift in the $M_s^{\bar{\sigma}}$ temperature to higher levels and, consequently, the higher transformation rate associated with formation of stress-assisted martensite is present at higher temperatures as compared to the uniaxial-tension case before necking. Similarly, the temperature difference between the changes in ϵ_f^n and J_{Ic} can be attributed to differences in

triaxiality between the stress-states in the necked region and ahead of the crack-tip.

The predicted shift in M_S^σ temperature due to triaxiality is qualitatively verified by the results shown in Table IV. A quantitative analysis can be done by fitting Equation 4 to the experimentally measured uniaxial tension stress-assisted transformation-stress for 31Ni(L) and 34Ni-9Co(H). Considering the variation in $d\Delta G/d\bar{\sigma}$ due to triaxiality, calculated temperature dependence for the stress-assisted transformation-stress ahead of the crack-tip is obtained. The predicted shifts in M_S^σ when the stress-state is changed from uniaxial tension to that ahead of the crack-tip are 55°C and 95°C for 31Ni(L) and 34Ni-9Co(H), respectively. Using $M_S^\sigma(u) \simeq -20^\circ\text{C}$ for 31Ni(L), the results listed in Table IV indicate experimentally determined shifts varying from 115°C to 155°C for 31Ni(L) and equal to 100°C for 34Ni-9Co(H). While the agreement between experimentally measured and calculated M_S^σ shifts is very good for 34Ni-9Co(H), the same is not true for 31Ni(L). This discrepancy is probably due to the previously discussed uncertainty in the determination of $M_S^\sigma(u)$ for 31Ni(L), as well as the uncertainty in the actual slope of the temperature dependence of the yield strength of 31Ni(L) at $T < M_S^\sigma(u)$.

As also indicated in Table IV, M_d is generally comparable for both the necked region and the crack-tip. This can be explained by noting that while the higher triaxiality present at the crack-tip as compared to that of the necking

enhances the tendency for mechanically-induced martensite formation, it is more detrimental to the material fracture resistance, lowering the strain to failure. Apparently the two contributions compensate each other.

$M_S^\sigma(ct)$ can also be regarded as the temperature for which the austenite plastic zone size is exactly equal to the transformation zone size ahead of the crack-tip. At temperatures lower than $M_S^\sigma(ct)$, the transformation zone is larger than the plastic zone estimated from σ_y for slip, while the opposite is true at temperatures greater than $M_S^\sigma(ct)$ (see Figure 34). Based on the Rice and Rosengren calculations⁽⁵²⁾ the slip plastic zone size ahead of the crack-tip for the stable austenites studied here ($n \approx 0.1$) is:

$$r_s(0) = 0.0025 \frac{JE}{(\sigma_y)^2} \cdot \quad [23]$$

The half-height of the slip plastic zone is given by:

$$r_s(\pi/2) = 0.2114 \frac{JE}{(\sigma_y)^2} \cdot \quad [24]$$

For small crack extensions $J = J_{Ic}$. E and σ_y are respectively the Young's modulus and austenite yield strength.

Table XV compares the calculated $r_s(0)$ and $r_s(\pi/2)$ values with measured equivalent transformation zone-size

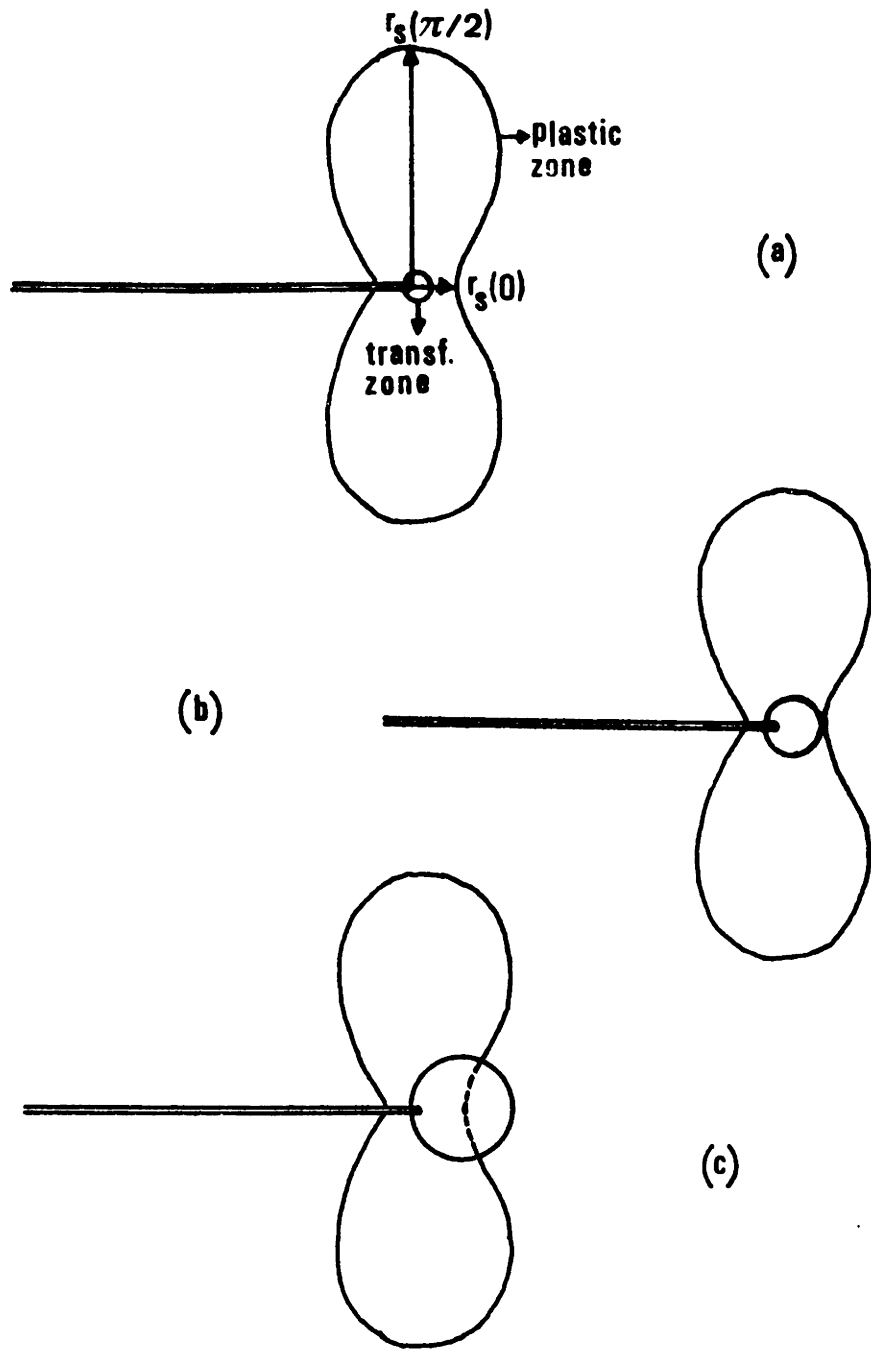


Figure 34 - Schematic comparison between crack-tip plastic and transformation zones at: (a) $M_s^\sigma < T_1 < M_d(ct)$, (b) $T_2 = M_s^\sigma(ct)$, $T_3 < M_s^\sigma(ct)$

parameters, $r_t(0)$ and $r_t(\pi/2)$. It is clear that at the $M_S^\sigma(ct)$, the size of the plastic zone ahead of the crack-tip as predicted by Equation 23 matches very well with the experimentally determined transformation zone $r_s(0)$. As expected and indicated in Figure 34, at $M_S^\sigma(ct)$ the half-height of the austenitic slip-plastic zone, $r_s(\pi/2)$, is larger than the corresponding transformation half-height, $r_t(\pi/2)$. This is due to the fact that at $\theta = \pi/2$ the triaxiality is smaller than at $\theta = 0$ and M_S^σ in this region is smaller than $M_S^\sigma(ct)$. In other words, for $T = M_S^\sigma(ct)$, at $\theta = \pi/2$, this same temperature is higher than the local M_S^σ ($T = M_S^\sigma(ct) > M_S^\sigma(\pi/2)$) and consequently $r_s(\pi/2) > r_t(\pi/2)$.

TABLE XV : CALCULATED PLASTIC ZONES (s) AND MEASURED TRANSFORMATION ZONE (t) SIZES

a) 31Ni-5Cr(L)

	T(°C)	$r_s(0)$ (μm)	$r_t(0)$ (μm)	$r_s(\pi/2)$ (μm)	$r_t(\pi/2)$ (μm)
$M_s^{\sigma}(ct) \rightarrow$	-196	32.3	100	2730	400
	-75	105.0	50	8900	200

b) 26Ni-4Cr(H)

	T(°C)	$r_s(0)$ (μm)	$r_t(0)$ (μm)	$r_s(\pi/2)$ (μm)	$r_t(\pi/2)$ (μm)
$M_s^{\sigma}(ct) \rightarrow$	-55	43.3	200	3660	500
	25	67.4	100	5700	300
	55	57.7	50	4880	100
	90	51.6	10	4370	50

c) 31Ni(L)

	T(°C)	$r_s(0)$ (μm)	$r_t(0)$ (μm)	$r_s(\pi/2)$ (μm)	$r_t(\pi/2)$ (μm)
$M_s^{\sigma}(ct) \rightarrow$	-75	21.4	875	1810	1000
	25	37.6	500	3180	500
	95	67.4	200	5700	250
	135	81.5	50	6890	100

d) $^{34}\text{Ni}-9\text{Co}(\text{H})$

	$T(^{\circ}\text{C})$	$r_s(0)(\mu\text{m})$	$r_t(0)(\mu\text{m})$	$r_s(\pi/2)(\mu\text{m})$	$r_t(\pi/2)(\mu\text{m})$
	-55	42.5	1000	3590	1250
	25	47.3	1250	4000	1125
	55	36.5	500	3090	875
	90	38.3	250	3240	400
$M_s^{\square}(\text{ct}) \rightarrow$	135	41.0	80	3470	200

5.2 - Transformation Stability

5.2.1 - Normalized Temperature Interval

By analysing Figure 12, it can be noted that the changes in uniform elongation for the different alloys are shifted in temperature according to their alloy transformation stability. The same is seen in Figures 13 and 14 for the strain to failure and in Figures 24 and 25 for J_{IC} . A way to normalize all the data with respect to the different stabilities is by defining a non-dimensional temperature interval equal to:

$$\eta = \frac{(T - M_d)}{(M_d - M_s^\sigma)} \quad [25]$$

where the M_s^σ and M_d temperatures are those corresponding to the respective stress-state. The term $M_s^\sigma - M_d$ takes into account the differences in stacking-fault energy and $\Delta S^{\gamma \rightarrow \alpha}$ between the various alloys. Both these parameters influence the kinetics of strain-induced martensite formation.

5.2.2 - Uniform Elongation Relative Enhancement

Figure 35 illustrates the variation of the relative increments in uniform elongation with η for 31 Ni(L) and 34Ni-9Co(H). The increments are relative to the austenitic uniform elongation given respectively by 31Ni-5Cr(L) and 36Ni-4Cr(H) at the same temperature. The values of M_s^σ and M_d entering in η are those for uniaxial tension

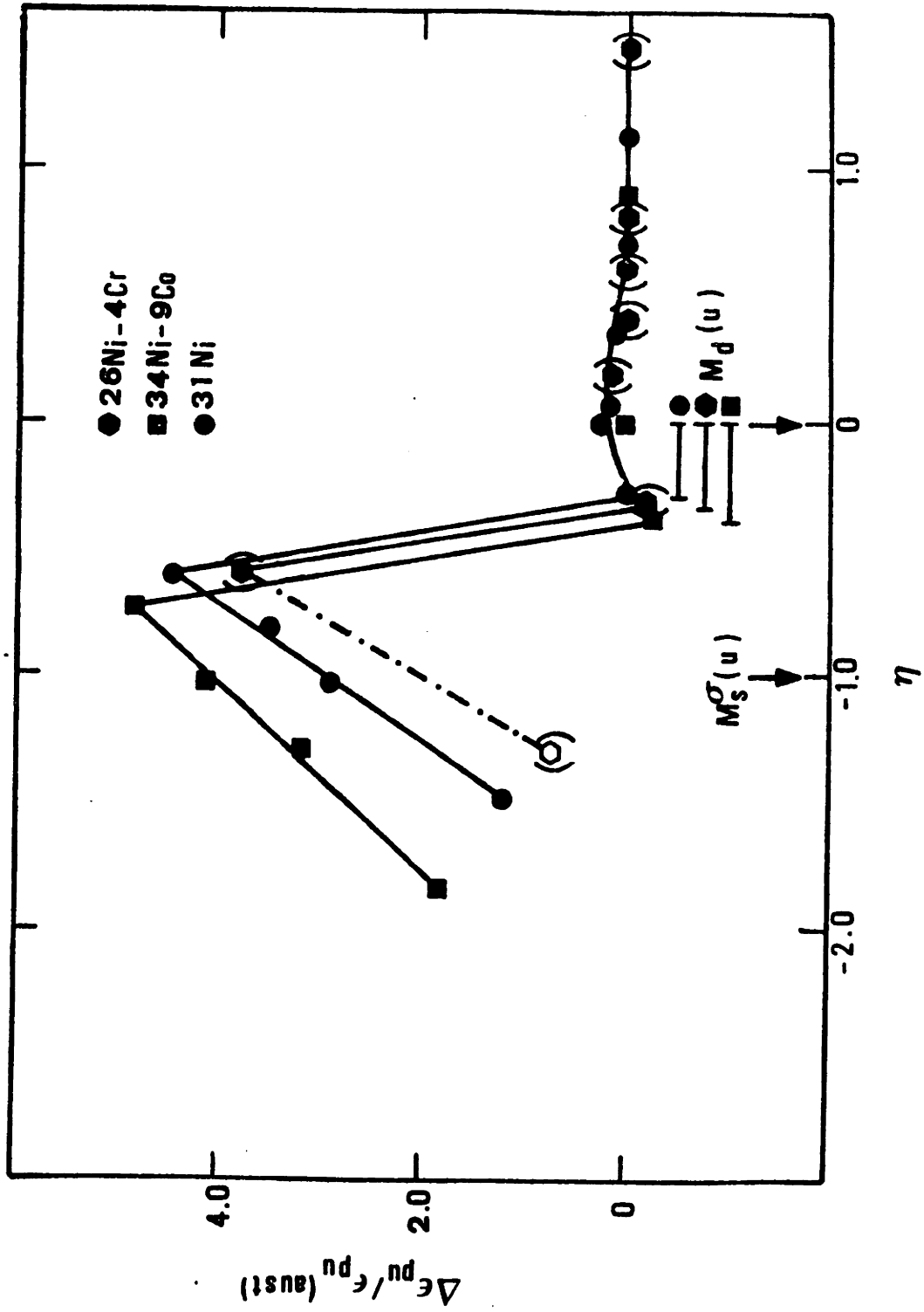


Figure 35 - Uniform elongation relative enhancement versus normalized temperature interval

before necking ($M_S^\sigma(u)$ and $M_d(u)$ listed in Table IV). The peaks in the relative enhancement in uniform elongation occurring at the same η for all alloys reinforce the idea that an optimum stability condition is required to obtain the highest ϵ_{pu} . By choosing $M_S^\sigma(u)$ for 26Ni-4Cr(H) equal to -120°C , as discussed in section 4.1, Figure 35 shows that the maximum in $\Delta\epsilon_{pu}/\epsilon_{pu}(\text{aust})$ also occurs at the same η as for the other two alloys (data in parentheses for 26Ni-4Cr(H)).

5.2.3 - Strain to Failure Relative Enhancement

Figure 36 shows the temperature dependence of the true strain to failure for stable lower- and higher-carbon austenites. The curve for higher-carbon austenites is that obtained for 36Ni-4Cr(H). At $T \geq 135^\circ\text{C}$, $\epsilon_f^n(\text{aust})$ for lower-carbon austenites are given by the results obtained for 31Ni-5Cr(L), which does not transform at this temperature. As compared to the higher-carbon case, at $T \geq 135^\circ\text{C}$ an apparent reversed temperature dependence of $\epsilon_f^n(\text{aust})$ is observed for the lower-carbon alloys. Possible reasons for this phenomenon are mentioned in connection with the J_{IC} relative enhancement discussed in section 5.2.4. Due to the lack of information about $\epsilon_f^n(\text{aust})$ for the lower-carbon alloys at $T < 135^\circ\text{C}$, and also due to the distinct temperature dependence of

$\epsilon_f^n(\text{aust})$ at $T \geq 135^\circ\text{C}$ for lower- and higher-carbon alloys, an average between all measured lower-carbon $\epsilon_f^n(\text{aust})$ is taken as the baseline austenitic lower-carbon $\epsilon_f^n(\text{aust})$ at $T < 135^\circ\text{C}$. This is indicated as a dashed line in Figure 36.

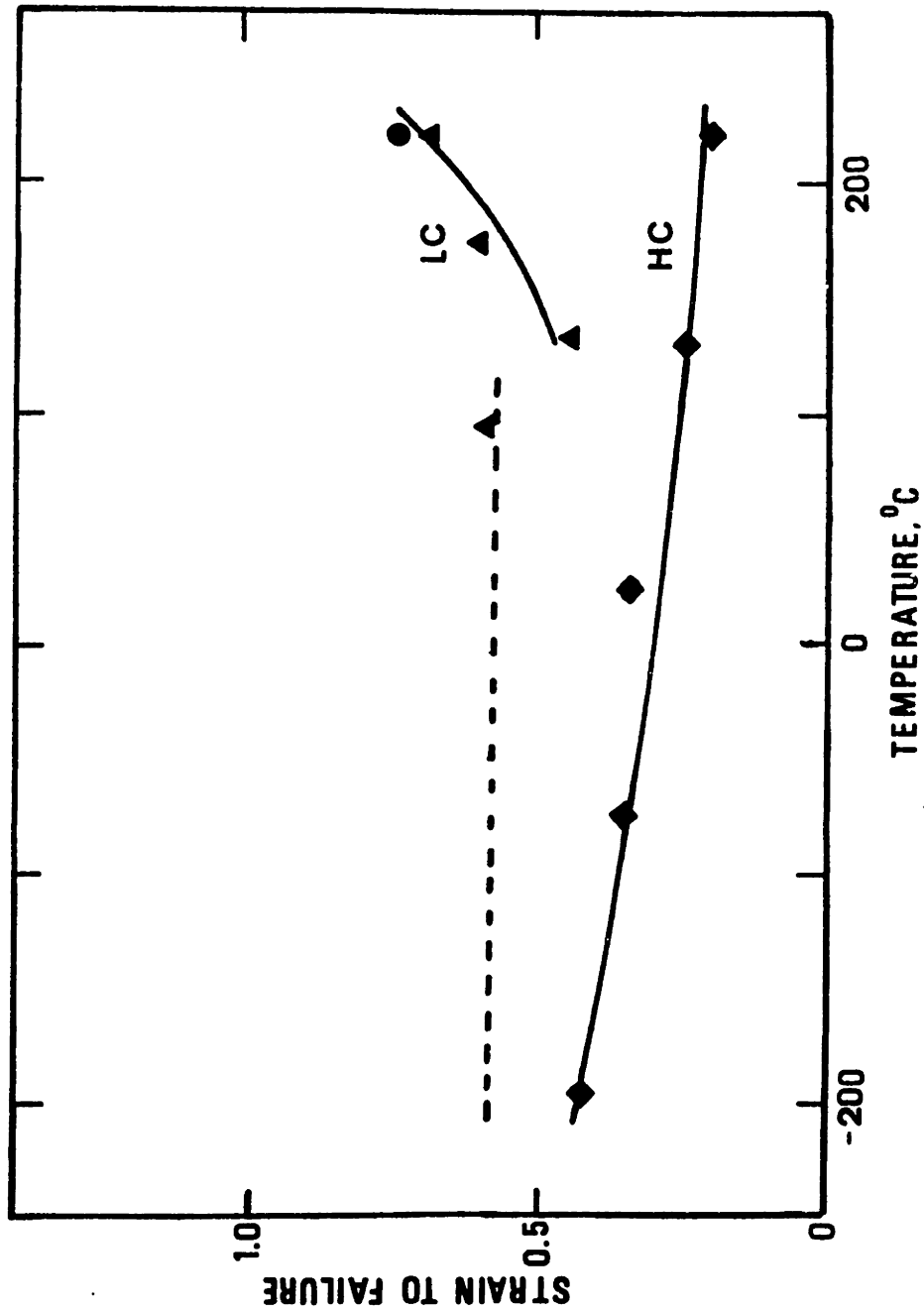


Figure 36 - Austenitic temperature dependence of the strain to failure of both lower- and higher-carbon alloys. The dashed line indicates the lower-carbon stable austenite baseline values used in the estimation of $\Delta\epsilon_f^n$ for $T < 135^\circ\text{C}$

Figure 37 shows the dependence of the absolute increment in the true strain to failure as a function of η . The increments in ϵ_f^n are calculated with respect to $\epsilon_f^n(\text{aust})$ given in Figure 36. In this case M_s^σ and M_d are the values estimated for the necked region ($M_s^\sigma(n)$ and $M_d(n)$ given in Table IV). $M_s^\sigma(n)$ for 31Ni-5Cr(L), which could not be precisely determined because no test was run at $T < -196^\circ\text{C}$, was taken as equal to -196°C . This value gives $M_s^\sigma(n) - M_d(n)$ for 31Ni-5Cr(L) approximately equal to the same difference for 26Ni-4Cr(H). This seems reasonable, since the two chromium-containing alloys have the same $\Delta S^{\gamma \rightarrow \alpha} \approx 4.0 \text{ J/mole}^\circ\text{K}$, and are expected to have also similar stacking-fault energies.

A comparison between the results for 26Ni-4Cr(H) and 34Ni-9Co(H) shown in Figure 37 suggests that a larger increment in the strain to failure at the same η is obtained for the alloy with the higher transformational volume change, 26Ni-4Cr(H). The effect is not apparent for the lower-carbon alloys probably due to the uncertainty in the value of austenitic ϵ_f^n at temperatures below 135°C .

5.2.4 - J_{IC} Relative Enhancement

Figure 38 shows the temperature dependence of J_{IC} for stable higher- and lower-carbon austenites. The curve for the higher-carbon austenites are given by the results obtained for 36Ni-4Cr(H). For $T \geq 135^\circ\text{C}$, the austenitic lower-carbon J_{IC} is given directly from experimental results.

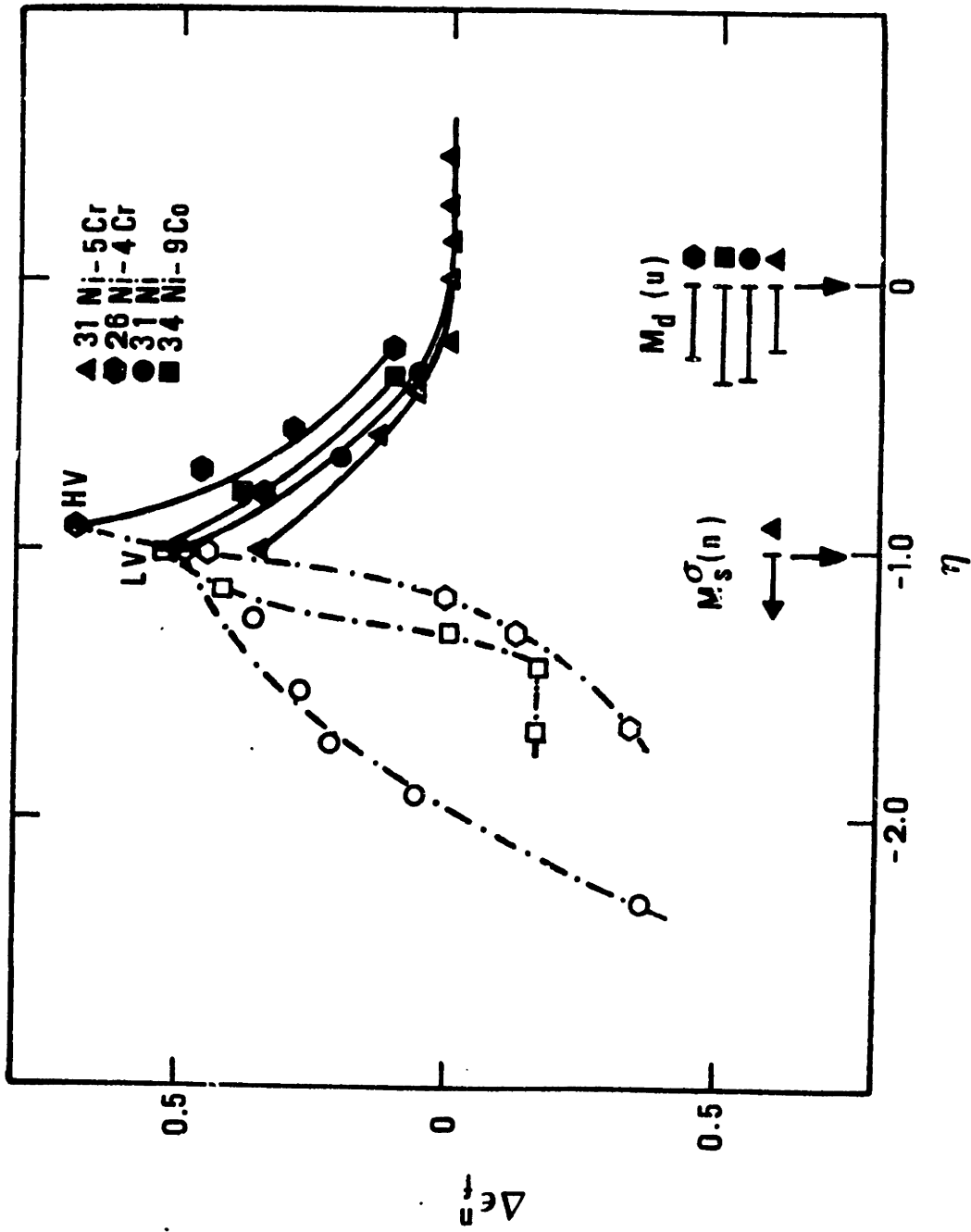


Figure 37 - Strain to fracture absolute enhancement versus normalized temperature interval

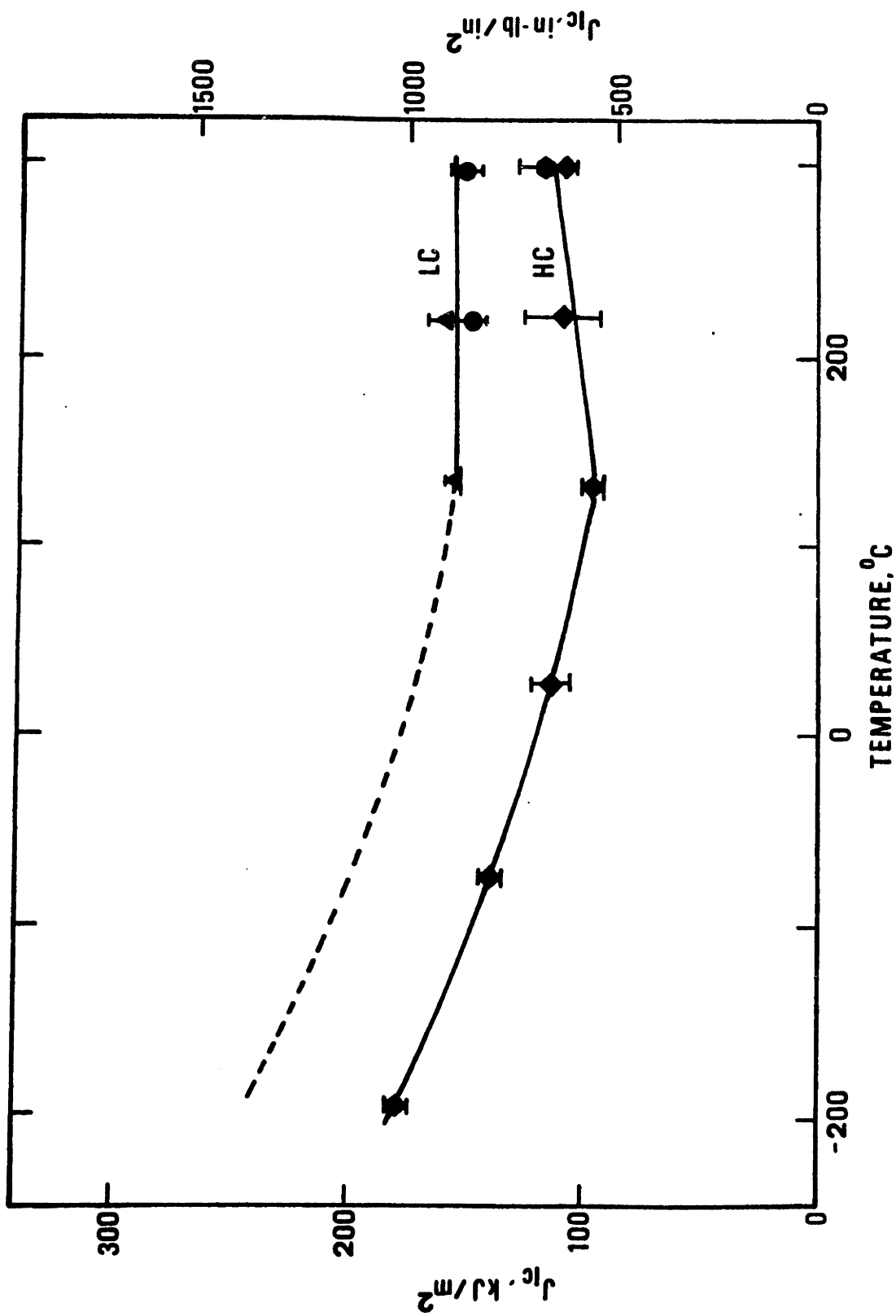


Figure 38 - Austenitic temperature dependence of J_{Ic} for both lower- and higher-carbon alloys. The dashed line indicates the lower-carbon stable austenite baseline values used in the calculation of $\Delta J_{Ic}/J_{Ic}(\text{aust})$ for $T < 135^\circ\text{C}$

Figure 38 indicates that both group of alloys have similar J_{IC} temperature dependence at $T \geq 135^{\circ}\text{C}$, only shifted in absolute value due to the lower intrinsic toughness of the higher-carbon austenites. Based on this, it seems reasonable to assume a J_{IC} temperature dependence for the lower-carbon at $T < 135^{\circ}\text{C}$ parallel to that for the higher-carbon alloys, but passing through the experimental results measured at $T \geq 135^{\circ}\text{C}$. This is shown as a dashed line in Figure 38.

The reversed J_{IC} temperature dependence of austenite at $T \geq 135^{\circ}\text{C}$ may be a consequence of change in the slip mode from planar at lower temperatures to wavy slip at higher. Also geometry changes in the crack-tip due to plastic deformation may be contributing to the toughness enhancement by reducing the triaxiality ahead of the crack-tip. Similar reasons may explain the reversed temperature dependence of $\epsilon_f^n(\text{aust})$ for lower-carbon alloys.

Figure 39 shows the dependence of the relative increments in J_{IC} as a function of η . M_s^{σ} and M_d are the estimated values for the crack-tip ($M_s^{\sigma}(\text{ct})$ and $M_d(\text{ct})$ from Table IV). The austenitic values are those given in Figure 38. Figure 39 indicates higher toughness for the alloys with larger transformational volume expansion. Furthermore, a comparison between Figures 35, 37, and 39 indicates that for all alloys the rising part of ϵ_f^n and $\Delta J_{IC}/J_{IC}(\text{aust})$ at decreasing temperatures from M_d are spread over larger values of η as compared to $\Delta \epsilon_{pu}/\epsilon_{pu}(\text{aust})$. This may also be a

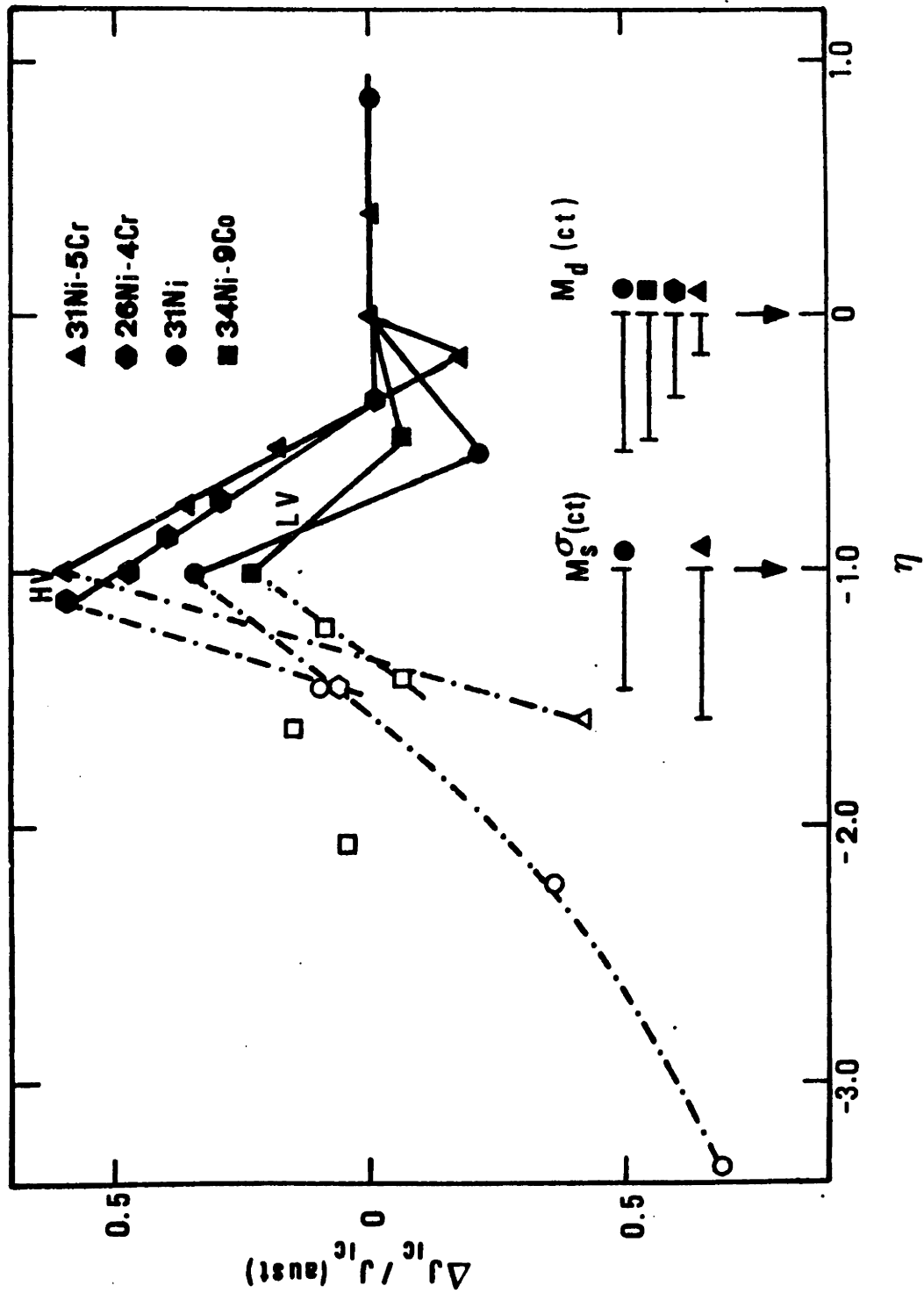


Figure 39 - J_{IC} relative enhancement versus normalized temperature interval

consequence of the transformational expansion. A more detailed analysis of the influence of the transformational volume change in the ductility enhancement under a triaxial stress-state will be given in sections 5.4 and 5.5.

5.3 - Strain Hardening and Flow Stability

The changes in uniform elongation of metastable austenitic steels can be understood by analysing how the mechanically-induced transformation affects the flow behavior of these alloys. A typical true-stress, true-plastic-strain curve when no transformation takes place is shown in Figure 40 (31Ni(L) tested at 95°C, $\eta_u=0$). The shape of the curve shows the usual downward curvature, starting with a very large value of the strain-hardening rate $\bar{h} = d\bar{\sigma}/d\bar{\epsilon}$; \bar{h} decreases with further straining up to a point where $\bar{h} = \bar{\sigma}$ and necking takes place.

Figure 41 shows the $\bar{\sigma}$ versus $\bar{\epsilon}$ curve for 31Ni(L) tested at the temperature for the maximum in uniform elongation (25°C, $\eta_u=-0.61$). The dynamic softening is present at low plastic strains promoting an early drop in the values of \bar{h} . Before final necking occurs, however, the strain-hardening contribution of the transformation promotes a relatively smooth increase in both $\bar{\sigma}$ and \bar{h} , delaying the plastic instability to very large strains. At this temperature the combination of dynamic softening and the work-hardening contribution of the transformation is optimum. The necking instability is delayed to the largest plastic strain.

A typical $\bar{\sigma}$ versus $\bar{\epsilon}$ curve for 31Ni(L) tested at temperatures lower than that of the maximum in uniform elongation is shown in Figure 42 ($T = -75^\circ\text{C}$, $\eta_u = -1.48$). The dynamic softening is present from the beginning of

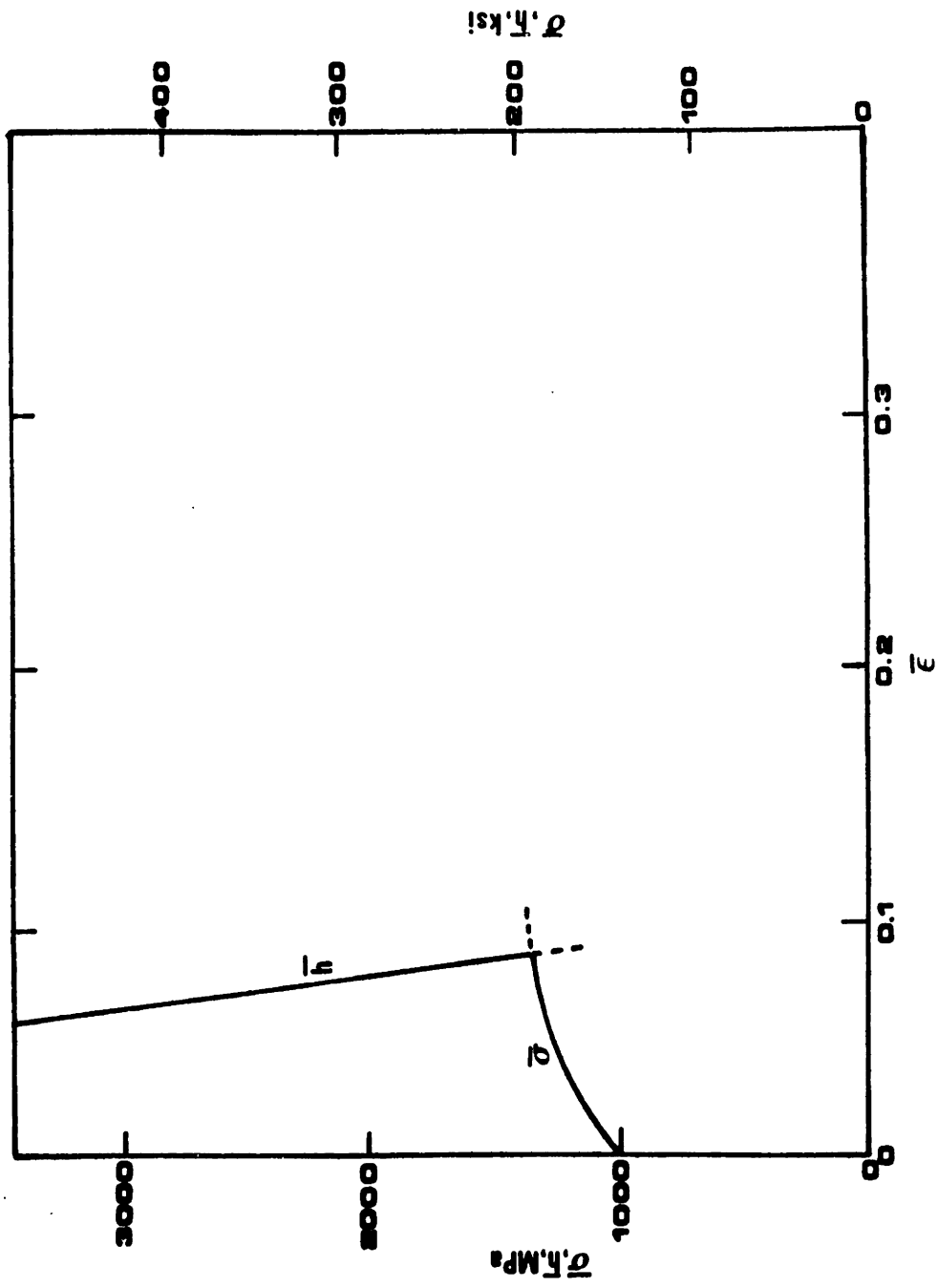


Figure 40 - True-stress and strain-hardening rate versus true-plastic-strain up to necking for 31 Ni(L) tested at 900°C.

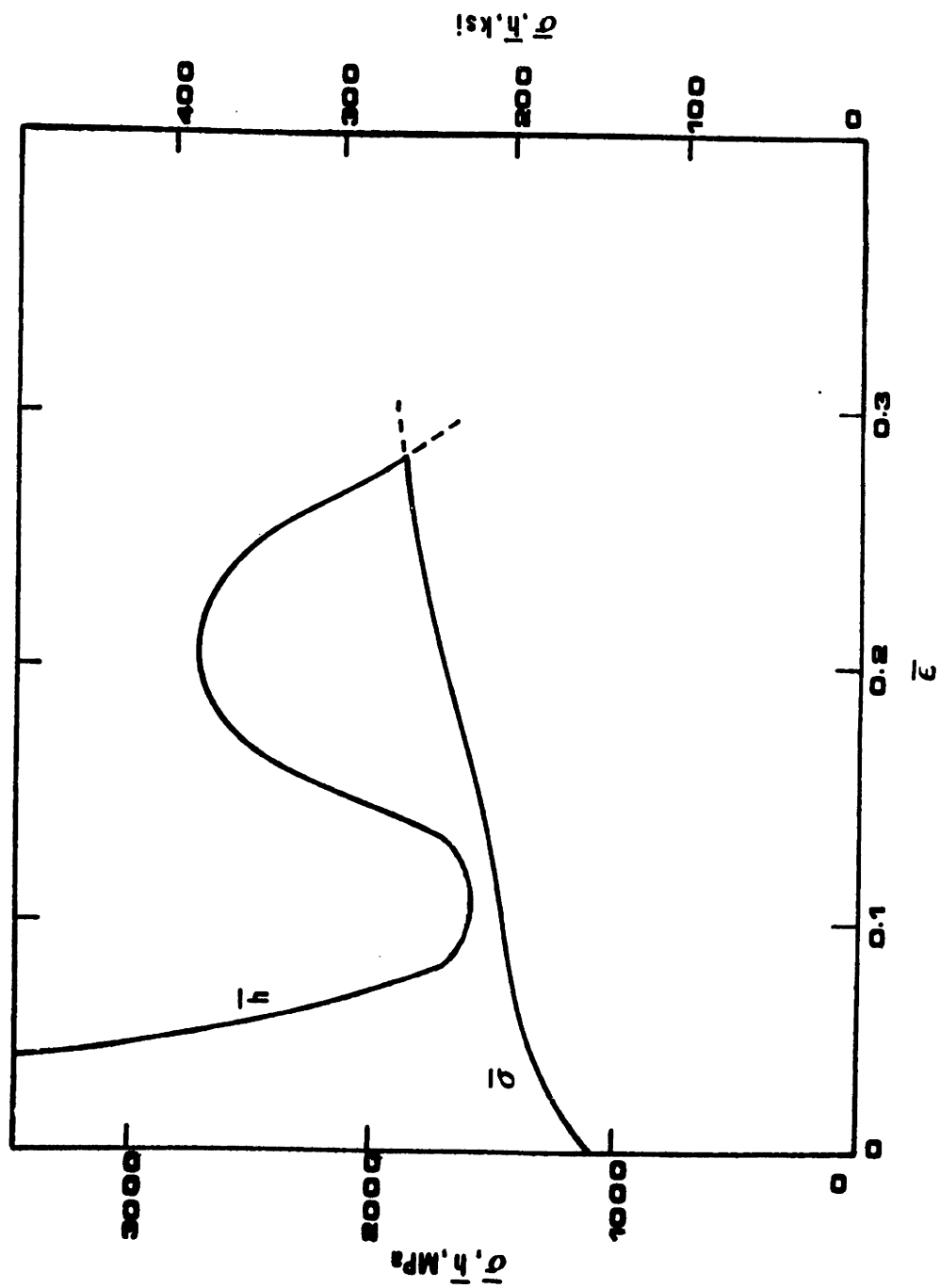


Figure 41 - True-stress and strain-hardening rate versus true-plastic-strain up to necking for 31Ni(L) tested at 25°C.

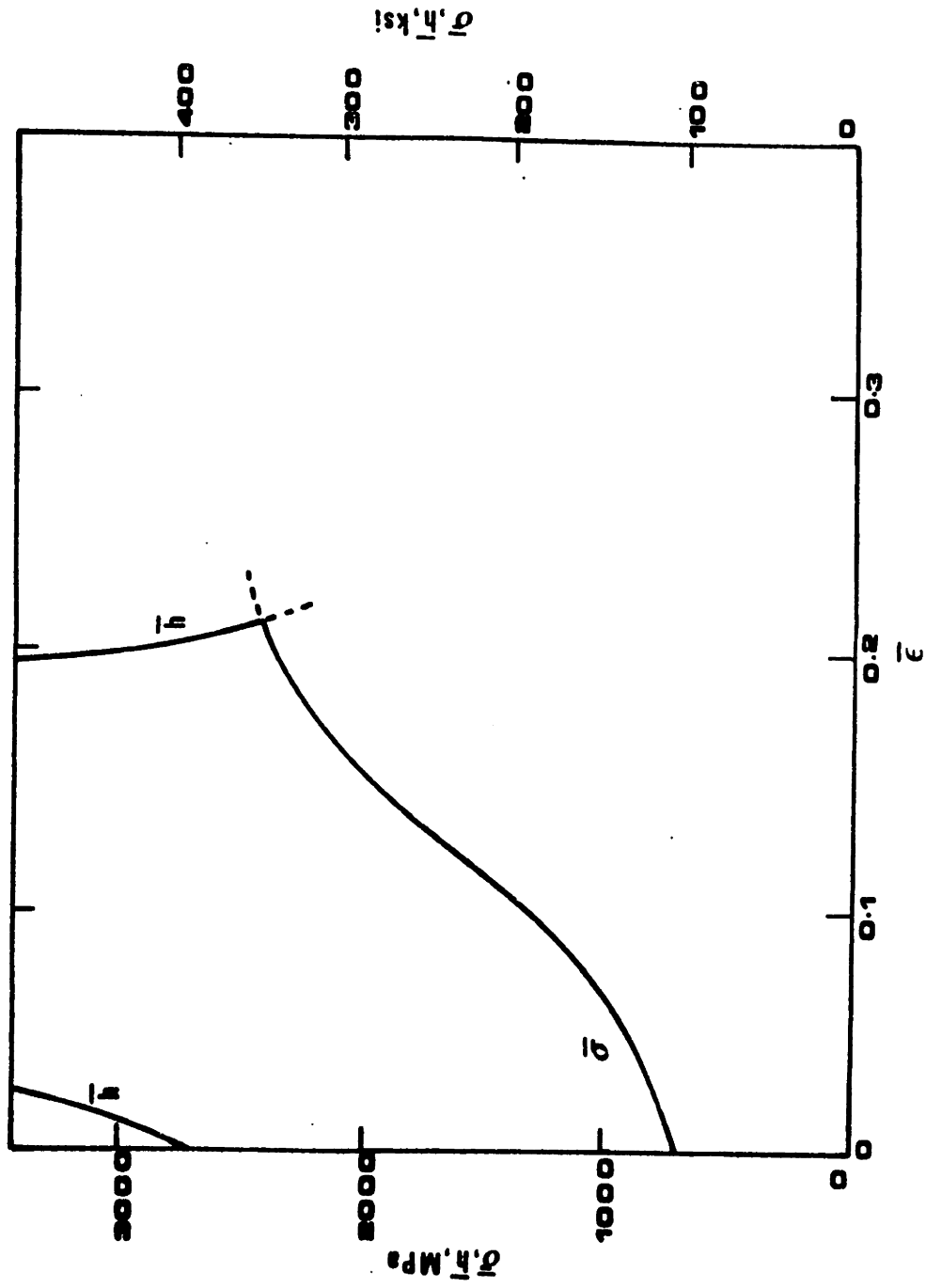


Figure 42 - True-stress and strain-hardening rate versus true-plastic-strain up to necking for 31Ni(L) tested at -75°C .

deformation and is larger than that observed at 25°C. This is due to the lower stability promoting a larger rate of transformation ($df/d\epsilon$) at early stages of deformation (see Equation 8). The large volume fraction of martensite present at these early stages of deformation is responsible for the early increase in both $\bar{\sigma}$ and \bar{h} with respect to plastic strain. However, the greater transformation rate at lower temperatures promotes early exhaustion of the transformation and this causes the necking instability to take place at lower plastic strains.

Similar behavior of the true-stress, true-plastic-strain curves is generally observed for 34Ni-9Co(H) and 26Ni-4Cr(H).

The decrease in uniform elongation due to the first mechanically-induced martensite formed can be rationalized in this same trend. Figure 43 shows the curves of $\bar{\sigma}$ versus $\bar{\epsilon}$ for 26Ni-4Cr(H) tested at 0°C ($\eta_u = 0$) and -55°C ($\eta_u = -0.37$). The decrease in ϵ_{pu} at -55°C can be accounted for by noting that the small dynamic softening at -55°C reduces \bar{h} in the vicinity of the normal necking strain. The necking condition $\bar{h} = \bar{\sigma}$ is then attained at lower values of plastic strain.

Similar extensive study of the influence of the mechanically-induced transformation on the shape of the $\bar{\sigma}$ versus $\bar{\epsilon}$ curves has been carried out for higher-strength nonprecipitation-hardenable TRIP steels^(5,17). Although a similar conclusion concerning the existence of an optimum evolution of the transformation was achieved, some differences in the behavior of both groups of alloys have been observed.

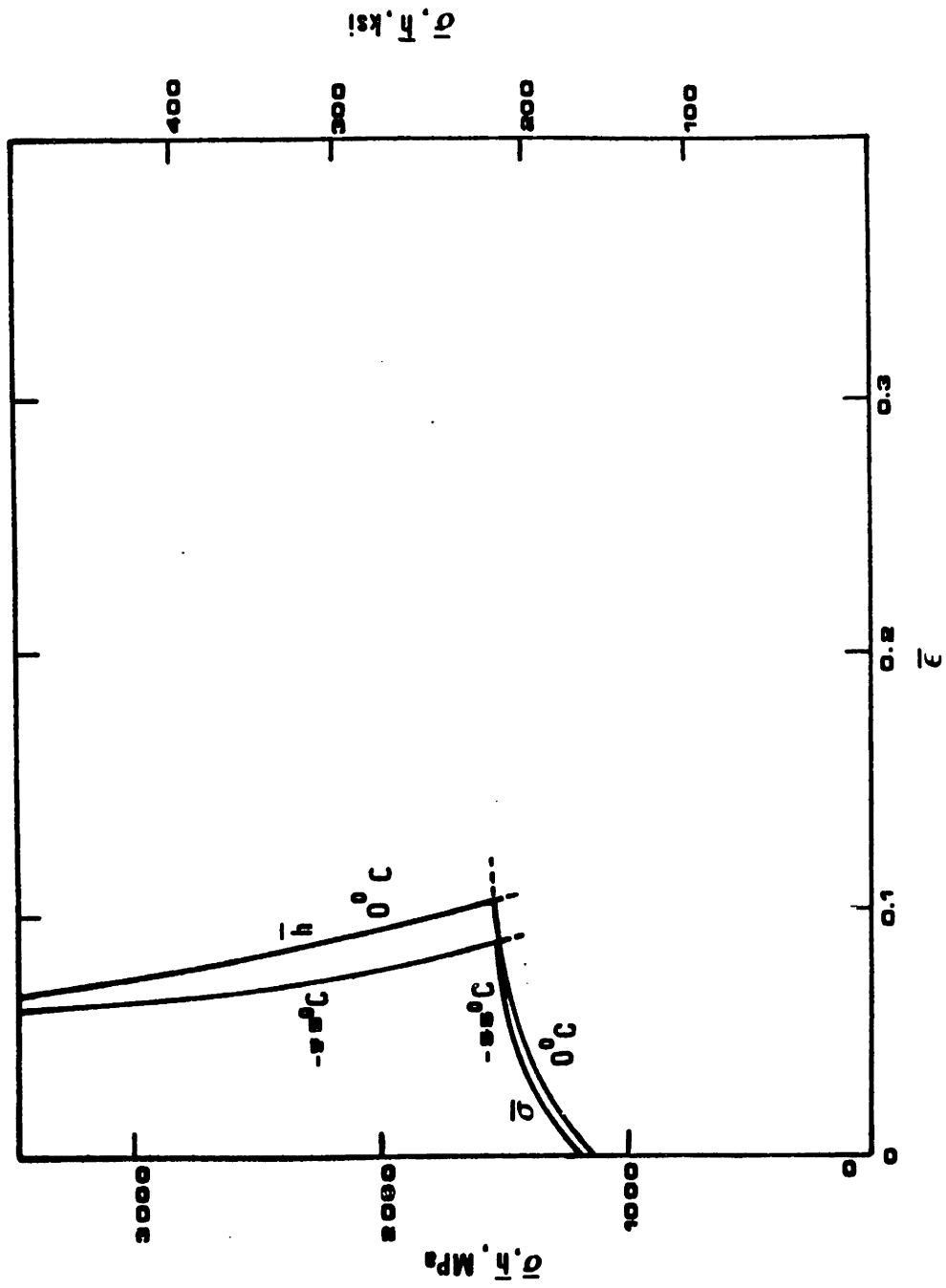


Figure 43 - True-stress and strain-hardening rate versus true-plastic-strain up to necking for 26Ni-4Cr(H) tested at 0°C and -55°C.

In the nonprecipitation-hardenable TRIP steels the onset of plastic straining at all temperatures is marked by the appearance of localized deformation in the form of Luder's bands. At temperatures where high values of uniform elongation are attained, the transformation is able to stabilize deformation after Luder's band propagation. This leads to a delay in the final necking instability. Much lower values of uniform elongation are attained at higher temperatures, where macroscopic uniform deformation is never reached. In the latter, the final necking starts before the Luder's band has spread throughout the whole gauge length of the tensile specimen.

In the precipitation-hardenable steels studied here, at all temperatures macroscopic uniform deformation is always present from the beginning of deformation through the final necking. Furthermore, while all $\bar{\sigma}$ versus $\bar{\epsilon}$ curves for the nonprecipitation-hardenable TRIP steels start with an upward curvature, in the alloys studied here this occurs only when a high dynamic softening is present.

5.4 - Shear-Instability-Controlled Fracture

As previously seen, the fracture of the alloys studied here over a fair range of temperatures occurred by shear instability. These instabilities, verified in both uniaxial tension and at the crack-tip, were triggered by localization of deformation. The enhancement in ϵ_f^n and J_{IC} due to mechanically-induced martensitic transformation can be analysed using the Rice formulation for the onset of localization of deformation⁽¹⁰⁸⁾.

The use of a continuum approach to analyse the zig-zag fracture observed in the alloys studied here seems to be reasonably appropriate. Each ridge in the zig-zag has a size on the order of 150 to 200 μm , and shows little size variation with temperature. Each ridge spans 2 to 4 grains, which are "pancaked" perpendicular to the macroscopic crack propagation plane due to the warm-rolling operation. Also, in most instances, the crack propagates continuously as shown in Figures 28 to 30.

Based on Rice's formulation, Needleman and Rice derived expressions for the critical requirements for the onset of localization of deformation⁽¹⁰⁹⁾. For a stress-controlled void-nucleation process and under plane-strain conditions, localization takes place at a critical value of $\bar{h}/\bar{\sigma}$ given by:

$$\left(\frac{\bar{h}}{\bar{\sigma}}\right)_{\text{crit}} = \frac{1}{1-K'\cosh\left(\frac{\sigma_m}{2\bar{\sigma}}\right)} \left[\frac{3f_v}{2} \cosh\left(\frac{\sigma_m}{2\bar{\sigma}}\right) \sinh\left(\frac{\sigma_m}{2\bar{\sigma}}\right) + \frac{(1+\nu)K'\bar{\sigma}}{6(1-\nu)} \cosh\left(\frac{\sigma_m}{2\bar{\sigma}}\right) \left\{ 1 + \frac{EK'\cosh\left(\frac{\sigma_m}{2\bar{\sigma}}\right)}{6} \right\} \right] \quad [26]$$

where \bar{h} is the effective strain-hardening rate ($\bar{h} = d\bar{\sigma}/d\bar{\epsilon}$), $\bar{\sigma}$ is the effective stress, σ_m is the mean (hydrostatic) stress, f_v is the void volume fraction, E and ν are Young's modulus and Poisson's ratio, and K' is a parameter related to the void-nucleation rate expressed as⁽¹⁰⁹⁾:

$$\left(\dot{f}_v\right)_{\text{nucl}} = K' \left(\dot{\bar{\sigma}} + \frac{\dot{\sigma}_m}{3} \right) \quad [27]$$

where the dot represents the time rate.

Equation 26 has been applied to uniaxial tension and plane-strain tension⁽¹¹⁰⁻¹¹³⁾. It seems reasonable to assume that the same concept applies to the crack tip, particularly considering that ahead of blunted cracks in hardening materials, stress and strain concentrations are smoothed out^(66,67). The smoothing of stresses and strains keeps them approximately constant over a distance equal to 2-4 times the blunted crack-tip opening^(66,67). If it is assumed that the fracture process occurs in this region, the assumptions behind Equation 26 can be satisfied. The main assumption in Rice's formalism is that the deformation in the

region of localization can be treated approximately as homogeneous. There are clear metallographic indications that the cracks present in the alloys studied here are blunted to a radius of 10 to 20 μm before they start to propagate.

Equation 26 was derived using Berg's porous-plastic model for ductile materials⁽¹⁰¹⁾ together with Gurson's constitutive equation for a cavitating material^(93,94). Consequently, in this development, it is assumed that in the region of shear localization voids should be present before the localization takes place. The large number of voids present outside the fracture plane in the materials studied here, e.g. Figures 19a and 44, suggests that the use of Equation 26 is appropriate.

Equation 26 predicts that localization of deformation is present whenever:

$$\left(\frac{\bar{h}}{\bar{\sigma}}\right) \leq \left(\frac{\bar{h}}{\bar{\sigma}}\right)_{\text{crit}} \quad [28]$$

The observed higher values overall strain to failure and J_{IC} for the lower-carbon alloys as compared to the higher-carbon ones when no transformation takes place may be related to differences in the values of f_v and K' . A higher-carbon content would undoubtedly mean the presence of more and/or larger void-forming carbides, implying larger f_v and K' and consequently higher $(\bar{h}/\bar{\sigma})_{\text{crit}}$ for the onset of shear localization; this leads to earlier fracture.



Figure 44 - Optical micrograph of the necked region of $^{31}\text{Ni}(\text{L})$ tested at 175°C .

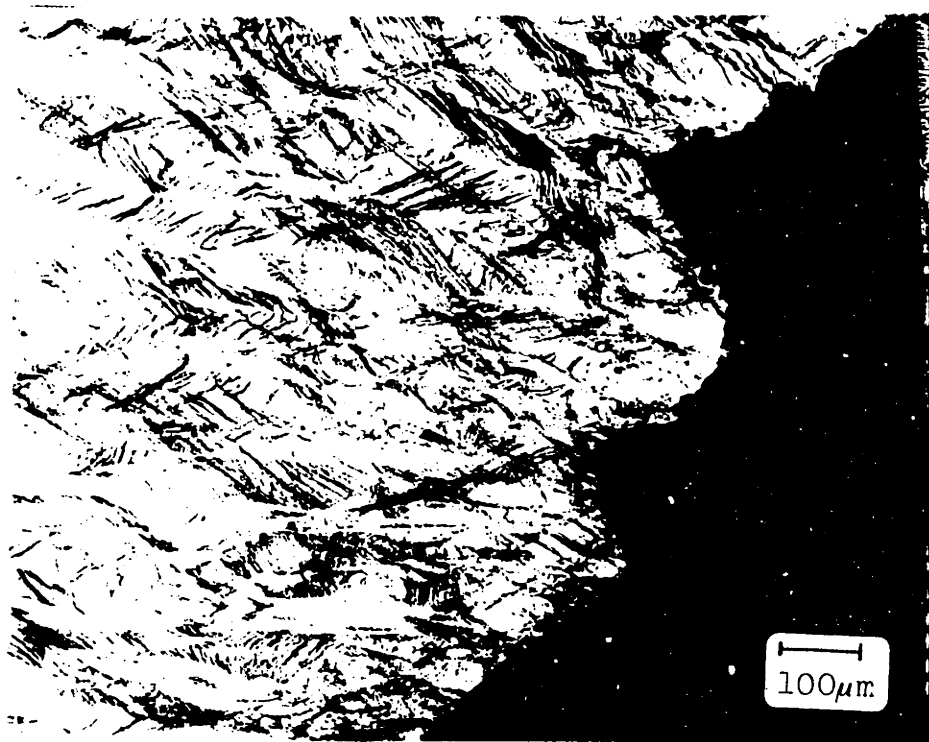
By analysing Equation 26, it is evident that mechanically-induced martensitic transformation can delay the onset of shear localization in two ways. The first is by maintaining high values of $\bar{h}/\bar{\sigma}$ at large strains, and the second is by reducing the local value of $\sigma_m/\bar{\sigma}$ due to the dilatation associated with the transformation.

The way in which the transformation affects the local $\bar{h}/\bar{\sigma}$ value is completely analogous to the way it affects $\bar{h}/\bar{\sigma}$ before necking, with the only difference being that the process now takes place at larger equivalent plastic strains. The analogy indicates that there should be a certain temperature in which the dynamic softening and the strain-hardening contributions of the transformation are combined in an optimum way. In this situation, $\bar{h}/\bar{\sigma}$ is kept at high values up to very large values of equivalent plastic strain.

Concerning the second way that the transformation can delay shear instability, it has been previously reported that positive dilatational strains decrease the local transverse stresses and consequently decreases σ_m ⁽¹²⁴⁾. The decrease in local triaxiality from dilation due to microcracking is responsible for the enhancement in J_{IC} in barre granite ⁽¹²⁴⁾. It is very likely that the same phenomenon exists in metastable austenitic steels where a dilatation occurs when transformation takes place. The local decrease in $\sigma_m/\bar{\sigma}$ due to the transformational dilatation exponentially decreases $(\bar{h}/\bar{\sigma})_{crit}$.

The beneficial effect of the transformational volume expansion on the enhancement in ductility and toughness in these alloys has already been indicated by the results shown in Figures 37 and 39. Further experimental evidence of the dilatation contributing to the increase in toughness is given by the comparison of the microstructures shown in Figure 45. In spite of the much larger amount of transformation in the necked region of 34Ni-9Co(H), Figure 45a, as compared to 26Ni-4Cr(H), Figure 45b, both at the same temperature, the values of ϵ_f^n as well as the increments compared to the pure austenite are approximately the same (see Tables V, VII and IX). The higher relative transformation volume change of 26Ni-4Cr(H) may thus give a higher toughening effect per amount of transformation, producing the same reduction in $\sigma_m/\bar{\sigma}$ as is observed for 34Ni-9Co(H) with a smaller amount of transformation. Similar observations have been made for the J_{IC} specimens of these two compositions tested at 150°C. Again, the higher volume expansion of 26Ni-4Cr(H) apparently compensates for the lower amount of transformation and the J_{IC} are the same (see Tables XIII and XIV).

Since the way mechanically-induced martensitic transformation affects $\bar{n}/\bar{\sigma}$ predicts the existence of an optimum stability condition, the same must be true for the overall delay in attaining the critical condition for shear localization and fracture, given by Equation 27. Inasmuch as it is the localization of deformation that leads to the



(a)



(b)

Figure 45 - Optical micrograph of the necked region of (a) 34Ni-9Co(H) and (b) 26Ni-4Cr(H) tested at 130°C.

final fracture, an optimum transformation stability condition must also exist for the overall enhancement in J_{Ic} and ϵ_f^n . The situation is then similar to the previously analysed influence of the transformation on the uniform elongation but with the additional features just discussed. While for the onset of necking the critical condition is fixed ($\bar{h}/\bar{\sigma} = 1$), in the shear instability the critical condition varies with the amount of transformation and transformational dilatation. As previously discussed, this variation is due to the influence of the transformation on the local value of $\sigma_m/\bar{\sigma}$. The variable critical condition for the onset of shear instability as compared to necking can account for the larger spread in stability over the range where ϵ_f^n and $\Delta J_{Ic}/J_{Ic}(\text{aust})$ are increasing as compared to the sharper variation in $\Delta \epsilon_{pu}/\epsilon_{pu}(\text{aust})$ (compare Figures 35, 37 and 39).

Comparing Figures 37 and 39, within the temperature interval of the tensile tests run in this work, in contrast to the behavior of $\Delta J_{Ic}/J_{Ic}(\text{aust})$, no apparent drop in $\Delta \epsilon_f^n$ has been observed at $T \lesssim M_d(n)$. This suggests that the drop either occurs much closer to M_d than in the J_{Ic} case, or it may be suppressed. A possible explanation for the less noticeable drop is that, at $T \lesssim M_d$, the orders of magnitude larger transformation zones in the necked region, as compared to the crack-tip, may be responsible for a decrease in triaxiality even when very little amount of transformation is present. The importance of the transformation zone size in reducing triaxiality and enhancing toughness has been

indicated in Hutchinson's model for ceramic systems⁽⁴⁸⁾, and will be also present in a semi-quantitative model developed in section 5.5. In terms of Equation 26, a large transformation zone, even with a small amount of martensite in it, may produce a noticeable decrease in triaxiality, and consequently a decrease in $(\bar{h}/\bar{\sigma})_{\text{crit}}$. This may compensate for the decrease in the local $\bar{h}/\bar{\sigma}$ due to the dynamic softening produced by the small amount of transformation. The larger transformation zones in the necked region, coupled with the intrinsically lower triaxiality as compared to the crack-tip, may also be responsible for the larger maximum relative enhancement in the strain to failure, $(\Delta \epsilon_f^n / \epsilon_f^n(\text{aust}))_{\text{max}} \approx 2.0$, as opposed to J_{IC} , $(\Delta J_{\text{IC}} / J_{\text{IC}}(\text{aust}))_{\text{max}} \approx 0.6$.

Another feature that sets in much more often at large plastic strains is the possibility that a different fracture process, like cleavage, intergranular, or low-ductility dimple fracture may produce premature failure and prevent the attainment of the highest possible toughness. When this happens, failure occurs at values of plastic strain less than that required for the onset of shear instability. As pointed out in the last chapter, there are indications that this happens in the alloys studied here when the failure occurs in a fully martensitic region. This type of premature failure is, in fact, a frequent phenomenon, and as indicated by the failure of 26Ni-Cr(H) tensile tested at -196°C , it can occur even at the low strains present before necking.

The tendency for the Fe-Ni-Ti martensites to show cleavage, intergranular, or a low-ductility flat dimple fracture mode can be rationalized by the analysis of how the γ' precipitates are affected by the martensitic transformation. It has been reported (125,126) that when very short aging times are used, the very small γ' clusters coherent with the austenitic matrix maintain coherency with the martensitic product phase during the martensitic transformation. This gives rise to a tetragonal distortion of martensite, similar to that present in high-carbon steels. This internal stress may explain the small amount of cleavage observed in 31Ni(T). On the other hand, when longer aging times are used, larger coherent γ' precipitates are formed which resist coherency loss during the transformation. Although these precipitates ultimately lose coherency with the martensite, they introduce stresses and strains in the martensite due to the resistance to the coherency loss (123,125,126). This internally stressed martensite is expected to be more brittle and so may account for the low-ductility void process as well as for the intergranular fracture sometimes observed. The intergranular fracture occurs along prior austenitic grain boundaries, even when the grains are completely transformed to martensite.

Figures 37 and 39 clearly indicate that the change in failure mode and consequent maxima in $\Delta \epsilon_f^n$ and $\Delta J_{IC}/J_{IC}(\text{aust})$ occurs respectively around $M_S^\sigma(n)$ and $M_S^\sigma(\text{ct})$ for all metastable alloys. This suggests that in the alloys studied here premature failure is more prone to occur in

stress-assisted plate martensite as opposed to strain-induced lath martensite. The higher brittleness of plate martensite has been previously observed⁽¹²⁷⁾, and may prevent the attainment of the highest possible neck ductility, and fracture toughness in the alloys here considered

5.5 - The Role of The Volume Change

Evidence for the beneficial effect of the transformational expansion on the enhancement of toughness in triaxial stress-states is given in Figures 37 and 39. An analysis of the way the volume expansion would delay the fracture by shear instability is given in the previous section. Here, a semiquantitative model for the relative enhancement in fracture toughness is developed in which the important role of the volume change is again evident.

Figure 46 shows the variation of the relative fracture toughness enhancement, $\Delta J_{IC}/J_{IC}(\text{aust})$, with the half-height of the transformation zone, d , which is the size of the transformation zone above (or below) the plane of crack propagation. In this development, for all alloys, consideration is limited to the range of temperatures in which enhancement in the fracture toughness due to the transformation is observed.

Figure 46 suggests that in some cases for the same d , very different enhancements can be obtained. For instance, for $d \approx 25 \mu\text{m}$, a larger amount of martensite in the transformation zone apparently produces a larger relative enhancement in J_{IC} . This suggests that the relevant parameter in the analysis should include the amount of martensite in the transformation zone, as well as d .

Figure 47 shows the dependence of $\Delta J_{IC}/J_{IC}(\text{aust})$ on $\bar{f}d$, where \bar{f} is the mean volume fraction of martensite over d ; $\bar{f}d$ is then a measure of the total amount of martensite in

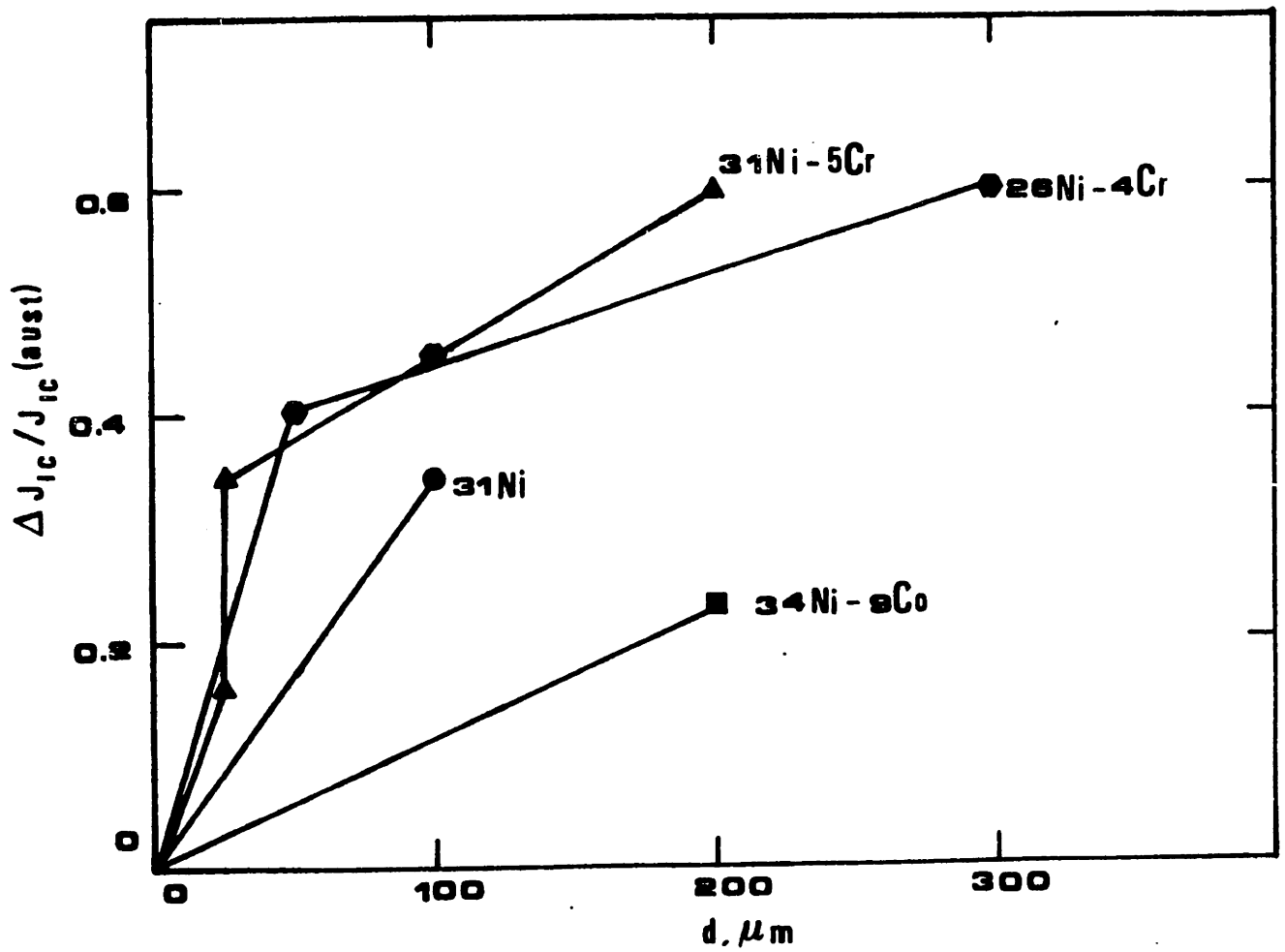


Figure 46 - J_{IC} relative enhancement versus transformation zone half-height.

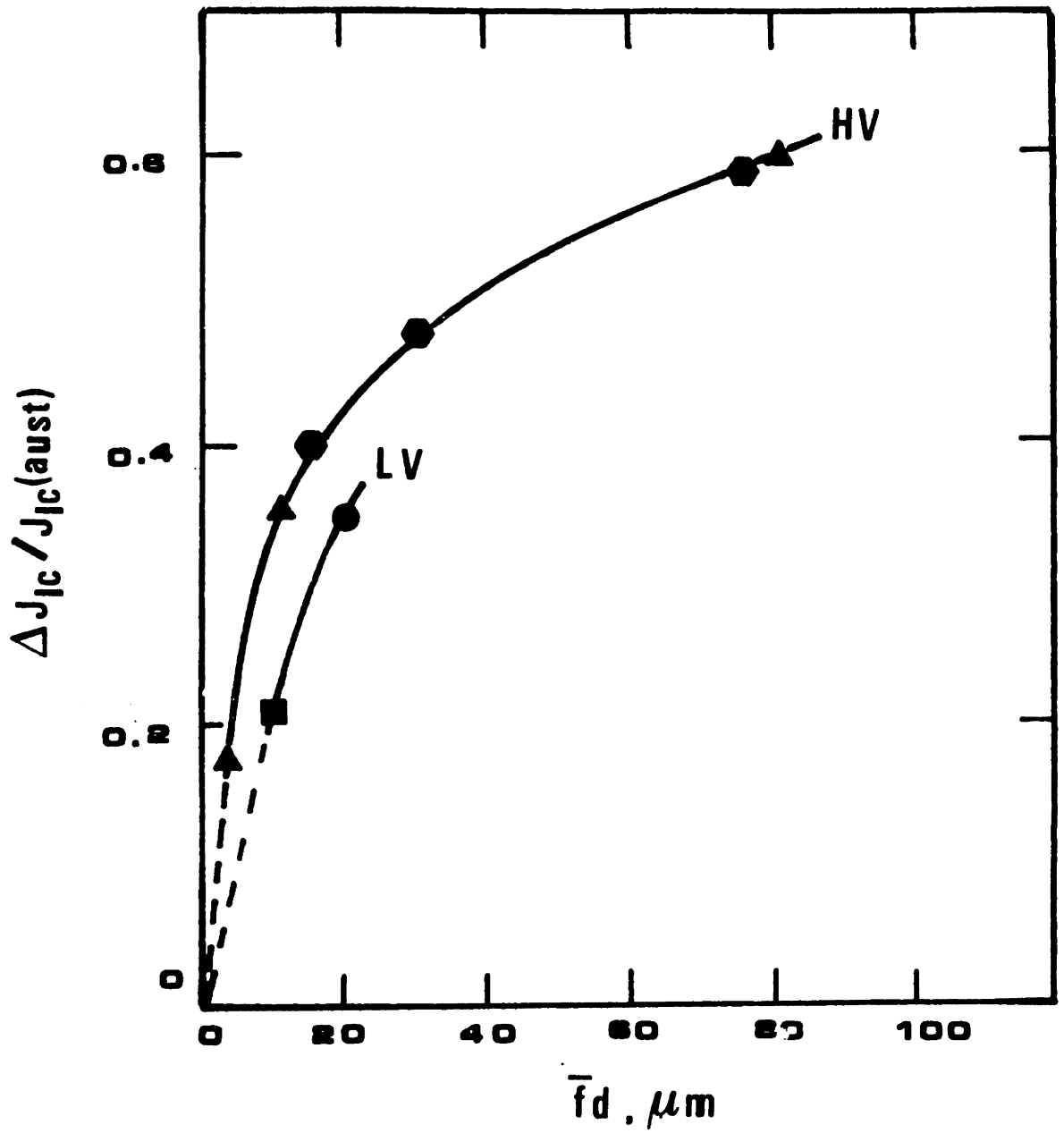


Figure 47 - J_{IC} relative enhancement versus amount of martensite in the transformation zone.

the transformation zone. The data in Figure 47 suggest a difference in the level of $\Delta J_{Ic}/J_{Ic}(\text{aust})$ for the same \bar{f}_d according to the volume expansion of the transformation. Furthermore, the results suggest a relation between $\Delta J_{Ic}/J_{Ic}(\text{aust})$ and \bar{f}_d of the type:

$$\frac{\Delta J_{Ic}}{J_{Ic}(\text{aust})} = k \left(\frac{\Delta v}{v} \right) (\bar{f}_d)^\alpha \quad [29]$$

Based on the results for the high volume-change alloys, $\alpha \approx 1/3$. Assuming that α is not dependent on the transformation volume expansion, $k(\Delta v/v)$ can be obtained from Figure 48. Based on this figure, assuming a linear dependence of k on $\Delta v/v$, the final expression for the relative increment in J_{Ic} due to the transformation is:

$$\frac{\Delta J_{Ic}}{J_{Ic}(\text{aust})} = \left(0.0544 + 2.3469 \frac{\Delta v}{v} \right) (\bar{f}_d)^{1/3} \quad [30]$$

With respect to the dependence of $\Delta J_{Ic}/J_{Ic}(\text{aust})$ on the parameter η defined in Equation 25, the data in Figure 39 suggest a linear dependence for $\eta < 0$, and a clear distinction between the high- and low-volume alloys. By considering the results for $\eta < 0$ where no premature failure occurs, the linear fitting of the data gives:

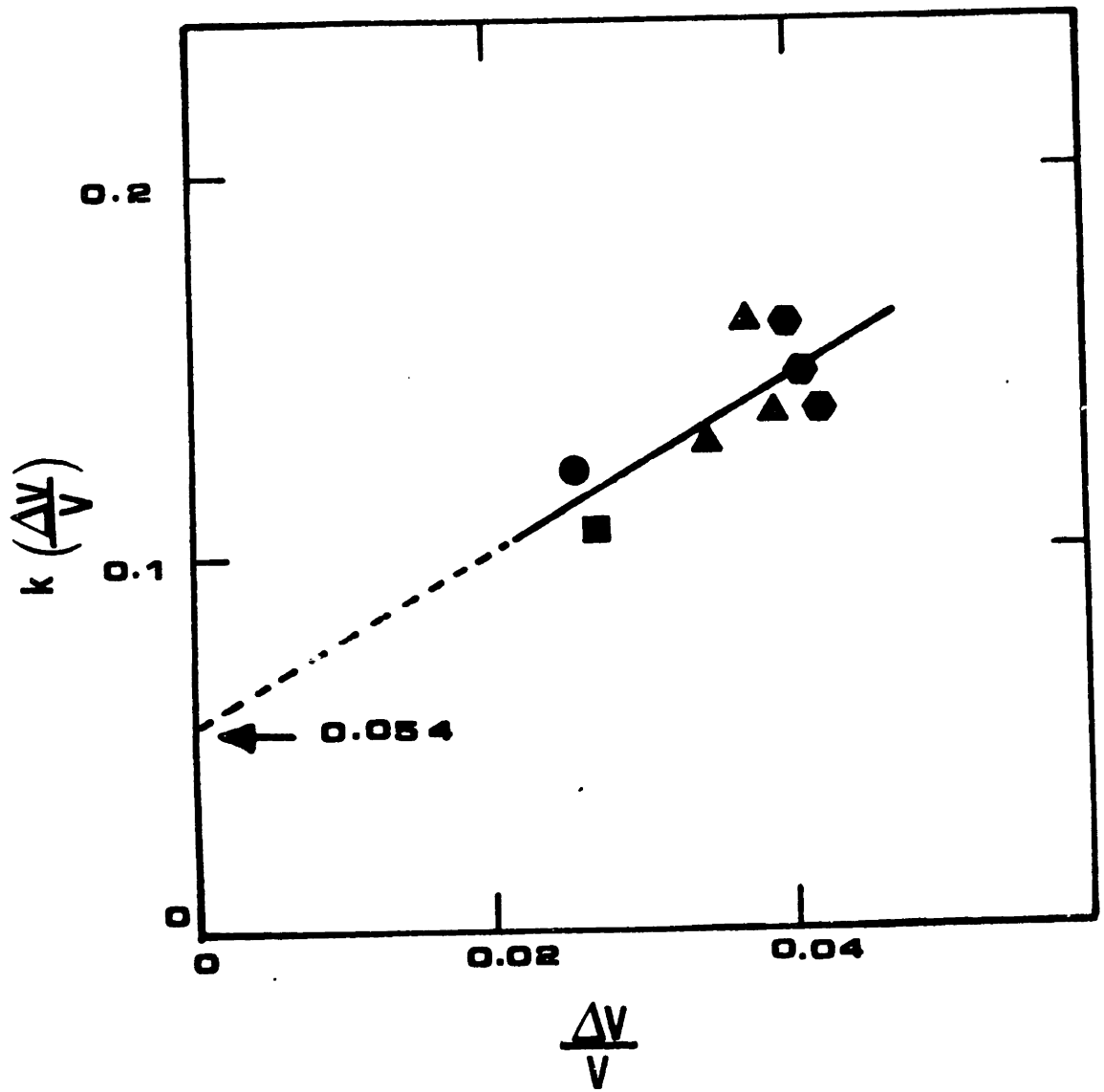


Figure 48 - $k(\frac{\Delta V}{V})$ versus relative transformational volume change.

$$\frac{\Delta J_{Ic}}{J_{Ic}(\text{aust})} = -0.2915 - 0.8213\eta \quad (\text{high } \Delta V/V) \quad [31]$$

$$\frac{\Delta J_{Ic}}{J_{Ic}(\text{aust})} = -0.5573 - 0.8314\eta \quad (\text{low } \Delta V/V)$$

The expressions indicate that the slope of the lines is virtually independent of $\Delta V/V$. On the other hand, $\Delta V/V$ has an influence on the value of η for which $\Delta J_{Ic}/J_{Ic}(\text{aust}) = 0$. The dependence of $\Delta J_{Ic}/J_{Ic}(\text{aust})$ can thus be expressed as:

$$\frac{\Delta J_{Ic}}{J_{Ic}(\text{aust})} = k'(\Delta V/V) - 0.8264\eta \quad [32]$$

where the slope is taken as an average between the ones obtained for the two group of alloys. Assuming a linear dependence of $k'(\Delta V/V)$ on $\Delta V/V$:

$$\frac{\Delta J_{Ic}}{J_{Ic}(\text{aust})} = -1.06 + 18.99 \frac{\Delta V}{V} - 0.8264\eta \quad [33]$$

This expression shows clearly that for alloys with lower $\Delta V/V$ to have the same $\Delta J_{Ic}/J_{Ic}(\text{aust})$ as the alloys with higher $\Delta V/V$, a lower transformation stability (smaller η or larger $|\eta|$) is required. In other words, alloys with lower transformational volume change require more martensitic

transformation to compensate for it. This seems to be also true for the increment in strain to failure, as has been previously discussed in connection with Figure 45.

The expressions in Equations 30 and 33 show that toughening is dependent on $\Delta V/V$, but dilatation is not essential, in agreement with the model proposed in section 5.4.

The enhancement in toughness in metastable austenitic alloys that fail by shear instability can be rationalized through the analysis of the effect of mechanically-induced martensitic transformation on the flow behavior of these materials. Under triaxial stress-states the transformational volume expansion is also important.

Figure 49 shows schematically how the relative increment in uniform elongation, the absolute increment in the strain to failure, and the relative increment in fracture toughness vary with the normalized temperature interval defined by Equation 25. By considering the effect of the transformation on the flow behavior of these materials, the drop in ductility and toughness at $T \lesssim M_d$ and also the peaks in the solid lines can be predicted. Since no noticeable drop in $\Delta \epsilon_f^n$ has been observed in this work, the curve for this parameter in Figure 49 is shown as a dotted line at $T \lesssim M_d(n)$. The possibility of a reduced or even suppressed drop has been discussed in section 5.4.

Figure 50 summarizes schematically how the true-stress, true-plastic-strain curves are altered by the transformation. By comparison with the curve at $T > M_d$, the very first amount of transformation present at $T \lesssim M_d$ produces a flattening of the $\bar{\sigma}$ versus $\bar{\epsilon}$ curve, causing the critical condition $\bar{\eta}/\bar{\sigma} = (\bar{\eta}/\bar{\sigma})_{crit}$ to be reached at lower plastic strain. By further lowering the temperature, the

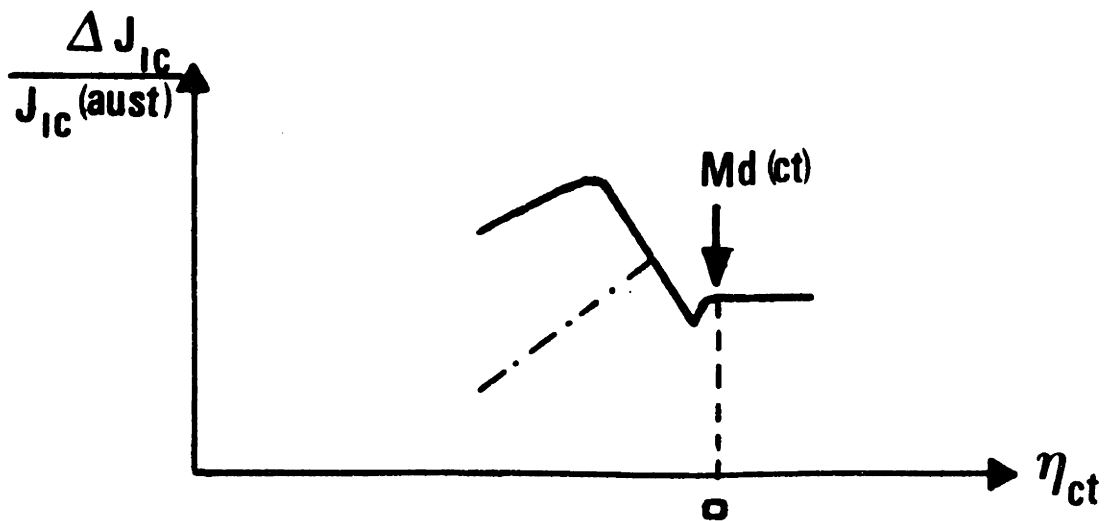
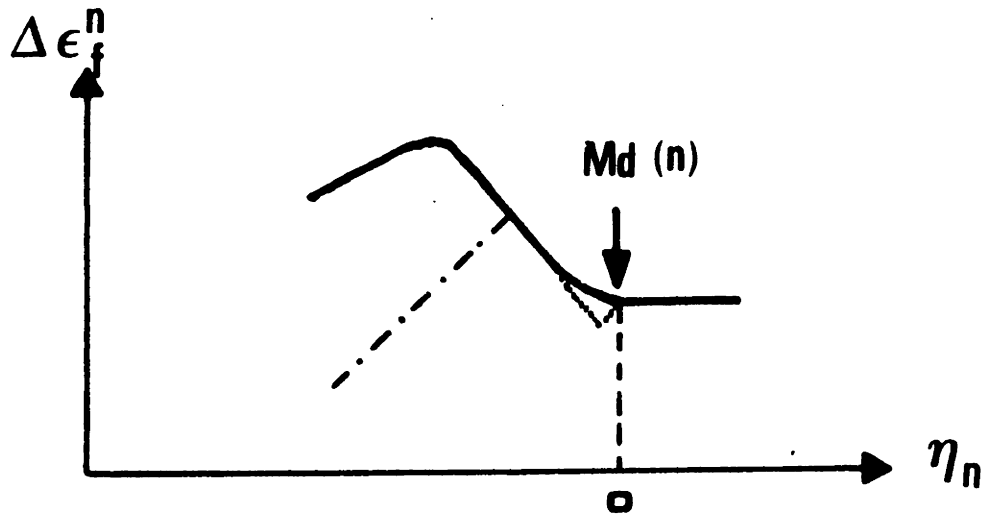
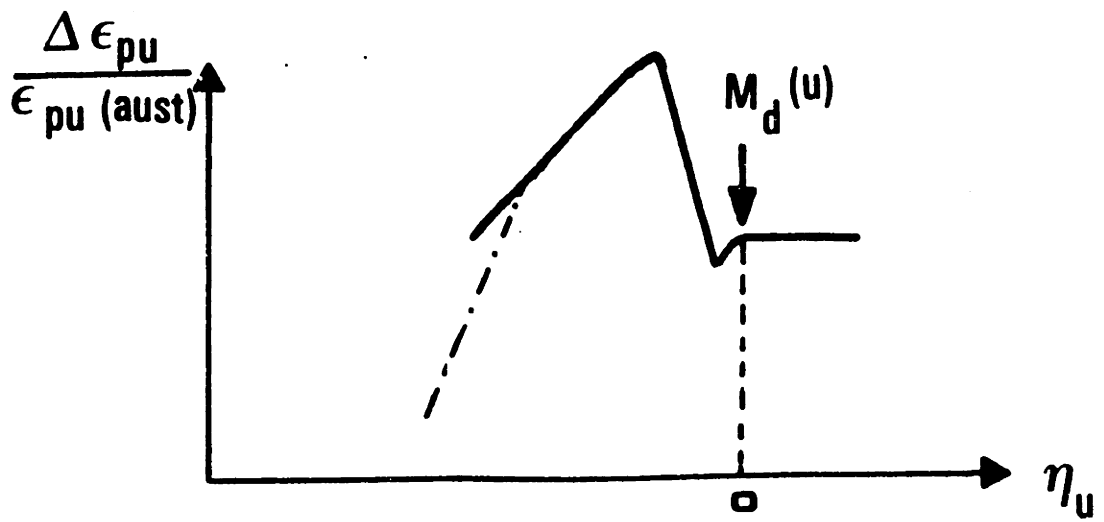


Figure 49 - Schematic uniform elongation relative enhancement, strain to failure absolute enhancement, and J_{IC} relative enhancement versus normalized temperature.

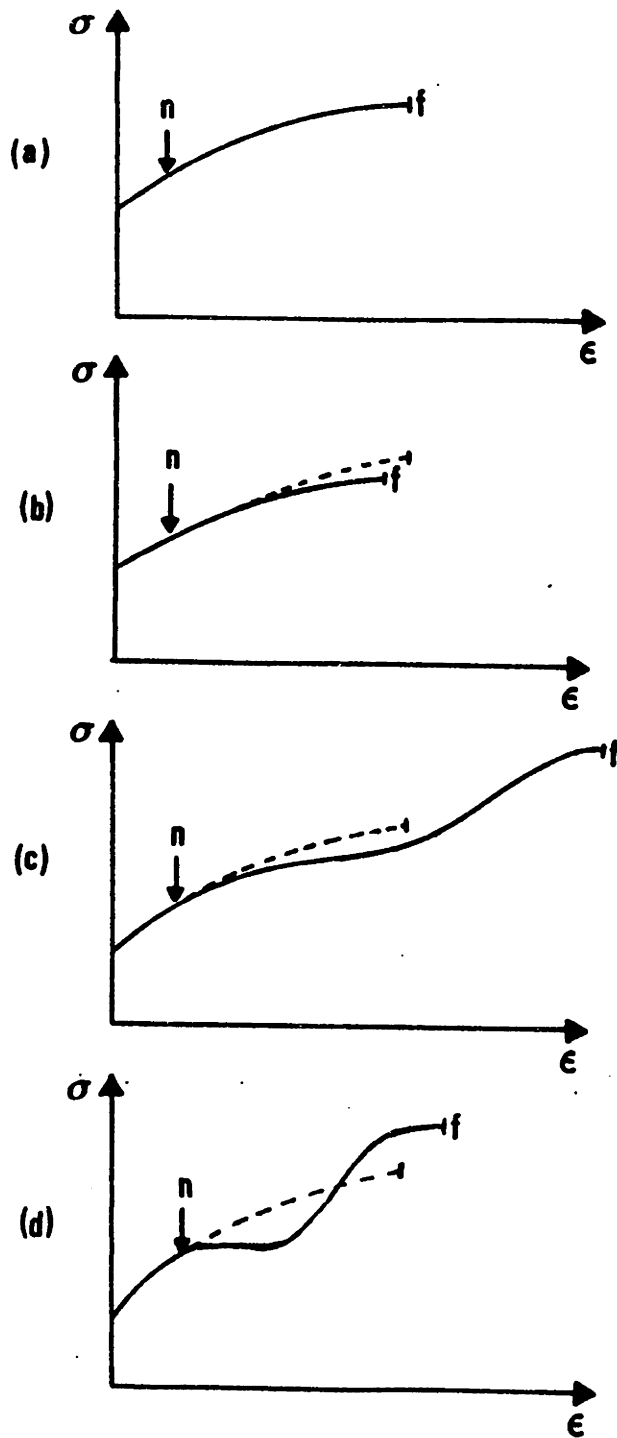


Figure 50 - Schematic true-stress, true-plastic-strain curves at (a) $T_1 > M_d$, (b) $T_2 \leq M_d$, (c) T_3 when maximum in toughness is attained, (d) $T_4 < T_3$.

dynamic softening and the work-hardening contributions of the transformation are combined in an efficient way to delay the attainment of the critical instability condition. Only considering the effect of transformation, a maximum in toughness would be obtained at $T = T_3$. At still lower temperatures the material becomes excessively metastable and a large amount of transformation sets in at relatively lower values of plastic strain compared to those at which the fracture occurs.

The shape of the stress-strain curves when mechanically-induced martensitic transformation occurs indicates that there may be up to two changes in curvature before final fracture. The first is promoted by the static hardening contribution of the transformation and takes place just after the end of the dynamic softening. In this case the curvature changes to upward. The second change in curvature occurs when the transformation is exhausted, and takes place at larger plastic strains. The curvature changes from upward to the final downward. It is expected that for the temperature of the highest ductility increment, the strain to failure of the pure austenite, in the case of maximum ϵ_f^n , or the strain for the onset of necking, in the case of maximum ϵ_{pu} , would fall in between the plastic strains corresponding to the two changes in curvature. This is schematically shown in Figure 51, where the maximum in uniform elongation and strain to failure would occur respectively in the temperature ranges ΔT_1 and ΔT_2 . The extremes of these temperature

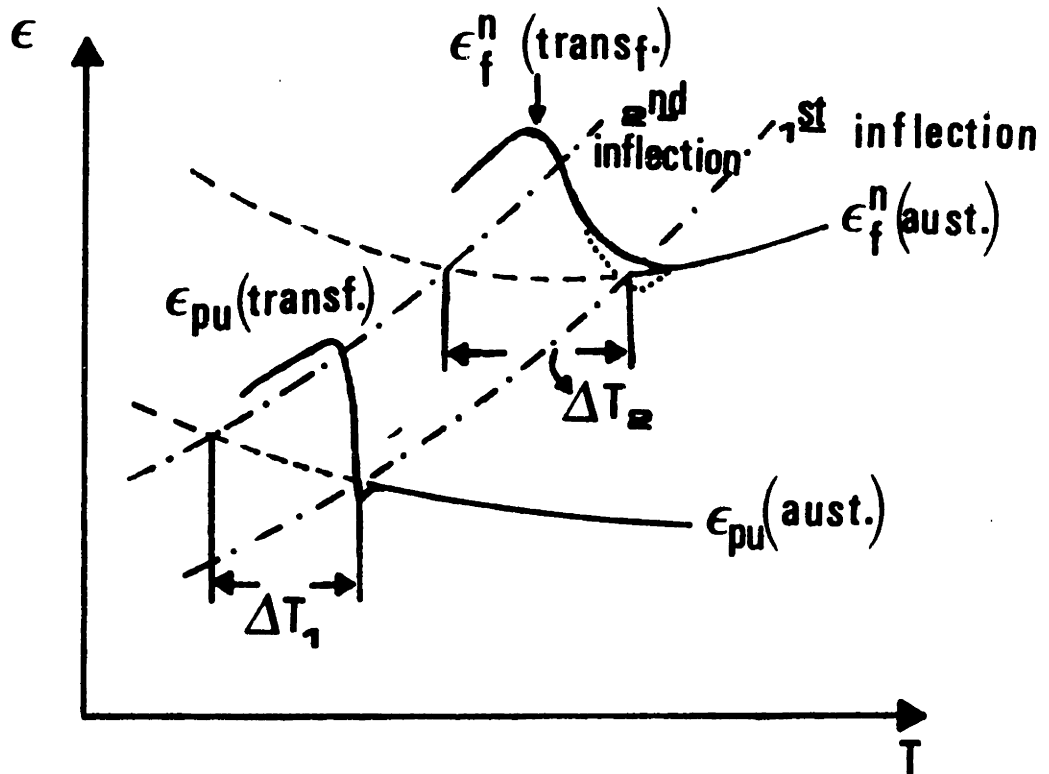


Figure 51 - Schematic temperature dependence of plastic strain. It shows the dependences of stable austenite strain to failure and strain for the onset of necking, the dependences of the strain corresponding to the two inflections in the curves σ versus ϵ promoted by mechanically-induced transformation, and also the increase in ϵ_f and ϵ_{pu} due to the transformation. The maximum in ϵ_{pu} and ϵ_f are observed respectively in the temperature intervals ΔT_1 and ΔT_2 .

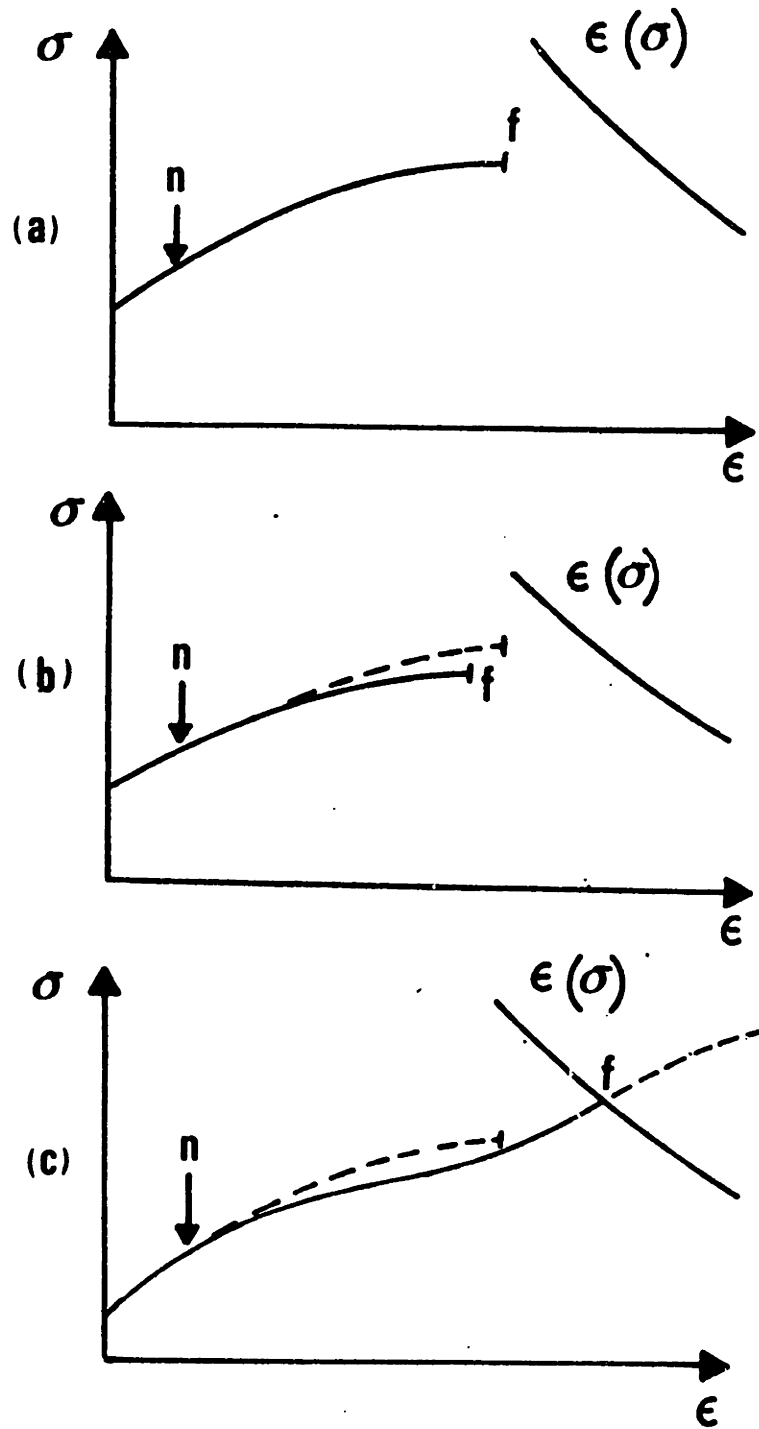


Figure 52 - Schematic true-stress, true-plastic-strain curves for different temperatures showing possible premature failure by other fracture process described by $\epsilon_f(\sigma)$: (a) $T_1^i > M_d$, (b) $T_2^i < M_d$, (c) T_3^i when premature failure prevails.

intervals are given by the intersection of the stable austenite strain for the onset of necking and strain to failure, respectively, with the strains corresponding to the two inflections in the $\bar{\sigma}$ versus $\bar{\epsilon}$ curves. The temperatures for the maxima may be predicted using theoretical transformation curves and constitutive equations already derived^(32,34). For the strain to failure case, it would also be necessary to model quantitatively the dependence of $(\bar{h}/\bar{\sigma})_{crit}$ on the transformation dilatation. These developments are listed in the suggestions for future work, Chapter VII.

In practice, the intrinsic maximum in toughness due only to the influence of the transformation in the flow behavior may never be attained; other fracture processes may produce failure before the critical condition for flow localization is reached. This possibility is schematically shown in Figure 52, where the general curve $\epsilon_f(\sigma)$ represents the required strain to produce failure by mechanisms other than shear instability. The real $\epsilon_f(\sigma)$ will depend on the specific fracture process (cleavage, intergranular, dimples, etc...). Its value will vary with the relative amount of each phase, austenite and martensite, present at the fracture zone, and also with the intrinsic toughness of the different martensitic morphologies (plate versus lath). The possibility that the attainment of maximum toughness and ductility can actually be prevented due to premature failure by other fracture mechanism is indicated in Figure 49.

This formalism is applicable for toughness and ductility as measured by J_{Ic} , strain to failure, and uniform elongation. The basic difference between the first two cases and the uniform elongation is that in a triaxial state $(\bar{h}/\bar{\sigma})_{crit}$ is a function of triaxiality and its value is affected by the transformation dilatation. Since the critical condition for the onset of necking is fixed at $(\bar{h}/\bar{\sigma})_{crit} = 1$, sharper temperature variations are expected for ϵ_{pu} as compared to ϵ_f^n and J_{Ic} .

A beneficial effect of the transformation has been also observed in the resistance to crack growth as measured by $dJ/d\Delta a$. Although the temperature dependence of this parameter suggests once more the existence of an optimum transformation stability condition for maximum crack-growth resistance, a more detailed analysis is complicated by the fact that the crack propagates in a combined Mode I-Mode II type of loading.

5.7 - Comparison with Commercial Steels

Figure 53 compares maximum fracture toughness values obtained in this work (31Ni-5Cr(L) tested at -75°C) with results for other high-toughness commercial alloys of the same yield strength. The data for the other alloys represent tests at room temperature. Figure 53 indicates that mechanically-induced martensitic transformation is able to produce materials of very good toughness ($K_{IC} \approx 255 \text{ MPa}\sqrt{\text{m}} \approx 230 \text{ ksi}\sqrt{\text{in}}$ at a yield strength of 1300 MPa)

The main problem with commercial utilization of these metastable austenitic steels is the strong temperature dependence of the mechanically-induced martensitic transformation. The results obtained here indicate that although sharp variation in uniform elongation with test temperature is observed, the changes in strain to failure and in fracture toughness are smoother. The temperature dependence of these two latter properties is affected by the transformational volume expansion and also by the difference between M_d and M_s^{σ} for the respective stress-state. The addition of Cr tends to promote the desired effect of increasing the temperature range between M_d and M_s^{σ} and it also produces a larger transformational volume change. This is expected from a reduction of both the stacking-fault energy and $\Delta S^{\gamma \rightarrow \alpha}$.

The results also indicate that for the alloys studied here, concerning fracture toughness, the best working condition is to design an alloy with $M_s^{\sigma}(\text{ct})$ slightly lower

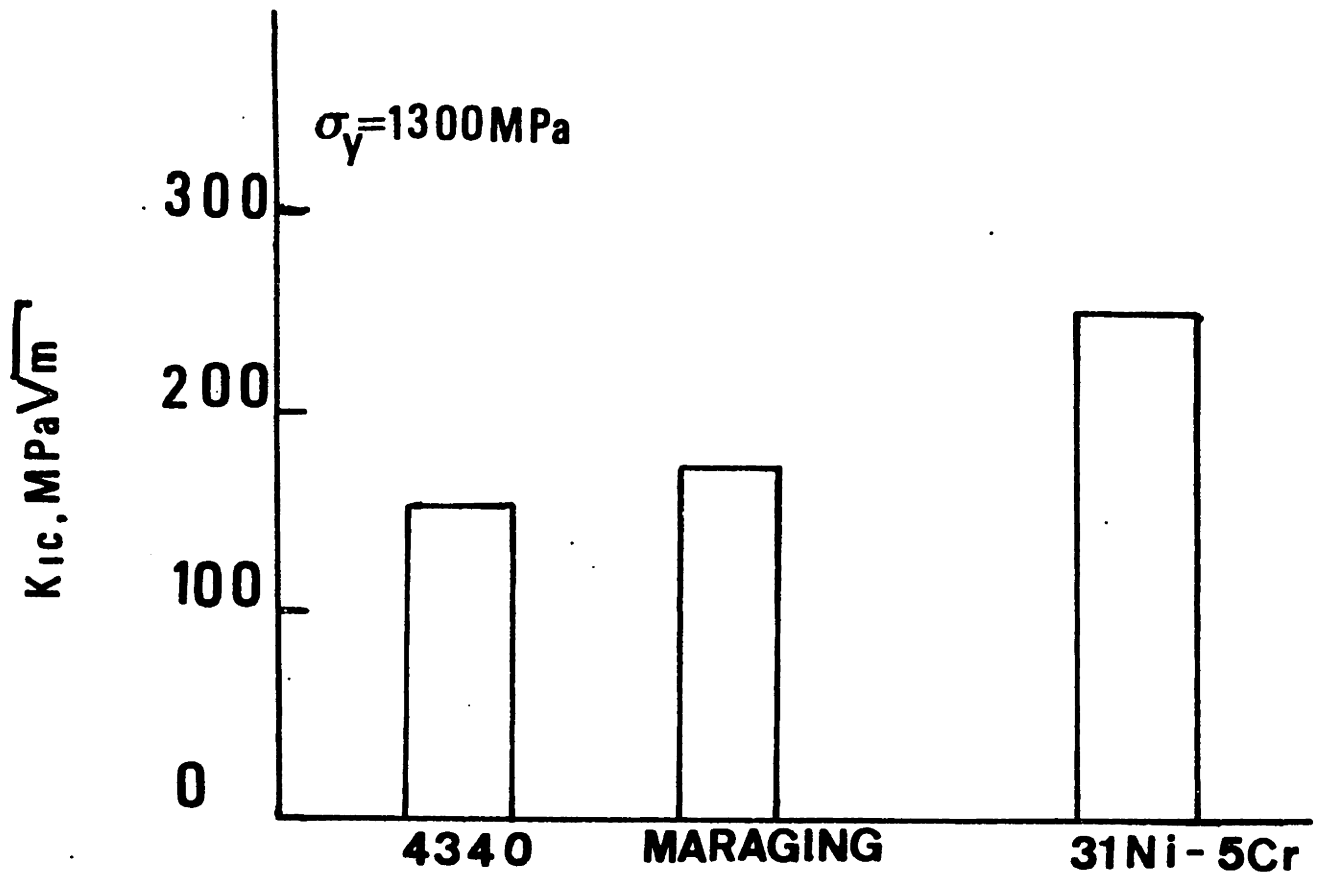


Figure 53 - Comparison of fracture toughness of the alloys studied here and commercial steels. Data for 4340 and maraging steels taken from Reference 97.

than the working temperature, since the maximum in toughness occurs at $M_s^{\sigma}(ct)$. Also, larger amounts of carbon in solution may be beneficial for relative enhancements in ductility and toughness by promoting a harder martensite and consequently larger work-hardening rates.

CHAPTER VI : CONCLUSIONS

1. The predicted variation in the stability of stress-assisted martensitic transformation as a function of stress-state has been verified experimentally. Although the expected increase in M_S^c with increased triaxiality occurs, no corresponding change in M_d is observed. This is attributed to the lower strains attainable in plane-strain failure.
2. At $T = M_S^c$ ahead of the crack-tip, the size of the transformation zone is about equal to the calculated austenitic plastic zone ahead of the crack-tip. The heights of the transformation zones are much smaller than the heights of plastic zones, consistent with the lower triaxiality above and below the crack-tip.
3. The present work has shown that mechanically-induced martensitic transformation enhances the ductility and toughness of metastable austenitic steels which fail by shear instability. By defining a normalized temperature interval $\eta = (T - M_d)/(M_S^c - M_d)$, it is shown that the increments in uniform elongation, strain to failure in the neck, and fracture toughness follow the same general pattern. The only additional feature present in the strain to failure and fracture toughness is that, under a triaxial stress-state, the transformational volume change influences the ductility and toughness increments. Metastable alloys

with larger transformational volume expansions have higher triaxial ductility and toughness at the same transformation stability. Furthermore, this volume expansion also promotes a larger range of transformation stabilities over which the enhancement in strain to failure and J_{Ic} takes place as compared to uniform elongation.

4. The enhancement in uniform elongation is explained by an analysis of how mechanically-induced transformation affects the flow behavior of metastable austenitic steels. The transformation delays the onset of necking by keeping the ratio $\bar{h}/\bar{\sigma}$ greater than 1 up to larger plastic strains. The analysis is able to account for the drop in ϵ_{pu} noted at temperatures just below $M_d(u)$, and it suggests the existence of an optimum stability condition for which the enhancement in toughness is maximum.
5. By using a model ($\bar{h}/\bar{\sigma} \ll \text{critical } \bar{h}/\bar{\sigma}$) for the onset of shear localization under plane strain conditions it is possible to rationalize the enhancement in the strain to failure and fracture toughness. The transformation increases toughness in plane strain by two different mechanisms. The first, similar to the uniform elongation case, is by keeping the ratio $\bar{h}/\bar{\sigma}$ at high values up to large equivalent plastic strains. The second is by favorably lowering the critical $\bar{h}/\bar{\sigma}$ for shear localization via a reduction in triaxiality promoted by the transformational volume expansion. By considering both

mechanisms, it has been possible to explain all the features observed in the temperature dependence of ϵ_f^n and J_{IC} . The model predicts the existence of an optimum transformation stability condition for which the ductility and toughness enhancement is maximum. In practice, this maximum may not be attained due to premature failure by other lower-toughness fracture processes. In the alloys studied here the maxima in ϵ_f^n and J_{IC} occur around M_s for the respective stress-state, probably due to intrinsic brittleness of stress-assisted martensite that contributes to premature failure at $T < M_s^{\sigma}$.

6. A semiquantitative model for the relative enhancement in fracture toughness due to mechanically-induced transformation has been developed, which indicates that the toughness increment is dependent on the volume expansion, but the latter is not essential. This model predicts a contribution of the volume expansion which is a function not only of the relative expansion but also of the size of the transformation zone and the amount of martensite in it. An expression for the dependence of the relative enhancement of fracture toughness on η has also been developed. In this expression is again evident the importance of the transformational volume change.
7. In a sense the mechanism of fracture-toughness enhancement observed for the alloys studied here differs from that previously reported for high-strength TRIP steels and

ceramic systems. While in the latter cases the toughness comes from a shielding of the crack-tip from the applied stresses, in materials that fail by shear instability the enhancement is obtained by a direct influence of the transformation on the fracture process itself.

8. A comparison between the maximum fracture toughness obtained in this work ($K_{IC} \cong 255 \text{ MPa}\sqrt{\text{m}}$) with that reported for other high-toughness commercial steels indicates that mechanically-induced martensitic transformation is a very effective toughening mechanism, but extremely sensitive to the compositional and test conditions. The addition of Cr to metastable austenitic steels is beneficial for smoothing out the generally sharp temperature variation in mechanical properties; Cr also increase the transformational volume expansion.

CHAPTER VII : SUGGESTIONS FOR FUTURE WORK

Experimentally, the effect of different strain-hardening rates on the toughness of metastable austenitic steels can be verified by comparing the results reported in this work with those found for much higher-carbon steels. By proper designing, it should be possible to obtain stable and metastable precipitation-hardenable austenitic alloys with similar strength but with higher-carbon contents that generate stronger martensites and larger strain-hardening rates.

The effect of strain rate can be verified by running impact pre-cracked Charpy tests. Possible notch-geometry effects can be studied by comparing the results shown here with those obtained for slow-bend Charpy tests. Notch-geometry effects at high strain rates can be studied by comparing regular and pre-cracked impact Charpy test results. Stress-state effects can be further investigated with plane-strain tensile tests.

Analytically, the experimental true-stress, true-plastic strain curves can be modeled using theoretical transformation curves and constitutive equations for metastable austenitic steels. The optimum stability condition for maximum uniform elongation can be then predicted. This can be done directly for the curves up to necking, and also after necking if proper correction for the triaxial stress-state is

applied. In the necking case, it will be desirable to model the way that the transformational volume change alters the local triaxiality. Furthermore, it may be possible to simulate numerically the crack-growth process in these materials using finite-element methods and applying the material's constitutive equations.

APPENDIX

J Versus Δa Curves

Figures A1 to A5 show the curves of J versus Δa for the alloys studied here. The error bars indicate a 50% confidence interval. From these data, Tables X to XIV from the main text were constructed.

Side-Grooved Specimen Testing

As mentioned in section 3.4, a side-grooved 31Ni-5Cr(L) specimen was tested at -75°C in order to assure that the high values of J_{IC} measured were not a consequence of deviation from plane-strain conditions. The 31Ni-5Cr(L) tested at -75°C was selected because it exhibited the highest toughness measured in this work. The 20% side-grooving produced a flat fatigue pre-crack as well as a flat crack propagation under monotonic loading. Figure A2 indicates that the J value measured for the side-grooved specimen (in parentheses) was only 8% lower than that obtained for the usual specimen loaded to the same crack length and at the same temperature (-75°C). Since this difference should even be smaller for less tough conditions, the J_{IC} results reported here are believed to be meaningful plane-strain J_{IC} values.

Influence of Overaging

In an attempt to study the possibility of avoiding the detrimental effect of the γ' precipitates on the fracture properties of mechanically-induced martensite, a J_{IC}

experimental determination was carried out on overaged 31Ni-5Cr(L) at -25°C . By overaging, it was expected that noncoherent γ' precipitates would be formed and the martensite would be less strained. However, as shown by the results in Figure A2, the expected toughness enhancement did not occur. Actually, fractographic analysis indicated that intergranular fracture occurred to some extent.

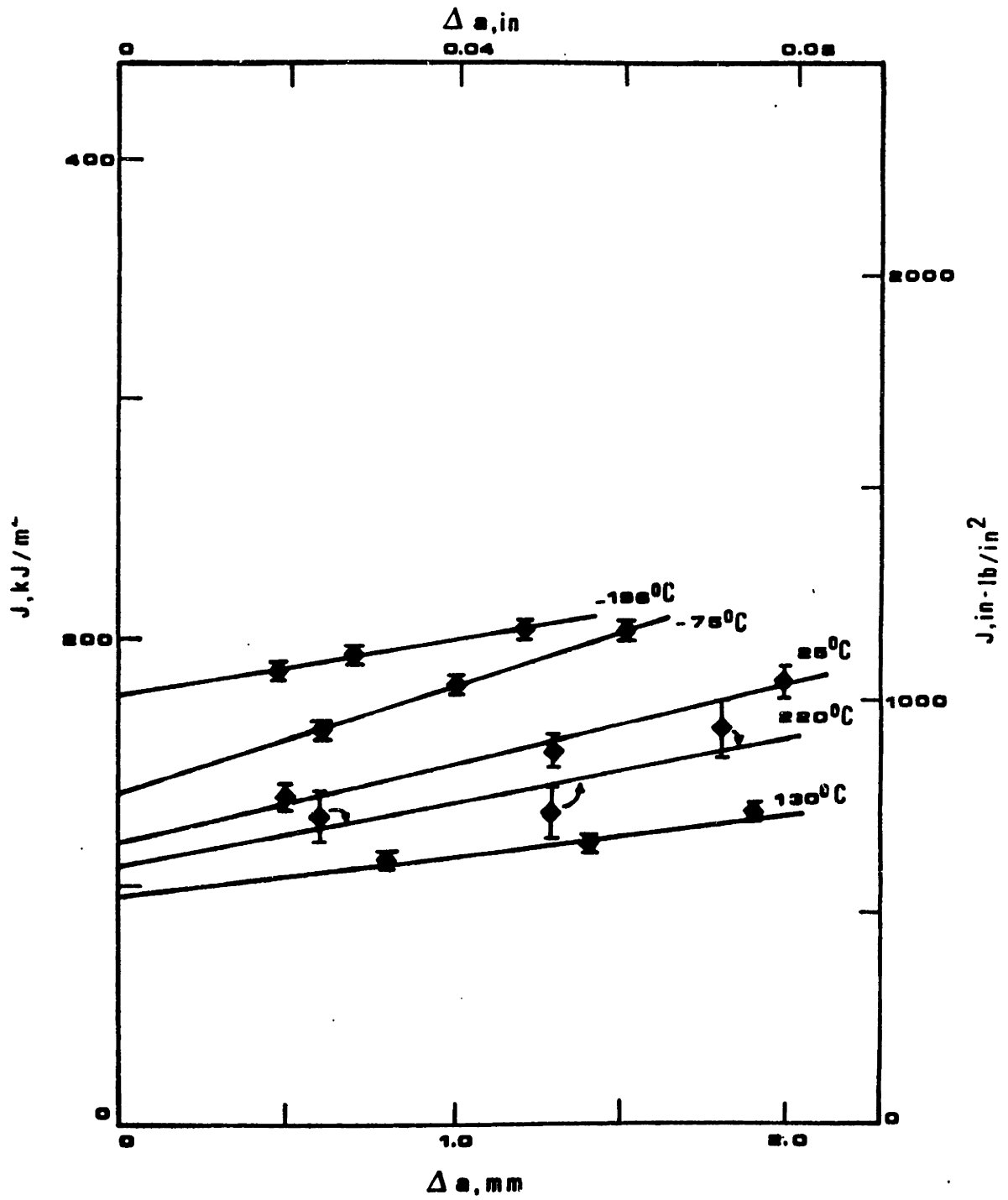


Figure A1 - J versus Δa curves for 36Ni-4Cr(H)

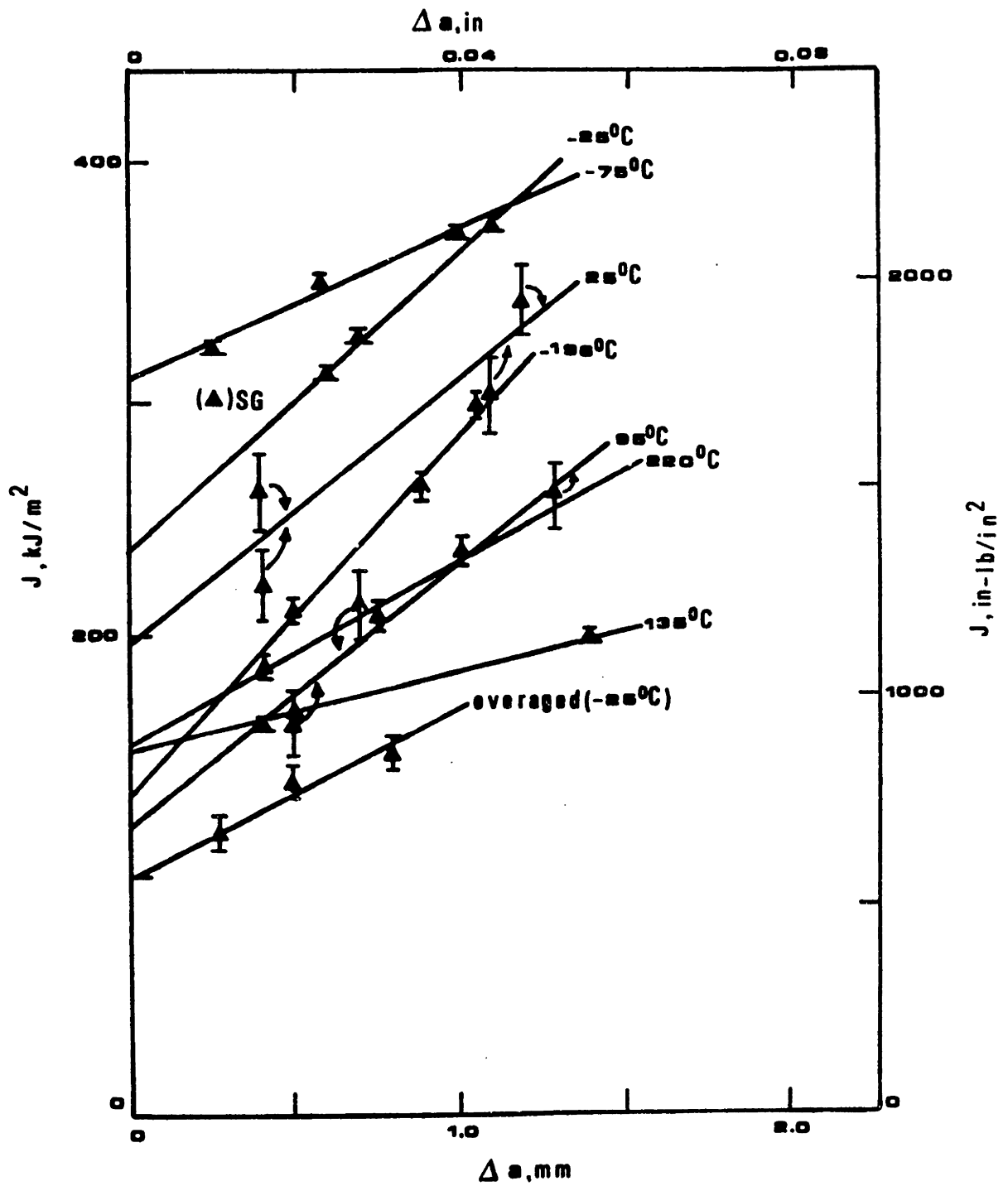


Figure A2 - J versus Δa curves for 31Ni-5Cr(L)

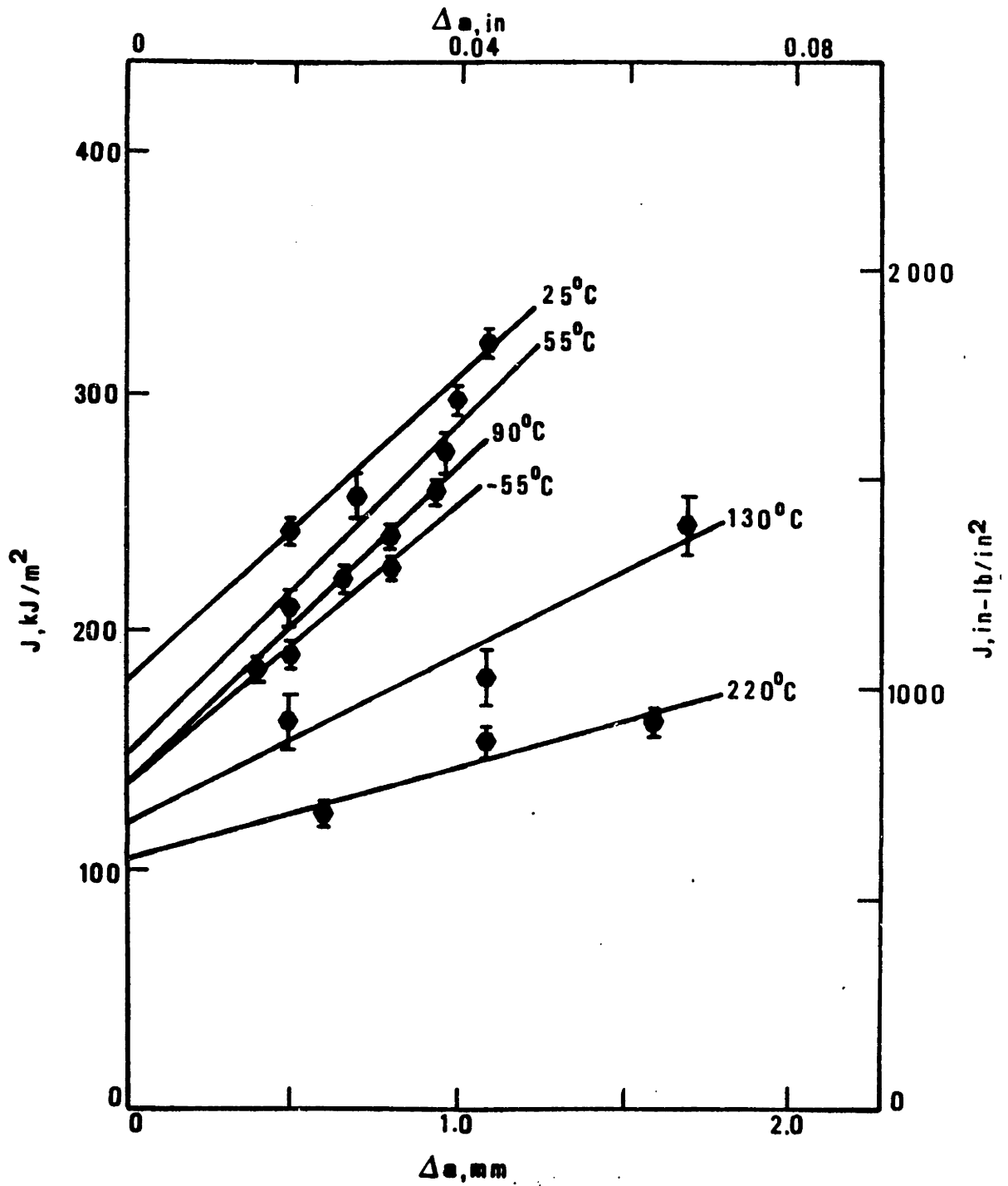


Figure A3 - J versus Δa curves for 26Ni-4Cr(H)

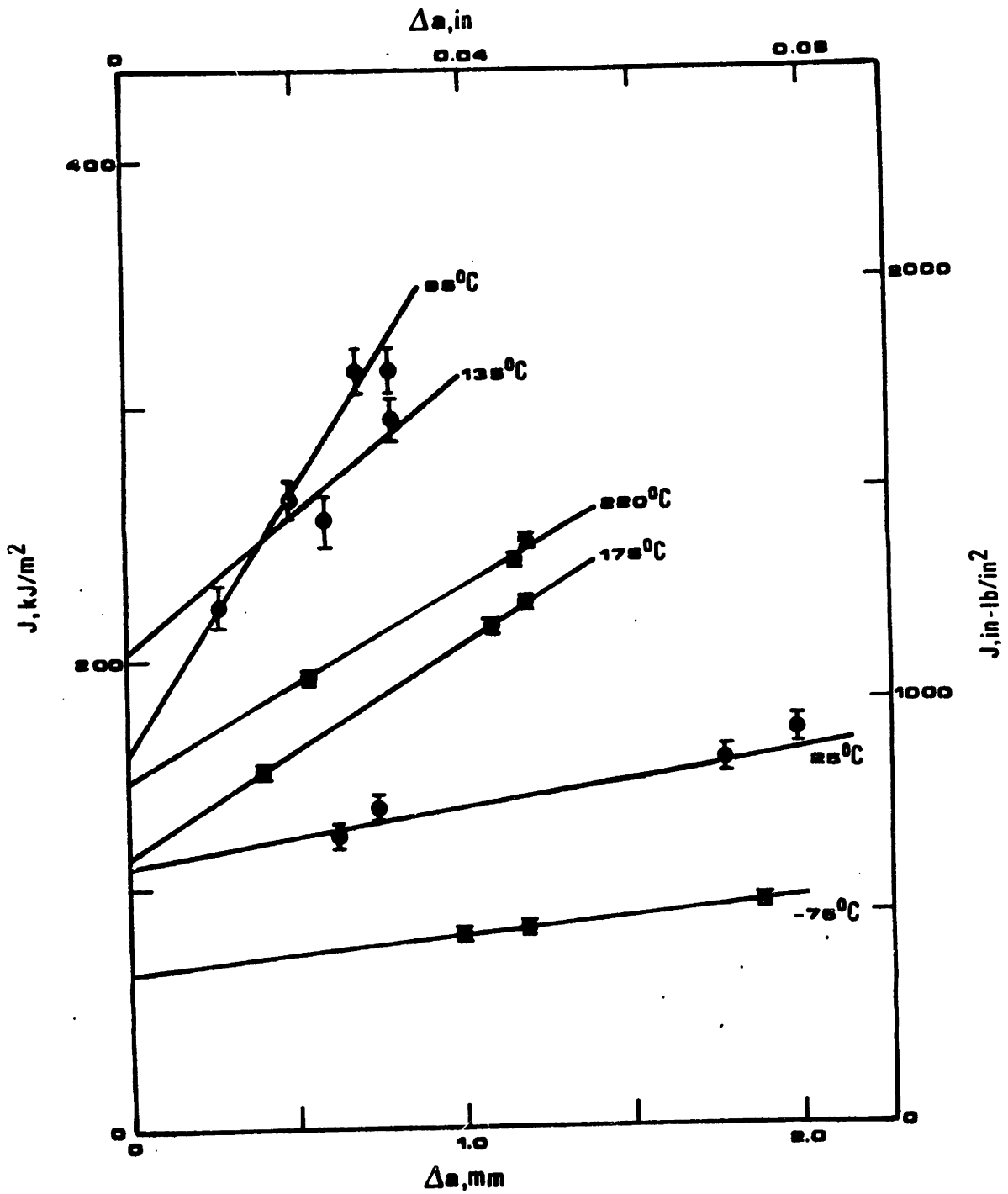


Figure A4 - J versus Δa curves for 31Ni(L)

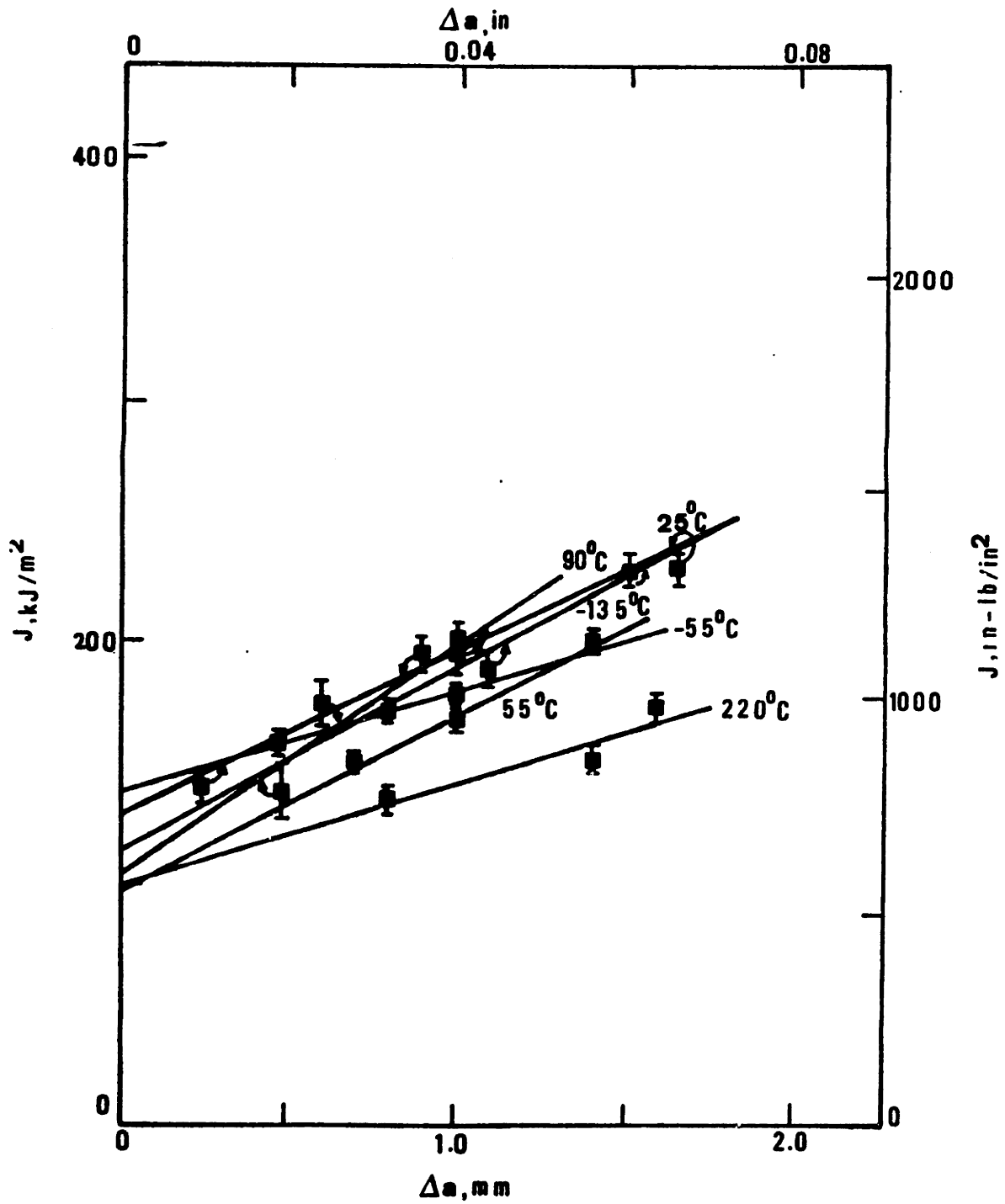


Figure A5 - J versus Δa curves for 34Ni-9Co(H)

BIBLIOGRAPHY

- (1) E.Scheil, "Uber die Umwandlung des Austenites in Martensit in Eisen-Nickellegierungen unter Belastung", Z.Anorg.Allg.Chem.207, 1932, p.21
- (2) J.R.Patel and M.Cohen, "Criterion for the Action of Applied Stress in the Martensitic Transformation", Acta Met.1, 1953, p.531
- (3) G.B.Clson and M.Cohen, "A Mechanism for the Strain-Induced Nucleation of Martensitic Transformations", J. Less-Comm. Metals 28, 1972, p.107
- (4) R.H.Richman and G.F.Bolling, "Stress, Deformation and Martensitic Transformation", Met. Trans. 2, 1971, p.2451
- (5) G.B.Olson, "Transformation Plasticity and the Stability of Plastic Flow", presented at 1982 ASM Materials Science Seminar: Deformation, Processing and Structure
- (6) J.P.Bressanelli and A.Moskowitz, "Effects of Strain Rate, Temperature and Composition on Tensile Properties of Metastable Austenitic Stainless Steels", ASM Trans. Quart. 59, 1966, p.223
- (7) V.F.Zackay, E.R.Parker, D.Fahr and R.Busch, "The Enhancement of Ductility in High-Strength Steels", Trans. ASM 60, 1967, p.252
- (8) W.W.Gerberich, P.L.Hemmings, M.D.Merz and V.F.Zackay, "Preliminary Toughness Results on TRIP Steel", ASM Trans. Quart. 61, 1968, p.843
- (9) W.W.Gerberich, P.L.Hemmings, V.F.Zackay and E.R.Parker, "Interactions Between Crack-Growth and Strain-Induced Transformation", Fracture, Chapman and Hall Ltd., London 1969, p.288
- (10) S.D.Antolovich and B.Singh, "On the Toughness Increment Associated with the Austenite to Martensite Phase Transformation in TRIP Steels", Met. Trans. 2, 1971, p.2135
- (11) G.B.Clson and M.Azrin, "Transformation Behavior of TRIP Steels", Met. Trans. 9A, 1978, p.713
- (12) J.A.Hall, V.F.Zackay and E.R.Parker, "Structural Observations in a Metastable Austenitic Steel", Trans. ASM 62, 1969, p.965

- (13) W.W.Gerberich, G.Thomas, E.R.Parker and V.F.Zackay, "Metastable Austenites: Decomposition and Strength", Proc. 2nd. Int. Conf. on the Strength of Metals and Alloys, 1970, p.894
- (14) G.R.Chanani, V.F.Zackay and E.R.Parker, "Tensile Properties of 0.05 to 0.20 Pct.CTRIP Steels", Met. Trans. 2, 1971, p.133
- (15) D.Fahr, "Stress- and Strain-Induced Formation of Martensite and its Effects on Strength and Ductility of Metastable Austenitic Stainless Steels", Met. Trans. 2, 1971, p.1883
- (16) D.Bhandarkar, V.F.Zackay and E.R.Parker, "Stability and Mechanical Properties of Some Metastable Austenitic Steels", Met. Trans. 3, 1972, p.2619
- (17) M.Azrin, G.B.Olson and R.A.Gagne, "Warm Extrusion of TRIP Steels: Process Control and Tensile Properties", Mater. Sci. Eng. 23, 1976, p.33
- (18) S.D.Antolovich, "Fracture Toughness and Strain-Induced Phase Transformations", Trans. TMS-AIME 242, 1968, p.2371
- (19) W.W.Gerberich, P.L.Hemmings and V.F.Zackay, "Observations of Strain-Induced Martensite Around a Crack", Trans. TMS-AIME 245, 1969, p.1124
- (20) S.D.Antolovich and B.Singh, "Observations of Martensite Formation and Fracture in TRIP Steels", Met. Trans. 1, 1970, p.3463
- (21) J.P.Birat and W.W.Gerberich, "A Metastable Austenite with Plane-Stress Fracture Toughness Near 500,000 psi in" Int. J. Fract. Mech. 7, 1971, p.108
- (22) W.W.Gerberich, P.L.Hemmings and V.F.Zackay, "Fracture and Fractography of Metastable Austenites", Met. Trans. 3, 1972, p.2661
- (24) G.R.Chanani and S.D.Antolovich, "Low-Cycle Fatigue of a High-Strength Metastable Austenitic Steel", Met. Trans. 5, 1974, p.217
- (25) A.G.Pineau and R.M.Pelloux, "Influence of Strain-Induced Martensitic Transformations on Fatigue Crack Growth Rates in Stainless Steels", Met. Trans. 5, 1974, p.1103
- (26) D.Hennessy, G.Steckel and C.Altstetter, "Phase Transformation of Stainless Steel During Fatigue", Met. Trans. 7A, 1976, p.415

- (27) G. Baudry and A. Pineau, "Influence of Strain-Induced Martensitic Transformation on the Low-Cycle Fatigue Behavior of a Stainless Steel", Met. Trans. 5, 1974, p.1103
- (28) R.G. Luther and T.R.G. Williams, "The Influence of Phase Transformation in Stainless Steel During Static and Fatigue Loading", Metal Sci. 11, 1977, p.219
- (29) G.B. Olson, R. Chait, M. Azrin and R.A. Gagne, "Fatigue Strength of TRIP Steels", Met. Trans. 11A, 1980, p.1069
- (30) G.B. Olson and M. Cohen, "Stress-Assisted Isothermal Martensitic Transformation and Transformation Plasticity", Proc. of US/Japan Seminar on Mechanical Properties of Martensite, R.P.I., 1979, p.7
- (31) D.L. Porter and A.H. Heuer, "Mechanisms of Toughening Partially Stabilized Zirconia (PSZ)", J. Amer. Ceram. Soc. 60, 1977, p.183
- (32) T. Narutani, G.B. Olson and M. Cohen, "Constitutive Flow Relations for Austenitic Steels During Strain-Induced Martensitic Transformation", Proc. Intl. Conf. Mart. - ICOMAT 82, Leuven, Belgium, 1982
- (33) G.B. Olson, "Mechanically-Induced Phase Transformations in Alloys", Encyc. Mat. Sci. and Eng., Pergamon Press, 1982
- (34) G.B. Olson and M. Cohen, "Kinetics of Strain-Induced Martensitic Nucleation", Met. Trans. 6A, 1975, p.791
- (35) J.A. Venables, "The Martensite Transformation in Stainless Steel", Phil. Mag. 7, 1962, p.35
- (36) R. Lagneborg, "The Martensite Transformation in 18%Cr-8%Ni Steels", Acta Met. 12, 1964, p.823
- (37) P.L. Manganon and G. Thomas, "The Martensite Phases in 304 Stainless Steel", Met. Trans. 1, 1970, p.1577
- (38) F. Lacroisey and A. Pineau, "Martensitic Transformations Induced by Plastic Deformation in the Fe-Ni-Cr-C System", Met. Trans. 3, 1972, p.387
- (39) S.R. Pati and M. Cohen, "Nucleation of the Isothermal Martensitic Transformation", Acta Met. 17, 1969, p.189
- (40) V. Raghavan and M. Cohen, "Measurement and Interpretation of Isothermal Martensitic Kinetics", Met. Trans. 2, 1971, p.2409

- (41) G.B.Olson and M.Cohen, "Stress-Assisted Isothermal Martensitic Transformation: Application to TRIP Steels", Met. Trans. 13A, 1982, p.1907
- (42) R.C.Garvie, R.H.Hannick and R.T.Pascoe, "Ceramic Steel?", Nature 258, 1975, p.703
- (43) D.L.Porter, A.G.Evans and A.H.Heuer, "Transformation Toughening in Partially Stabilized Zirconia (PSZ)", Acta Met. 27, 1979, p.1649
- (44) A.G.Evans, D.B.Marshall and N.H.Burlingame, "Transformation Toughening in Ceramics", Advances in Ceramics vol.3, American Ceramic Society ed., 1981
- (45) A.G.Evans and A.H.Heuer, "Transformation Toughening in Ceramics : Martensitic Transformations in Crack-Tip Stress Fields", J. Am. Cer. Soc. 63, 1980, p.241
- (46) A.G.Evans, N.Burlingame, M.Drony and W.M.Kniven, "Martensitic Transformations in Zirconia - Particle Size Effects and Toughening", Acta Met. 29, 1981, p.447
- (47) R.M.McMeeking and A.G.Evans, "The Mechanics of Transformation Toughening in Brittle Materials", J. Am. Cer. Soc. 65, 1982, p.242
- (48) B.Budiansky, J.W.Hutchinson and J.C.Lambropoulos, "Continuum Theory of Dilatant Transformation Toughening in Ceramics", Division of Applied Sciences, Harvard University, 1982
- (49) J.R.Rice, "A Path-Independent Integral and the Approximate Analysis of Strain Concentrations by Notches and Cracks", J. Appl. Mech. 35, 1968, p.379
- (50) J.R.Rice, "Mathematical Analysis in the Mechanics of Fracture", Fracture II, E. Liebowitz ed., Academic Press, 1969, p.192
- (51) J.W.Hutchinson, "Singular Behavior at the End of a Tensile Crack in Hardening Materials", J. Mech. Phys. Sol. 16, 1968, p.13
- (52) J.R.Rice and G.F.Rosengren, "Plane Strain Deformation Near a Crack-Tip in a Power-Law Hardening Material", J. Mech. Phys. Sol. 16, 1968, p.1
- (53) D.Broek, Elementary Engineering Fracture Mechanics, Martinus Nijhoff Publishers, Boston, 1982, p.237

- (54) J.D.Landes and J.A.Begley, "The J-Integral as a Fracture Criterion", ASTM STP-514, 1972, p.1
- (55) J.A.Begley and J.D.Landes, "The Effect of Specimen Geometry on J_{Ic} ", ASTM STP-514, 1972, p.24
- (56) J.R.Bucci, P.C.Paris, J.D.Landes and J.R.Rice, ASTM STP-514, 1972, p.40
- (57) J.R.Rice, P.C.Paris and J.G.Merkle, "Some Further Results of J-Integral Analysis and Estimates", ASTM STP-536, 1973, p.231
- (58) J.D.Landes and J.A.Begley, "Test Results from J-Integral Studies : An Attempt to Establish a J_{Ic} Testing Procedure", ASTM STP-560, 1974, p.170^{Ic}
- (59) G.A.Clarke, W.R.Andrews, P.C.Paris and D.W.Schmidt, "Single Specimen Tests for J_{Ic} Determination", ASTM STP-590, 1976, p.27
- (60) ASTM E813-81, Annual Book of ASTM Standards, Section 3, Volume 03.01, 1983, p.762
- (61) G.A.Clarke, "Single-Specimen Tests for J_{Ic} Determination Revisited", ASTM STP-743, 1980, p.553
- (62) H.A.Ernst, P.C.Paris and J.D.Landes, "Estimation on J-Integral and Tearing Modulus T from a Single Specimen Test Record", ASTM STP-743, 1980, p.476
- (63) D.M.Parks, Course Notes in MIT Course 3.41J:The Mechanics of Fracture
- (64) R.M.McMeeking, "Finite Deformation Analysis of Crack-Tip Opening in Elastic-Plastic Materials and Implication for Fracture", J. Mech. Phys. Sol. 25, 1977, p.357
- (65) R.M.McMeeking and D.M.Parks, "On Criteria for J Dominance of Crack-Tip Fields in Large Scale Yielding", ASTM STP-668, 1979, p.175
- (66) J.R.Rice and M.A.Johnson, "The Role of Large Crack-Tip Geometry Changes in Plane-Strain Fracture", Inelastic Behavior of Solids, M.F.Kanninen et. al., 1970, p.641
- (67) F.A.McClintock, "Plasticity Aspects of Fracture", Fracture III, E.Liebowitz ed., 1971, p.48
- (68) J.W.Hutchinson, Non-Linear Fracture Mechanics, Technical University of Denmark, 1979, p.81

- (69) P.C.Paris, H.Tada, A.Zahoor and H.Ernst, "Instability of the Tearing Mode of Elastic-Plastic Crack Growth", ASTM STP-668, 1979, p.5
- (70) J.W.Hutchinson and P.C.Paris, "The Theory of Stability Analysis of J-Controlled Crack Growth", ASTM STP-668, 1979, p.37
- (71) P.C.Paris, H.Tada, A.Zahoor and H.Ernst, "An Initial Experimental Investigation of the Tearing Instability Theory", ASTM STP-668, 1979, p.251
- (72) J.F.Knott, Fundamentals of Fracture Mechanics, Butterworth, London, 1973
- (73) K.E.Puttick, "Ductile Fracture in Metals", Phil. Mag. 4, 1959, p.964
- (74) C.Crussard, "A Comparison of Ductile and Fatigue Fractures", Fracture, B.L.Averbach ed., 1959, p.524
- (75) H.C.Rogers, "The Tensile Fracture of Ductile Metals", Trans. AIME 218, 1960, p.498
- (76) J.Gurland and J.Plateau, "The Mechanism of Ductile Rupture of Metals Containing Inclusions", Trans. ASM 56, 1963, p.442
- (77) J.I.Blum and R.J.Morrissey, "Fracture in a Tensile Specimen", Proc. of 1st. Int. Conf. on Fracture vol. 3, 1965, p.1739
- (78) D.Broek, Elementary Engineering Fracture Mechanics, Martinus Nijhoff Publishers, 1982, p.38
- (79) J.Gurland, "Observations on the Fracture of Cementite Particles in a Spheroidized 1.05%C Steel Deformed at Room Temperature", Acta Met. 20, 1972, p.735
- (80) D.Broek, "The Role of Inclusions in Ductile Fracture and Fracture Toughness", Eng. Fract. Mech. 5, 1973, p.55
- (81) A.R.Rosenfield, "Criteria for Ductile Failure of Two-Phase Alloys", Metall. Rev. 13, 1968, p.29
- (82) A.S.Argon, J.Im and R.Safoglu, "Cavity Formation from Inclusions in Ductile Fracture", Met. Trans. 6A, 1975, p.825
- (83) A.S.Argon and J.Im, "Separation of Second Phase Particles in Spheroidized 1045 Steel, Cu-0.6Pct.Cr Alloy and Maraging Steel in Plastic Straining", Met. Trans. 6A, 1975, p.839

- (84) S.H.Goods and L.M.Brown, "The Nucleation of Cavities by Plastic Deformation", Acta Met. 27, 1979, p.1
- (85) M.F.Ashby, "Work-Hardening of Dispersion-Hardened Crystals", Phil. Mag. 14, 1966, p.1157
- (86) F.A.McClintock, "On the Mechanics of Fracture from Inclusions", Ductility, ASM, 1968, p.255
- (87) L.M.Brown and W.M.Stobbs, "The Work-Hardening of Copper-Silica II - The Role of Plastic Relaxation", Phil. Mag. 23, 1971, p.1201
- (88) F.M.Beremin, "Cavity Formation from Inclusions in Ductile Fracture of A508 Steel", Met. Trans. 12A, 1981, p.363
- (89) F.A.McClintock, "A Criterion for Ductile Fracture by the Growth of Holes", J. Appl. Mech. 35, 1968, p.363
- (90) J.R.Rice and D.M.Tracey, "On the Ductile Enlargement of Voids in Triaxial Stress Fields", J. Mech. Phys. Sol. 17, 1969, p.201
- (91) F.A.McClintock and A.S.Argon, Mechanical Behavior of Materials, Addison-Wesley, 1966
- (92) L.M.Brown and J.D.Embury, "The Initiation and Growth of Voids at Second Phase Particles", Proc. 3rd. Int. Conf. on Strength of Metals and Alloys, Institute of Metals, London, 1973, p.164
- (93) A.L.Gurson, "Continuum Theory of Ductile Rupture by Void Nucleation and Growth", part 1 in J. Eng. Mat. and Tech., Trans. ASME 99, 1977, p2
- (94) ibid., part 2 in Advances in Research on the Strength and Fracture of Materials 2A, D.M.R.Taplin ed., Pergamon Press, 1977, p.357
- (95) G.R.Yode, "Fractographic Lines in Maraging Steel - A Link to Fracture Toughness", Met. Trans. 3, 1972, p.1851
- (96) C.D.Beachem and G.R.Yode, "Elastic-Plastic Fracture by Homogeneous Microvoid Coalescence Tearing Along Alternating Shear Planes", Met. Trans. 4, 1973, p.1145
- (97) J.A.Van Den Avyle, "Correlation of Fractography, Microstructure and Fracture Toughness Behavior of High Strength Alloys", Doctoral Thesis, Department of Materials Science and Engineering, MIT, 1975

- (98) Paul Fleyshman, "Fracture Toughness of Rapidly Solidified Martensitic Steels", Master Thesis, Department of Materials Science and Engineering, MIT, 1982
- (99) J.W.Carson, "A Study of Plane Strain Ductile Fracture", Doctoral Thesis, Department of Mechanical Engineering, MIT, 1970
- (100) F.A.McClintock, "Crack Growth in Fully Plastic Grooved Tensile Specimens", Physics of Strength and Plasticity, A.S.Argon ed., MIT.Press, 1969
- (101) C.A.Berg, "Plastic Dilatation and Void Interaction", Inelastic Behavior of Solids, M.F.Kanninen ed., McGraw-Hill, 1970
- (102) J.M.Kraft, "Correlation of Plane Strain Crack Toughness with Strain Hardening Characteristic of a Low, a Medium and a High Strength Steel", Applied Materials Research, 1964, p.88
- (103) T.B.Cox and J.R.Low Jr, "An Investigation of the Plastic Fracture of AISI 4340 and 18Nickel-200Grade Maraging Steels", Met. Trans. 5, 1974, p.1457
- (104) J.Hadamark, Leçons sur la Propagation des Ondes et les Equations de L'Hydrodynamique, Paris, 1903
- (105) R.Hill, "Acceleration Waves in Solids", J. Mech. Phys. Sol. 10, 1962, p.1
- (106) T.Y.Thomas, Plastic Flow and Fracture of Solids, Academic Press, 1961, p.184
- (107) J.Mandel, "Condition de Stabilité et Postulat de Drucker", Rheology and Soil Mechanics, J.Kravtchenko and P.M.Sureys ed., Springer-Verlag, 1966, p.58
- (108) J.R.Rice, "The Localization of Plastic Deformation", Proc. 14th. Int. Cong. on Theoretical and Applied Mechanics, W.T.Koiter ed., North-Holland Publ. Co., 1976, p.207
- (109) A.Needleman and J.R.Rice, "Limits to Ductility Set by Plastic Flow Localization", Mechanics of Metal Sheet Forming, D.P.Koistinen and N.M.Wang ed., Plenum Publ. Co., 1978, p.237
- (110) H.Yamamoto, "Conditions for Shear Localization in the Ductile Fracture of Void-Containing Materials", Int. J. Fract. 11, 1978, p.347

- (111) J.R.Rice and J.W.Rudnicki, "A Note on Some Features of the Theory of Localization of Deformation", Int. J. Sol. and Struct. 16, 1980, p.597
- (112) M.Saje, J.Pan and A.Needleman, "Void Nucleation Effects on Shear Localization in Porous Plastic Solids", Int. J. Fract. 19, 1982, p.163
- (113) J.Pan, M.Saje and A.Needleman, "Localization of Deformation in Rate Sensitive Porous Plastic Solids", Int. J. Fract 21, 1983, p.261
- (114) V.Tvergaard, "Influence of Voids on Shear-Band Instabilities under Plane Strain Conditions", Int. J. Fract. 17, 1981, p.389
- (115) V.Tvergaard, "Ductile Fracture by Cavity Nucleation Between Larger Voids", J. Mech. Phys. Sol. 30, 1982, p.265
- (116) V.Tvergaard and A.Needleman, "Analysis of the Cup-Cone Fracture in a Round Tensile Bar", Danish Center for Applied Mathematics and Mechanics, Report No 264, June 1983
- (117) R.M.Bozorth, Ferromagnetism, Van Nostrand, 1951, p.109
- (118) C.L.Magee and R.G.Davies, "On the Volume Expansion Accompanying the FCC to BCC Transformation in Ferrous Alloys", Acta Met. 20, 1971, p.1031
- (119) G.Speich, "Cellular Precipitation in an Austenitic Fe-30Ni-6Ti Alloy", Trans. Met. Soc. AIME 227, 1963, p.754
- (120) T.Maki, K.Kobayashi and I.Tamura, "Effect of Ausaging on the Morphology of Martensite in Fe-Ni-Ti-Co Alloys", Journal de Physique 43, Colloque C4, supplement au n^o 12, 1982, pC4-541
- (121) ASTM E8-82, Annual Book of ASTM Standards, section 3, volume 03.01, 1983, p.119
- (122) J.F.Breedis and W.D.Robertson, "Martensitic Transformation and Plastic Deformation in Iron Alloy Single Crystals", Acta Met. 11, 1963, p.547
- (123) S.Jin, J.W.Morris, Jr., Y.L.Chen, G.Thomas and R.I. Jaffee, "An Investigation of Transformation Strengthening in Precipitation-Hardened Fe-Ni Austenite", Met. Trans. 9A, 1978, p.1625

- (124) W.W.Wilkening, "Dilatational Deformation and Fracture in Barre Granite", Doctoral Thesis, Department of Materials Science and Engineering, MIT, 1976
- (125) M.M.Hall and P.G.Winchell, "Tetragonality of Fe-Ni-Ti Martensite", Acta Met. 25, 1977, p.735
- (126) P.G.Winchell, "Preaging Austenite and Post-Aging Martensite - A Review of Recent Results", ICOMAT-79, p.547
- (127) G.B.Olson, private communication

BIOGRAPHICAL NOTE

The author was born on April 24, 1955 in Rio de Janeiro, Brazil. He was raised in the same city, where he graduated as a Metallurgical Engineer from Instituto Militar de Engenharia (IME) in 1977. From the same school he received the degree of Master of Science in Materials Science in 1979. In that same year he married Vania Maria de Araujo, also from Rio de Janeiro. In February 1980 he started his doctoral program at MIT. On September 16, 1981 his daughter Priscila de Araujo Deal was born in Boston, Massachusetts.